EFFICIENT, STABLE, FLEXIBLE AND TRANSPARENT PEROVSKITE SOLAR CELLS

BY

IDRIS KAYODE POPOOLA

A Thesis Presented to the
DEANSHIP OF GRADUATE STUDIES

KING FAHD UNIVERSITY OF PETROLEUM & MINERALS

DHAHRAN, SAUDI ARABIA

In Partial Fulfillment of the
Requirements for the Degree of

MASTER OF SCIENCE

In

PHYSICS

MAY 2017

KING FAHD UNIVERSITY OF PETROLEUM & MINERALS

DHAHRAN- 31261, SAUDI ARABIA

DEANSHIP OF GRADUATE STUDIES

This thesis, written by **IDRIS KAYODE POPOOLA** under the direction of his thesis advisor and approved by his thesis committee, has been presented and accepted by the Dean of Graduate Studies, in partial fulfillment of the requirements for the degree of **MASTER OF SCIENCE IN PHYSICS.**

m. a. Gondal

Dr. Muhammad Ashraf Gondal
(Advisor)

Dr. Abdullah A. Al-Sunaidi
Department Chairman

Dr. Saleem Rao
(Member)

Dr. Salam A. Zummo
Dean of Graduate Studies

a Mekki

Dr. Abdelkrim Mekki
(Member)

13/7/2017

Date

To Allah Almighty

ACKNOWLEDGMENTS

I am grateful to Allah (SWT) who in His infinite mercy grants me the opportunity to complete my Master of Science (MS) programme at the Physics Department of King Fahd University of petroleum and Minerals (KFUPM). My Appreciation goes to my wife Ochuwa and family who all stood by me during the course of my studies. I pray Allah (SWT) forgive and grant Jannatul Firdaus to my late brother AbdulWasi'i who passed away while I'm in a faraway foreign land.

I thank my Advisor Distinguished Professor M. A. Gondal to his supports and roles towards the success of my thesis work. The contribution of my committee members: Dr AbdelKrim Mekki and Dr. Saleem Rao are well appreciated. My sincere gratitude also goes to the Chairman, Physics Department, KFUPM for all his supports for the successful completion of my MS studies.

I appreciate KFUPM for providing enabling environment for studies and research for me and the entire students populace. The Kingdom of Saudi Arabia is thanked for providing me with scholarship. I thank the Nigerian community in KFUPM for making KFUPM a home away from home for me.

TABLE OF CONTENTS

LIST OF TABLES

LIST OF FIGURES

LIST OF ABBREVIATIONS

MOS	Metal Oxide Semiconductor
PLAL	Pulsed Laser Ablation in Liquid
J_{SC}	Short circuit current density
V_{OC}	Open circuit voltage
N3	Bis(isothiocyanato)bis(2,2'-bipyridyl-4,4'-dicarboxylato)ruthenium(II)
N719	2-(4-carboxypyridin-2-yl)pyridine-4-carboxylate;ruthenium(2+);tetrabutyl azanium;dithiocyanate
ETM	Electron Transport Material
HTM	Hole Transport Material
FF	Fill Factor
CE	Counter Electrode

ABSTRACT

Full Name : [IDRIS KAYODE POPOOLA]
Thesis Title : [EFFICIENT, STABLE, FLEXIBLE AND TRANSPARENT PEROVSKITE SOLAR CELLS.]
Major Field : [PHYSICS]
Date of Degree : [MAY 2017]

Energy remains an important part of continuous existence of humans and other organisms, so is the preservation of the environment. Renewable energy sources are the most viable and sustainable sources that can best meet the demand of the globe and the need for the sustainability of the environment. Solar photovoltaics are currently being used to harvest the enormous energy potential of the sun using silicon-based photovoltaic. Recently, third generation solution-processable solar cells have shown great potentials due to their unique properties like ease of fabrication, low cost, availability of materials and other remarkable features. Platinum counter electrodes were fabricated by a novel UV photoreduction fabrication process. Irradiation time, spin coating cycles and solvent effects were investigated for the photo-fabricated platinum counter electrodes. X-ray photon spectroscopy (XPS) was used to characterized the photo-fabricated sample. The catalytic performance of the electrodes were examined by cyclic voltammetry technique. The electrodes were used in the fabrication of titanium (IV) oxide (TiO_2) dye sensitized solar cells (DSSCs) achieving a maximum efficiency of 8.12%. P-type DSSC based on copper oxide (CuO) synthesized by pulsed laser ablation in liquid (PLAL) was fabricated and solvents effect on ruthenium based N719 dye sensitizer was investigated. Mixed cation and mixed halides lead-free bismuth perovskite solar cells were fabricated and characterized. Considerable high open circuit voltage (V_{OC}) of 0.4907 V was achieved.

ملخص الرسالة

الاسم الكامل:

عنوان الرسالة:

التخصص:

تاريخ الدرجة العلمية:

CHAPTER 1

INTRODUCTION

Energy remains an important part of development and economic sustenance of the world. It has also become a key in the world economy, security and even politics [1]. The energy demands of the world is in no way diminishing rather there have been quest for more energy supply to cater for the growing needs of the world populace as the earth continues to witness enormous increase in the world population. Report produced by the Energy Information Administration forecasts that the energy consumption from 2007 to 2035 in OECD countries will grow by 14 percent, and energy consumption in non-OECD countries will increase enormous by 84 percent within the same period [2].

The main sources of world energy are basically classified into two: renewable and non-renewable sources. Non-renewable sources are the most widely used sources of energy with fossil fuel, coal and nuclear sources being at the centre of the energy consumption of today. Fossil fuel and coal are not clean energy sources as these produce colossal amount of carbon oxides to the environment thus contributing to the rise in global warming and climate change[1]. Due to constant and rapid depletion of fossil fuel and coal they are not sustainable in driving global economic development and preserving the environment [1]. Recently, the Fukushima Daiishi nuclear disaster of March, 2011 has been an eye opener to the world towards harnessing renewable energy sources.

Renewable energy is the energy of the future and most of the nations are in favour of renewable energy. For example the EU renewable energy policy is being championed through a comprehensive legislative framework after passing through two earlier phases in reaching the EU's 2020 targets [3]. Sources of renewable energy are abundantly available in nature and are non-depleting. Renewable energy offers possibility of carbon-free economy for a more sustainable world. Major sources of renewable energy are the Solar, Wind, Tidal, and Biomass among others. The energy supply of the sun is reliable, sustainable and of long-term with no worry of depletion [2].

Solar energy harvesting has been done considerably through photovoltaic devices. By 2030 photovoltaics are predicted to account for one-third of global electricity generation [3]. Silicon has been the prime and most favoured material in the evolution of solar energy conversion for the generation of electricity. Power conversion efficiency (PCE) of 30% has been reported for uni-junction crystalline materials like silicon, gallium arsenide and other compound semiconductors [2]. High cost of manufacturing mono-crystalline silicon based photovoltaic is a major setback in the photovoltaic industry despite its high PCE [2]–[4]. Hence, there is need for the development of low production cost solar cell technologies.

Since the pioneering work of Professor Micheal Gratzel and Brian O'Regan on mesoscopic (nanoporous) dye-sensitized solar cells (DSSCs), photovoltaic solar cell based on DSSCs became an attractive alternative since photoelectric conversion efficiency (PCE) of more than 12% has been achieved by use of liquid electrolyte [4],[7].

Mesoporous titania TiO_2, N3 dye and iodide-based electrolyte are the major components of the DSSC. Other semiconductor metal-oxides and nano-composites hav been investigated for possible substitution of TiO_2. N719 dye has become a favourite sensitizer, quantum dots have also been used as sensitizers in DSC due to their outstanding optical properties and solid state electrolytes have recorded PCE of over 8.5% [4], [7], [8]. Due to high TiO_2 sintering temperature of about 500^{o}C, DSSCs is faced with the setback of having limited choice of substrate and device architecture based on colossal multi-junction devices [6].

Perovskite material was first used in solar cell fabrication by Miyasaka *et al* when they reported efficiency of 2.2% [3] using organometallic halides as light harvester in dye sensitized solar cells (DSSC). Perovskite solar cell (PSC) has since become the new sensation in photovoltaic solar cell devices after they later reported an improved PCE of 3.8% by replacing bromine with iodine [2], [5], [6]. Methyl ammonium lead iodide ($CH_3NH_3PbI_3$) has been reported to be a better light harvester than N719 ruthenium sensitizer used in DSSC [5]. A stunning 22.1% PCE was said to have been achieved by PSC. Spiro-OMeTAD serves has hole-transport material (HTM) and has helped to improve the stability of the mesoporous perovskite solar cell [2], [5]–[7]. Device architectures utilized in PSCs are mesoscopic heterojunction and planar heterojunction solar cell in regular (N-I-P) or inverted (P-I-N) form [5], [6], [8], [9]. For an N-I-P device architecture, electron transport materials (ETM) with conduction band (CB) energy matching the work function (WF) of the substrate and the CB of the perovskite layer and HTM having valence band (VB) energy close to the VB of the perovskite films and WF of the contact electrode (cathode) are required and vice versa for the inverted P-I-N architecture. Perovskite has also been used as component of tandem solar cell architecture [10]–[25] with Albrecht group recording a PCE of 19.9% [10] and Warner group reported PCE of 21.2% for cell area of 0.17cm^2 and 19.2% for cell area of 1.22 cm^2 [11]. PSC has been found to have better stability compared to its liquid electrolyte counterpart [6], [26]. The organometallic halide of $CH_3NH_3PbI_3$ degrades rapidly in humid environment and when exposed to ultraviolet radiation [3], [5]. A lot of work has been done to improve the efficiency of PSC using different approaches ranging from device architectures, lead substitution, fabrication techniques, choice of substrates and materials variation. Stability and durability of PSC have also been reported in literatures [5], [26], so is the effect of hysteresis studied [27]. One major drawback for the deployment of PSC despite its promising PCE is that lead plays very important role in the photovoltaic cells based on perovskite with highest efficiency till date. Lead is known to be toxic [3], [5] and efforts are ongoing to replace the lead component of the organometallic halide. PSC generally comprise of substrates (rigid or flexible), electron transport material (ETM), perovskite layer, hole transport materials (HTM) and contact electrode [3], [5].

Due to its low-temperature solution processing attribute, PSC has been fabricated on flexible substrates with remarkable performance [28], [29]. Flexible PSCs (flex-PSCs) have enjoyed considerable research attentions and outputs. Thus, given room for the possibility of roll-to-roll (RSR), portable, bendable, lightweight, conformable and wearable photovoltaic devices [6], [30], [31].

1.1 Statement of Problem

The low manufacturing and high efficiency with potential for improvement of DSSCs and PSCs has attracted worldwide photovoltaic community both academics and industrial players to research PSC as the real energy of the future. Lots of challenges are yet to be solved regarding the efficiency and safety of the constituent materials of PSC. The quest for higher efficiency of photon to electricity conversion is very much required. The need to protect both human and the environment from the toxicity of lead through the replacement of lead with high performance nontoxic metals is also very much demanded. Techniques for achieving a more durable and stable PSC is continuously been researched as durability is a major consideration for real time operation. Solar cell transparency could also help install photovoltaic in unusual places like on smart electronic devices, wall of skyscrapers, automobiles, and aircrafts among other possibilities. This research is focused on fabrication and characterization of solution-processable dye sensitized and perovskite solar cells.

1.2 Research Objectives

The objectives of this thesis research are as follow:

i. To synthesize organometallic halides.

ii. To fabricate photovoltaic devices using perovskite and dye sensitized materials

iii. To study the efficiency of other metal oxides and organic hole transport materials (HTMs) for a possible better performance than bench-marked metal oxides like TiO_2

To investigate the better solar cell device architectures for the abovementioned objectives.

CHAPTER 2

LITERATURE REVIEW

2.1 Dye Sensitized Solar Cells

Third generation solar cells such as dye-sensitized solar cells (DSSCs), quantum-dots sensitized solar cells (QDSSCs) and recently perovskite solar cells (PSCs) have generated enormous research interests as they are expected to ultimately rival and possibly replaced silicon solar cells in the pursuit of renewable and clean energy utilizing the abundance energy of the sun. The research interests attracted by theses third generation solar cells are due to their solution processing capabilities, low costs, easy fabrication techniques, efficient devices performances and potentials for application in flexible devices[32]–[36]. Since the work of Gratzel in 1991[37], various components of DSSCs such as the substrates, photoanodes, sensitizers (dyes), electrolytes and the counter electrodes (CEs) have continued to be researched for new materials, synthesis methods and fabrication techniques. N-type photoanode with molecularly engineered dye has reached a record power conversion efficiency (PCE) of 13%[38]. TiO_2 remains the most commonly used n-type semiconducting photoanodes[38]–[43]. ZnO, photoactive doped metal oxides and various nanocomposite materials have been reported as photoanodes in DSSCs[44]–[46]’[47]. Ruthenium (Ru) based sensitizers such as N3, N719 among others have become the *de facto* dye materials for DSSCs[48]. Liquid electrolytes are usually comprised of iodide/triiodide (I^-/I^{3-}) and cobalt complexes (Co^{2+}/Co^{3+}) redox couples[49], [50]. Highly electrocatalytic materials like platinum (Pt) are used to reduced I^{3-} to I^- at the interface of the electrolyte/CE in order to sustain the flow of current and regenerate molecules of the oxidized sensitizer in the DSSCs devices[51], [52].

The CE is one of the foci interests of research towards the improvement and advancement of DSSCs. Various efforts have been on in utilizing other non-platinum electrocatalytic materials[32] as well as developing new techniques for the fabrication of Pt CE. Some of the alternative materials that been investigated and reported include polymeric conducting materials such as poly(3,4-ethylenedioxy-thiophene):poly(styrenesulfonate) (PEDOT: PSS)[32], [53]–[56], carbon materials such as carbon soot, graphene, carbon nanotube (CNT), carbon nanofiber (CNF) and graphite[57]–[60], inorganic semiconducting compounds such as NiS, CoS, and CoSe[61], platinic composite materials[62], [63] and other electrocatalytic composite materials[64], [65]. Polymeric conducting materials and carbon materials have the advantages of low costs, solution processing and low temperature fabrication requirement. Pt has consistently shown excellent electrocatalytic performance with great transparency and holds the record of the highest PCE for DSSCs[51]. Pt CEs are usually fabricated at an elevated temperature of 450 °C from platinic acid (H_2PtCl_6) precursor[66] or vacuum sputtered from Pt target[67], [68]. Thermal decomposition of H_2PtCl_6 for the fabrication of Pt CE is not suitable for material with lower thermal stability at the required elevated temperature for the synthesis of Pt. Hence, flexible Pt CE on conductive polyethylene naphtholate (PEN), polyethylene terephthalate (PET) and textile cannot be achieved through thermal decomposition process[51], [52], [69]. Sputtering deposition on the other hand results in wastage of material during deposition process, thereby, limiting its use for large scale production[51], [52], [69].

Researchers have reported several attempts at fabricating Pt CEs at low temperature. Electrodeposition technique is one of such methods employed in the fabrication of Pt CE at low temperature. This method which takes place at room temperature involves three electrodes configuration with transparent conductive oxide (TCO) substrate acting as the working electrode and electrolyte material containing platinic acid solution [70]–[72]. A cyclic voltammetry process is then performed using an electrochemical system. Electrophoretic deposition was used by Yin *et al*[73]. They prepared H_2PtCl_6 glycol solution and preheated it under stirring for 6 h in an atmosphere of argon. ITO-PEN substrates were immersed in the resulting Pt-colloid and driven by a D.C. field of 1.6 Vcm^{-1}. The Pt coated electrode was washed with deionized (DI) water and ethanol before being post thermally treated at 60 ^{o}C for 30 mins. Both electrodeposition and electrophoresis method have the shortcoming of large Pt loading making them unfeasible for commercial production.

Some other alternative methods have however been reported. Chemical wet-chemistry reduction has been utilized for the fabrication of Pt CEs form H_2PtCl_6 employing acidic reducing agents without subsequent treatment. Matoh *et al.*[74] employing chemical reduction method prepared H_2PtCl_6 in ethanol for the synthesis of nanostructured metallic Pt. The ethanolic Pt precursor was either spin coated or drop coated on fluorine doped tin oxide (FTO) glass electrodes or indium doped tin oxide (ITO) PET flexible substrates and dried at room temperature. The coated surfaces were then treated with gaseous formic acid reducing agent at temperature of 100 ^{o}C for a period of 15 minutes. Hseih *et al.*[52] used modified chemical reduction method to fabricate Pt CEs. Polyvinylpyrrolidone (PVP) served as surfactant, $NaHBr_4$ as reducing agent, NaOH was used to achieve neutral platinic precursor and UV-ozone treatment was used to decompose the surfactant after deposition on FTO or ITO-PEN. Polyol reduction technique is a facile method of synthesis of Pt from H_2PtCl_6 whereby ethylene glycol (EG) is used as reducing agent. Mei *et al.*[75] fabricated Pt CEs using EG solution of $H_2PtCl_6 \cdot 6H_2O$. the deposited precursor was thermally treated at 180 ºC. The synthesized Pt on the substrates exhibited dense and porous Pt structures. The earlier resulting from growth of Pt on the substrates following the reduction while the latter is due to Pt nanoparticle precipitation. Li *et al.*[51] used similar polyol method with modification of the pH of the H_2PtCl_6 and preheating the precursor solution at 110 ºC for 30 mins. They as well pretreated the substrates with 'piranha' and 3-mercaptopropyl(trimethoxysilane) (MPTMS) to produce a thiol-functionalized silane self- assembled monolayer (SAM) film on the conductive substrates. The as-prepared functionalized substrates were soaked in the platinic EG solution for 12 h and rinsed with ethanol to eliminate undesirable residues and dried in nitrogen environment with no post fabrication thermal treatment.

In this study, we photofabricated Pt CEs employing different solvents. Our photofabrication process utilized UV irradiation of deposited solutions of H_2PtCl_6 to achieve Pt CEs. This novel method of fabricating Pt CEs is an all-room temperature process without pre/post-thermal treatment and was carried out in ambient environment. This method utilized minimal Pt loading. It requires no surfactant addition, which is usually required to be removed either by heating or other methods. It is as well properly suited for plastic substrates as no acidic treatment is performed in the fabrication process. This photofabrication method is simple, ease and requires no pretreatment of substrates nor posttreatment procedures. It is equally a fast processing technique for Pt CEs fabrication.

2.2 Pulsed Laser Ablation in Liquid

For photoactivity applications, n-type photoanode and p-type photocathode materials are desired as nanomaterials. Nanosized materials such as nanoparticles (NPs), nanotubes (NTs), nanospheres (NSs) and nanowires (NWs) exhibit novel material properties that are significantly different from those of individual atoms and molecules or bulk materials. Due to high surface-to-volume ratio of nanomaterials, properties such as reactivity, catalytic strength, electrical and optical properties are greatly enhanced. Nanomaterials occur as one dimension (thin films), two dimensions (nanowires, nanotubes and nanorods) and three dimensions (nanoparticles, nanospheres). Synthesis procedure and techniques have been reported to impact on morphology, crystallinity and optical characteristics of nanomaterials. Hence, p-type semiconducting metal oxides synthesis methods could affect their performance in DSSCs. Some of the method generally used to synthesize nanosized semiconducting metal oxides include hydrothermal, solvothermal, sol-gel, pulsed laser deposition and pulsed laser ablation.

Pulsed laser ablation (PLA) is a process in which a pulsed laser beam is applied to remove/eject material from a solid surface. Pulsed laser ablation in liquid (PLAL) has recorded tremendous usage in the synthesis of nanomaterials over the past decade. Remarkably, a large variety of nanomaterials such as metals, metallic alloys, metal oxides, semiconductors, and carbon-related materials have been excited, fragmented, conjugated and synthesized by PLAL. The unique features of this technique are the simplicity of the procedure, the versatility with respect to materials and solvents, and the absence of chemical reagents or ions in the final product. PLA does not require costly chambers and high vacuum pumping systems hence is considered as a clean method. Varying different parameters such as: laser wavelength, the pH of the solution, adding surfactants and the temperature of solution, the size of synthesized materials can be controlled, which could lead to change of the physical and chemical properties of the synthesized materials. PLAL has the following advantages: (i) laser-generated (metal) nanoparticles are charged and thus have an extremely high colloidal stability, (ii) contrary to dry nanopowders, nanoparticle colloids are not inhalable and thus lead to an improved occupational safety during product handling, (iii) chemical precursors are not required and thus the colloids are 100% pure, and (iv) this method can be applied universally with an almost unlimited variety of materials and solvents.

2.3 Perovskite Solar Cells

Perovskites are generally denoted by ABX_3 (Figure 2.1) where A is organic cation (cesium, methylammonium, ethylammonium, formamidinium and phenylammonium), B is metal inorganic-cation (Ge, Pb, Sn, Sr and Bi) and smaller than A while X is any of the halide elements (I, Cl and Br) [3], [5], [7], [76]–[86]. Hence, there are various choices of material selections for the perovskite material formation and various substitutional doping matrixes have been reported in literature. Different electron transport materials (ETMs) and hole transports materials (HTMs) have been employed in the fabrication of flexible Perovskite solar cells. Likewise, ETM and HTM-free flex-PSCs are also found in literature. Several contact electrodes have also been attempted in the fabrication of efficient flex-PSCs. Here, we report some of the materials that have been used in the fabrication of flex-PSCs.

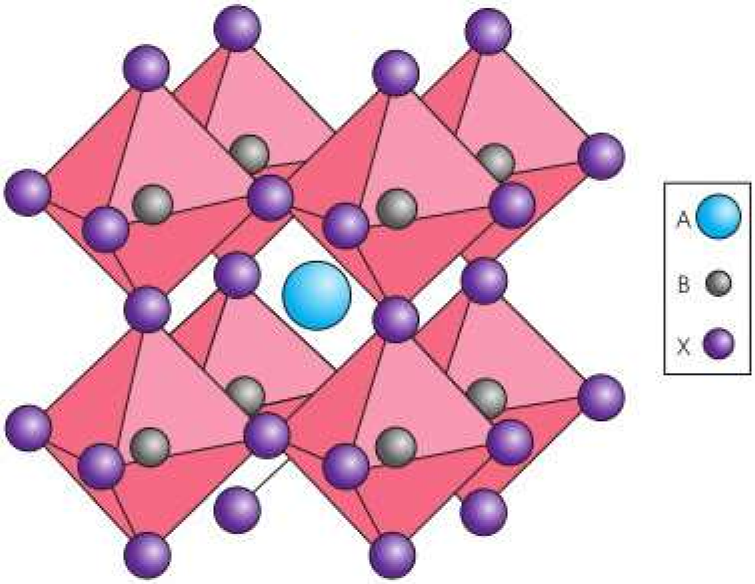

Figure 2.1: Typical crystal structure of organic-inorganic perovskite material [76]

2.3.1 Flex-PSCs perovskite films: deposition technique, morphology and crystallinity

PSCs with the very high efficiencies records are lead-based organometallic halides. This is largely true for both rigid substrates and flexible substrates PSCs. PSCs have been fabricated using one-step spin-coating technique [8], [9], [28], [29], [87]–[90], vapour-assisted solution process (VASP) [91], [92], two-step deposition technique (TSD) [9], [89], [91] and chemical vapour deposition (CVD) technique [9], [89], [91]. Perovskite crystals synthesis and morphological study for flex-PSCs have been reported by various research groups. The morphology of the ABX_3 films is vital for high performance PSC [29], [93], [94]. Two-step deposition technique has been favoured to improve the morphology of the perovskite (ABX_3) layer with a superior crystallization [93]–[96]. The two-step deposition techniques that have been majorly utilized in the fabrication of flex-PSC are spin-spin and spin-dip coating methods. Spin-spin deposition technique involves the spin coating of BX_2 followed by spin coating solution of AX on the BX_2 [94]–[96]. While spin-dip deposition method is done by immersing a spin-coated layer of BX_2 in a solution of AX in a solid-liquid reaction mode to achieve the ABX_3 perovskite layer [6], [96]. Solvent choices have also been reported to affect the perovskite films formation, hence proper solvents have to be employed in the ABX_3 crystals formation with optimal performance [94], [95], [97].

Liu and Kelly [6] synthesized $CH_3NH_3PbI_3$ using two-step spin-dip solution processing technique by first spin-coating PbI_2 followed by a subsequent dip in CH_3NH_3I solution at room temperature. The X-ray diffraction (XRD) analysis of the synthesized $CH_3NH_3PbI_3$ revealed a tetragonal crystal with a crystallite size of 75nm. They posited that the recorded large crystallite size may enhancement mobility of the carriers generated within the $CH_3NH_3PbI_3$ layer, reduce defect and trap states recombination and an increment in the device effective optical path length. The flex-PSC fabricated with this perovskite layer attained a high PCE of 10.3% with a photovoltage (V_{oc}) of 1.03 V, photocurrent density (J_{sc}) of 13.4 mA-cm^{-2} and fill factor (FF) of 73.9% while its glass-ITO counterpart achieved PCE of up to 15.7%. The quality of the $CH_3NH_3PbI_3$ crystals formed using spin-dip preparation technique is dependent on the duration of immersion [93]. Table 1 illustrates device parameters dependency on immersion time. At dipping time of 40 s, the optimum device parameters (photovoltaic and kinetic) were obtained due to the complete conversion of PbI_2 to $CH_3NH_3PbI_3$ with large area coverage. Further dipping time of 50 s led to washing away of the $CH_3NH_3PbI_3$ film consequently leading to reduced device performance [93]. Wang *et al* [98] reported similar deposition technique for the formation of $CH_3NH_3PbI_3$ film layer in their work.

Mixed halide perovskite layer has also been used in the fabrication of flex-PSC with excellent performance. You *et al* [29] in their work employed a mixed iodide-chloride perovskite $CH_3NH_3PbI_{3-x}Cl_x$ layer owing to the extensive lifetime of its carrier and decent electrical properties [99]. They produced perovskite layer by combining 0.8 M of $PbCl_2$ and 2.4 M of CH_3NH_3I corresponding to a ratio of 1:3 via one-step deposition technique. The $CH_3NH_3PbI_{3-x}Cl_x$ film was found to be uniform with some pinholes observed and having a thickness of 340 nm. The thicker perovskite film guarantees adequate light absorption [5]. The XRD characterization of the $CH_3NH_3PbI_{3-x}Cl_x$ revealed the crystal to be along the direction (110) similar to the $CH_3NH_3PbI_3$ crystals reported by Burschka [100]. The quantification of Cl in the $CH_3NH_3PbI_{3-x}Cl_x$ was done with the aid of X-ray photoelectron spectroscopy (XPS) and Cl was found to be very minute in the $CH_3NH_3PbI_{3-x}Cl_x$ composition. They found out that the percentage composition of Cl in (Cl+I) was 2.2% and further measurement of Cl of several samples taken from the same synthesized $CH_3NH_3PbI_{3-x}Cl_x$ was very minimal. The $CH_3NH_3PbI_{3-x}Cl_x$ having an energy band gap of 1.5eV [29], [90] recorded V_{oc} of 0.86V, J_{sc} of 16.5 mA-cm^{-2}, *FF* of 64% and a PCE of 9.2%. Dianetti *et al* [101] used similar one-step deposition technique of CH_3NH_3I and $PbCl_2$ at 3:1 molar ratio to synthesize $CH_3NH_3PbI_{3-x}Cl_x$ on a transparent conductive oxide (TCO)-free flexible substrate obtaining a PCE of 4.9%. At a molar ratio of 1:1 of CH_3NH_3I and PbI_2, Weerasinghe *et al* [102] deposited $CH_3NH_3PbI_3$ for their flex-PSC devices. Yin *et al*[103] also employed one-step spin-coating of $CH_3NH_3PbI_3$ on a PEN-ITO substrates achieving PCE of 13.43%.

Using fast-deposition-crystallization method [104] Zhang *et al* [105] synthesized $CH_3NH_3PbI_3$. The $CH_3NH_3PbI_3$ layer was prepared with PbI_2 and CH_3NH_3I precursors at molar ratio 1:1 in an anhydrous N,N-dimethylformamide (DMF) having a 40 wt% final concentration for a 340 nm optimal thickness. The solution underwent an overnight stirring in nitrogen glove box at a temperature of 60ºC and was subsequently filtered using 0.45 μm polyvinylide fluoride filter prior to usage. The morphology of the prepared $CH_3NH_3PbI_3$ was analyzed with the aid of scanning electron microscope (SEM) with no pin-hole revealed on the surface of the crystals. The perovskite film quality was high with plate-like shape of diameters ranging from 200 nm to 700 nm.

Dual akylammoniunhalides of formamidinium iodide ($CH(NH_2)_2I$) and CH_3NH_3Cl solutions at the ratio of 50:5 was spin-coated on an annealed PbI_2 solution for 30 s at 3000 rpm by Xu's group [106] to form a chlorine-infused formamidinium lead triodide (Cl-$FAPbI_3$) layer of 350 nm thickness with a record PCE of 12.7% on PET-ITO flexible substrate. Xi *et al* [107] prepared flex-PSCs with modified α-$FAPbI_3$ (α-$HC(NH_3)_2PbI_3$) by evaporating 40 nm thick PbI_3 on (PEN-ITO)/PEDOT:PSS substrate under 10^{-5} mbar pressure at 1.0 A^0 s^{-1} rate and heated at 60 ºC for 60 s in a N_2 glove box. Then followed by the spin-coating of 0.063 mol L^{-1} of FAI, MABr or their mixture at (4:1, 3:1, 2:1, 1:1 and 0:1) in 2-propanol solution at a speed of 2000 rpm for 20 s. Moisture content of the prepared films was removed by heating at 90 ºC (cold), 120 ºC (mild) and 150 ºC (hot) for 10 min, respectively. The excess unreacted precursors (FAI or MABr), 2-propanol solvent) was spun on the perovskite layer for 60 s at 2000 rpm then finally annealed at

120 ^{o}C for 5 min. The phase of the crystal layers changed from trigonal to pseudocubic then to cubic with respect to applied heat (cold-to-mild-to-hot) with grain sizes increasing accordingly. A champion device efficiency of 13.03% was achieved with mild thermal treatment and moderate doping.

Tavakoli *et al* [108] utilized two-step sequential thermal evaporation deposition technique to deposit the $CH_3NH_3PbI_3$ layer on a flexible willow-glass substrate. This technique involves preloading quartz crucibles with PbI_2 and CH_3NH_3I followed by evaporating them in sequence onto a metal oxide coated substrate. The authors carried out the deposition on a (willow glass)-ITO/ZnO substrates at a deposition rate of 0.1- 0.2 nm s^{-1} under high vacuum pressure of 4×10^{-6} mbar. Calibrated quartz sensor was used to regulate the rate at which the vapours are deposited in order to achieve desired thickness. Their optimal device combined a 1:1 ratio of PbI_2 and CH_3NH_3I forming a $CH_3NH_3PbI_3$ film with 340 nm thickness.

Gas-assisted processing method first reported by Huang *et al*[109] was employed by Dkhissi *et al* [110] in synthesizing $CH_3NH_3PbI_3$ layer on an PET-IZO flexible substrate. This technique leads to fast-solvent evaporation via blowing of inert gas at certain pressure during spin coating with even $CH_3NH_3PbI_3$ film achieved [109]. They spin-coated 40 wt% precursors solution of CH_3NH_3I and PbI_2 at a molar ratio of 1:1 in DMF solvent for 30 s at 6500 rpm while argon gas was being directed at it 3 s after the start of spinning. This was then followed by annealing for 10 min to get the $CH_3NH_3PbI_3$ layer. XRD revealed a tetragonal phase $CH_3NH_3PbI_3$ crystals.

Slot-die coating, known to be successful in mass production of flexible organic photovoltaics (flex-OPV) and flexible polymer solar cells (flex-PoSCs) [111], [112] was deployed by Schmidt *et al* [113] to fabricate flex-PSCs on a PET-ITO substrate with sheet resistance of 45 Ω sq^{-1} in both one and two-step deposition techniques. The one-step process involved slot-die coating of 350 mg mL^{-1} mixtureof $PbCl_2$ and CH_3NH_3I (1:3 in a DMF solvent) at a pump rate and web speed of 0.017 mL min^{-1} and 0.5 m min^{-1}, respectively. Meanwhile, 400 mg mL^{-1} PbI_2 DMF solution was first slot-die coated 0.02mL min^{-1} pump rate and 1 m min^{-1} web speed in the two-step method. This was followed by slot-die coating of CH_3NH_3I layer at a pump rate and web speed of 0.03 mL min^{-1} and 1 m min^{-1}, respectively. The grown $CH_3NH_3PbI_3$ was annealed at a temperature of 110 ºC for 5 min. All other layers of the flex-PSC were slot-die coated except the top contact electrodes. Best devices PCEs of 4.9% (one-step) and 2.6% (two-step) were achieved.

2.3.2 Substrate Choice

PSC has been fabricated largely on rigid glass substrates and rigid substrates hold the record for the highest PCE [4-7, 10-11, 13-14, 16-18, and 20-22]. PSCs fabricated on rigid substrate are carried out at a very high temperature. However, low-temperature solution processed PSCs have been reported with encouraging and high PCE. Dianyi et al [9] using Indium-doped transparent oxide (ITO)/poly(ethylene terephthalate) (PET) as substrate prepared PSC via room-temperature solution processed technique and recorded a PCE of 10%. Cristina et al [12] used a flexible AZO/Ag/AZO/PET substrate to achieve a flexible PSC with an efficiency of 7% and a repeated bending showed no deterioration of device performance. Meanwhile, Jingbi and co-workers [15] obtained a 9.2% PCE using ITO/PET flexible substrate at a low-temperature processing. The encouraging high PCE recorded by flexible substrates makes roll-to-roll (R2R) PSC the future.

2.3.3 PSCs Electron Transport Materials (ETMs)

Perovskite (ABX_3) crystals are not only good light harvesters with long range diffusion length and high charge-carrier mobility [114]' but can also act as both electron transport material (ETM) and hole transport material (HTM) [5,48]. Incorporation of ETMs has been used to enhance collection of carrier, thereby achieving better photovoltaic performance. ETMs materials used in flex-PSCs are generally classified into metal-oxide and organic ETMs. The metal-oxides must be deposited at a relatively low temperature and annealing temperature of not more than 150ºC as against rigid-PSCs that can withstand temperature of up to 500ºC for TiO_2, ZrO_2 or Al_2O_3 ETMs [3,45]. Organic ETMs have also enjoyed adequate deployment and are well suited for flex-PSCs. They are solution-processed at low temperature and are equally flexible. We examine below some of the ETMs that have gained applications in flex-PSCs.

2.3.3.1 Metal-oxide ETMs

A. TiO_2-ETM Flex-PSCs

Titanium dioxide (TiO_2) has seen tremendous usage in all organic-based solar cells such as dye sensitized solar cells (DSSCs), organic solar cells (OSCs) and perovskite solar cells (PSCs) [115]–[119]. Low temperature solution-processed TiO_2 ETMs have been well reported in literatures for flex-PSCs. The conduction band (CB) energy of TiO_2 is suitably aligned with the perovskite CB (illustrated in Figure 2.2), thus, easing the flow of electrons from the perovskite layer to the TiO_2-ETM. Dkhissi *et al* [110] fabricated a planar flex-PSC using low temperature solution-processed mesoporous TiO_2 (meso-TiO_2) with maximum PCE of 12.3%. They spin-coated dispersed meso-TiO_2 of 28 mg mL^{-1} in ethanol on polyethylene terephthalate coated with indium-doped zinc oxide (PET-IZO) flexible substrate and annealed at temperature of 150°C for a duration of 1 h. The surface of the PET-IZO substrate was well covered with TiO_2 100 nm thickness which helps to prevent contact between the substrate and the $CH_3NH_3PbI_3$ layer. It is desired that the TiO_2 layer does not become thicker so as not to inhibit the transportation of charge carrier through the film as it becomes resistive. Weerasinghe *et al* [102] fabricated flex-PSC using similar PET-IZO/meso-TiO_2 materials with device performance of average J_{sc} of 16.8 mA cm^{-2}, *Voc* of 1020 mV, *FF* of 69% and PCE of 12%. TiO_2 in combination with Al_2O_3 nanoparticles (NPs) scaffold ETM was reported by the group of Troughton [120] in which their device was fabricated on Titanium (Ti)-foil flexible substrate attaining PCE of 10.3%. Al_2O_3 scaffold is particularly helpful in blocking holes carrier from getting to the TiO_2 layer preventing recombination of carriers thereby enhancing charge extraction. Meso-TiO_2 was incorporated into flexible fiber-based PSC by Qiu and co-workers [121] with a PCE of 3.3% recorded, further highlighting the versatility of TiO_2 ETM for flex-PSCs.

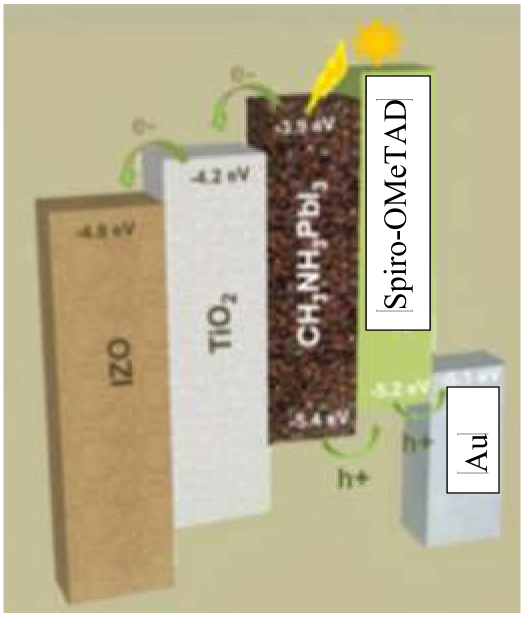

Figure 2.2: Energy levels of different layers of perovskite solar cells showing charge transfer mechanism of TiO$_2$ ETM [110]

Amorphous TiO$_2$ (amp-TiO$_2$) was employed by Yang *et al* [122] as ETM owing to its good transparency to solar spectrum, improved electron injection and reduction in cathodic transfer resistance. Its Fermi level is well aligned with the least unoccupied molecular orbital (LUMO) of the perovskite layer. Kelvin Probe Force Microscopy (KPFM) was used to determine the Fermi level of the amp-TiO$_2$ as -4.15eV. The PET-ITO/amp-TiO$_2$ recorded J_{sc} of 20.9mA cm^{-2}, V_{oc} of 1.03V, FF of 70% and PCE of 15.07%.

In their work, Wang *et al* [98] synthesized TiO$_2$ nanotube (TiO$_2$-NT) ETM via electrochemical anodization [123], [124] at voltage and temperature of 20 V and ~20ºC respectively, for period of 10 min. Ti-foil served as the working electrode while the counter electrode used was platinum gauge in the two-electrode anodization configuration employed for the synthesis. 0.3 wt% ammonium fluoride containing ethylene glycol and 2 vol% dionized (DI) water electrolyte solution was used. The as-synthesized TiO_2-NT was thermally annealed at 450ºC for 180 min so as to convert amp-TiO_2 to the anatase (ana-TiO_2) phase. The TiO_2-NT was further treated in aqueous solution of 40 mM $TiCl_4$ at 70ºC for 10 h, thereafter washed with ethanol and DI water for enhanced cell performance. The TiO_2-NT based flex-PSC fabricated on Ti-foil achieved PCE of 8.31%. In an improved fiber-shaped flex-PSC, Qui *et al* [125] utilized TiO_2-NT as ETM to achieve J_{sc} of 8.9 mA, V_{oc} of 0.852 V, *FF* of 48.2% and a PCE of 3.6%.

Plasma assisted/enhanced atomic layer deposition (Pl-ALD) of TiO_2-ETMs of flex-PSCs have been investigated owing to its quality film formation, low temperature processing capability and lower pinhole density [36]. Kim *et al* [126] employed annealing-free Pl-ALD-TiO_2-ETM thickness of 20 nm to fabricate flex-PSC on PEN-ITO flexible substrate with PCE of 12.2% with a photocurrent density J_{sc} of above 20 mA cm^{-2} resulting from efficient recombination blocking and electrons mobility. Similarly, Giacomo's group [36] used Pl-ALD-TiO_2 in combination with UV treated TiO_2 scaffold layer on PET-ITO flexible substrate. Their champion flex-PSC has a PCE of 7.4%. *J-V* curves shown in Figure 2.3 illustrate the performance of device based on Pl-ALD-TiO_2 with UV-TiO_2-scaffold and without.

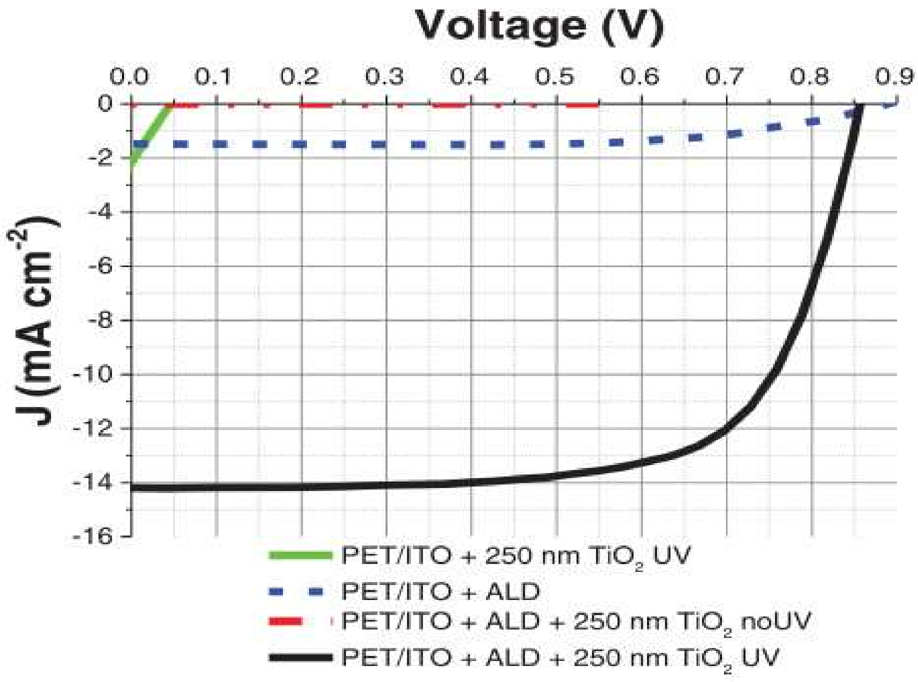

Figure 2.3: I V characteristics of an atomic layer deposited TiO_2 with and without UV treatment [36]

B. ZnO-ETM PSC

ZnO became the first candidate to be employed in the fabrication of flex-PSCs owing to its high electron mobility, low temperature solution processing and non-requirement of calcination or sintering process [127], [128]. Kumar *et al* [129] took the advantage of these unique properties of the ZnO to report the first fabricated flex-PSCs that utilized ZnO compact layer prepared using electrodeposition method and ZnO nanorod synthesized via chemical bath deposition (CBD) as ETM on PET-ITO flexible substrate with a modest PCE of 2.62%. Liu and Kelly [6] used ZnO NPs ETM to fabricate their flex-PSC on PET-ITO. The ZnO NPs used was synthesized by dissolving zinc acetate in methanol. Device parameters obtained for their best performing flex-PSC are J_{sc} of 13.4 mA cm^{-2}, V_{oc} of 1.03 V, *FF* of 73.9% and PCE of 10.2%. Jung *et al* [130] reported similar preparation method for ZnO NPs ETM deposited on PEN-ITO flexible substrate. It is important to control the thickness of ETMs for an optimal device performance. Too thin ETMs layer could aid recombination of carriers as the perovskite layer could be in contact with the ITO substrate thereby lowering device performance. While too thick ETMs layer would hinder electron injection across the perovskite layer. Jung's group [130] investigated the effect of ZnO-ETMs thickness on the device performance of flex-PSCs fabricated on 0.12 cm^2 active area of PEN-ITO substrate.

C. Zn_2SnO_4-ETM PSCs

Ternary Zn_2SnO_4 (ZSO) NPs transparent conducting oxide (TCO) has been reported as a photoanode material in DSSCs [30], [131]–[134]. It is a wide band gap (3.8 eV) n-type semiconductor with interesting electrical and optical properties [133]. Shin *et al*[30] fabricated flex-PSC based on low temperature solution processed ZSO NPs on PEN-ITO flexible substrate. The ZSO manifested a superb transmittance in the visible light region. The ZSO NPs were synthesized through Zn-hydrazine complex precursor at reaction temperature of 90°C for 2 h with controlled ration of hydrazine/Zinc (N_2H_4/Zn).

The transmittance analysis [30] revealed that ZSO NPs synthesized has high transparency. The ZSO-ETM flex-PSCs fabricated displayed a widened external quantum efficiency (EQE) plateau over 80% between 460 and 755 nm wavelength with J_{sc} of 21.2 mA cm^{-2}, excellent electron collection and light harvesting within the flex-PSCs (Fig. 10c). The photovoltaic performance of the ZSO-based flex-PSCs are J_{sc} = 21.6 mA cm^{-2}, V_{oc} = 1.05 V, FF = 67% and PCE = 15.3%.

Shin's group, in another report [135] noted the loss of photogenerated electrons in the ETM (vis-à-vis ITO-ETM and ETM-perovskite) interfaces as one of the causes for the poorer performance of the flex-PSCs as compared to their rigid-PSCs counterpart. They further reported the minimization of the photogenerated electrons loss by tailoring the energy level and transporting ability of metal oxide ETM through the usage of ZSO NPs and quantum dots (QDs). Due to large crystallite size and higher work function (WF), ZSO NPs are advantageous for the transport of electron within the ZSO ETM and electron transfer at the ZSO/ITO interface. ZSO QDs on the other hand have lower WF that is valuable for a large built-in potential (V_{bi}) at the ZSO-perovskite interface as illustrated in Figure 2.4.

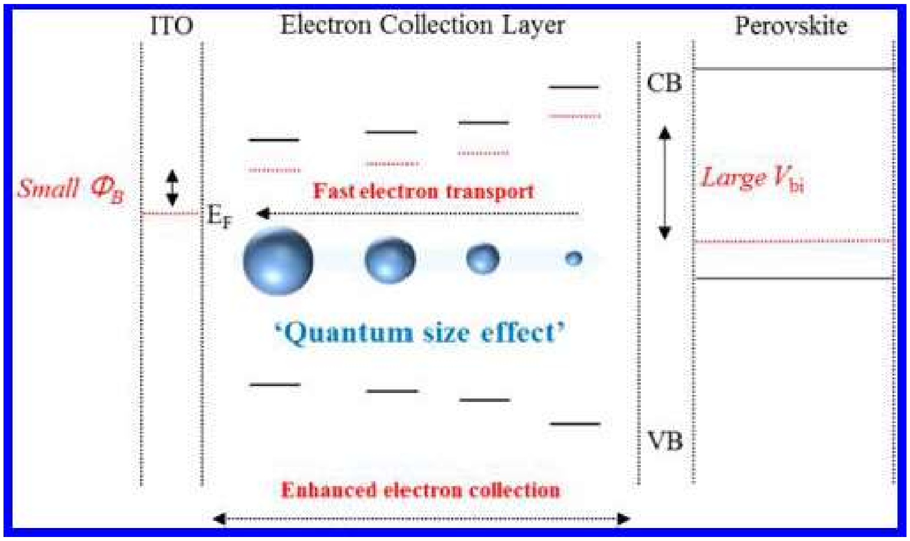

Figure 2.4: Schematics of QD Zn_2SnO_4 showing electron transport within the particle and energy levels of at the ZSO/ITO and ZSO/Perovskite interfaces [30]

They found the combination of both ZSO NPs and QDs (in other to benefit from their respective features) improved the devices performance of the flex-PSCs.

2.3.3.2 Organic-ETMs PSCS

Organic materials have found applications in perovskite solar cells (PSCs) particularly as HTMs asides the organic components of the perovskite crystals. In the quest to reduce hysteresis effects usually observed when measuring the photovoltaic performance of PSCs, organic fullerene C_{60} and fullerene-derivative phenyl-C_{61}-butyric acid methyl ester (PCBM) have been employed as ETMs resulting in enhanced device performance with reduced hysteresis effect as its helps passivate traps in the perovskite crystals grain boundaries [136]'[137]'[138]. Figure 2.5 shows the schematic structure of PCBM-ETM.

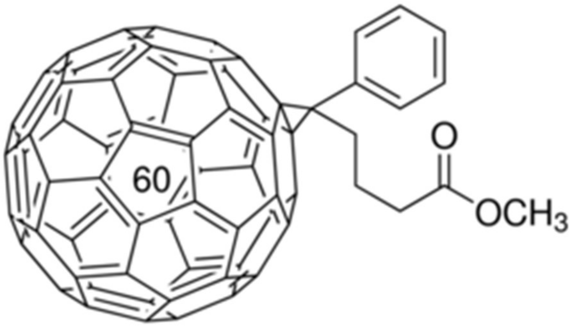

Figure 2.5: Structure of organic PCBM ETM [136]

PCBM is an n-type electron acceptor that has been widely used in organic photovoltaics (OPV) and polymer solar cells (PoSCs) both on rigid and flexible substrates [139]–[146]. Owing to its almost well aligned energy levels with the perovskite layer and the counter electrodes, PCBM exhibits high electrons transfer leading to efficient photovoltaic devices in the p-i-n inverted architecture. Its lowest unoccupied molecular orbital (LUMO) energy level is about 0.15 eV lower than the perovskite crystals CB, 0.4 eV higher than aluminum (Al) counter electrode and 1.5 eV above gold (Au) contact electrode leading to ease of electrons transport across the interfaces. This property has endeared its usage as ETMs layer by various groups working on PSCs. Its solution-processing technique at low temperature makes it highly suitable for flex-PSCs. Figure 2.6 shows the LUMO energy level matching between perovskite layer and Al contact electrode.

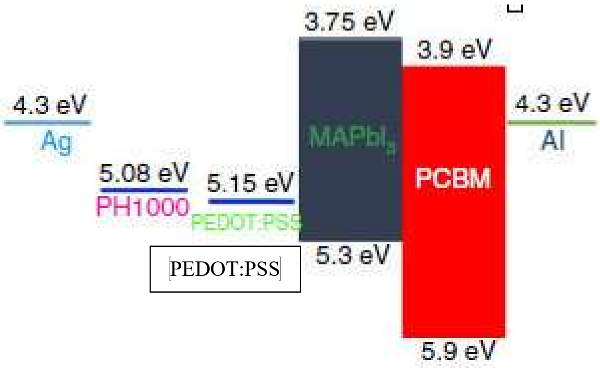

Figure 2.6: Energy level diagram of perovskite solar cell employing PCBM as ETM [147]

PCBM guarantees large area device fabrication [147]. Chiang *et al* [148] investigated the performance of fullerene C_{60} and PCBM on flexible substrates as well as the effects of their thicknesses on device parameters. PCBM with 20 nm thickness on flexible substrate (ITO-2) has the highest PCE of 4.54% and a good electron mobility leading up a J_{sc} of 7.93 mA cm^{-2} inferior only to C_{60} (30 nm) on ITO-2 with J_{sc} of 8.18 mA cm^{-2}. Expectedly, PCBM (20 nm) on rigid substrate (ITO-1) has the best *FF* of 69% slightly above its ITO-2 counterpart.

Ryu's group [149] successfully fabricated PCBM ETM flex-PSC using the regular n-i-p architecture via careful solvents engineering. Diethylether and 2-propanol were the suitable dripping solvents that do not degrade the PCBM and ensured quality film formations of the $CH_3NH_3PbI_3$-PCBM layer. PCBM had equally been used with other materials for dual-ETMs layer flex-PSCs [101]'[35]. Low-cost high electron mobility *N,N'*-dimethyl-3,4,9,10-tetracarboxylic perylene diimide (PTCDI)-ETM was reported by Kaltenbrunner *et al* [147]. PTCDI is greatly immune to degradation or bleaching and can produce enormous device yield as it forms homogeneous film over an extensive cell area deposited via vacuum-evaporation. It has deep highest occupied molecular orbital (HOMO), effective for blocking holes and guarantees excellent ambient stability.

2.3.4 Hole Transport Materials (HTMs) PSCs

Efficient holes collection is essential to avoid recombination, thus guaranteeing superior device performance. Though, perovskite crystals are unique ambivalent materials capable of generating electrons and holes as well as transporting them for current generation. Hence, different materials have been employed for efficient hole carriers transport with spiro-OMETAD leading the pack. HTMs-free PSC have been reported with modest device performance on both rigid and flexible substrates [105]. In the sections below, we review different HTMs used in flex-PSCs.

2.3.4.1 Spiro-OMETAD-HTMs PSCs

[2,2,7,7-tetrakis(N,N-di-p-methoxyphenyl-amine) 9,9-spirosbifluorene] also known as spiro-OMeTAD first used in solid-state dye-sensitized solar cells (s-DSSCs) as hole transport material (HTM) to replace liquid electrolytes has seen tremendous usage in PSCs [150]–[153]. Spiro-OMeTAD is a small amorphous organic molecule with intrinsically low hole carrier mobility ($\mu \sim 1.69 \times 10^{-6}$ cm^2 (Vs)$^{-1}$) and conductivity. For an efficient hole collection spiro-OMeTAD is doped with a p-type material usually Bis(trifluoromethane)-sulfonimide lithium salt (LiTFSI) to increase it conductivity and enhance holes transport via the oxidation of the spiro-OMeTAD molecule [151], [152]. It has a well matched band gap with perovskite crystal and high melting point, hence, its suitability as a HTM for PSCs [152]. PSCs have seen considerable usage of spiro-OMeTAD as a choice HTM, its solution-processability under low temperature also makes it compatible with flex-PSCs. However, spiro-OMeTAD is an expensive HTM with poor crystallinity and likely degradation under ambient environment [154].

In fabricating flex-PSCs, several groups have employed spiro-OMeTAD as HTM to achieve good device PCEs performance. Liu and Kelly in their pioneer work on flex-PSCs recorded a 10% PCE using spiro-OMeTAD as HTM [6]. Ever since, several groups have reported an average of above 12% PCEs for flex-PSCs with spiro-OMeTAD serving as holes collection materials [106],[108],[110],[126],[130],[155]. Yang's group achieved very high efficiency of 15.07% for flex-PSCs employing spiro-OMeTAD HTM on a large area greater than 10 mm [122].

Recently, Shi *et al* [153] synthesized single crystal spiro-OMeTAD for use as HTM in PSCs with inherently high mobility of holes. The triclinic single crystal shown in Figure 2.7 contains dual spiro-OMeTAD molecules with parallel p-p intermolecular stacking in its unit cell. The hole carrier mobility ($\mu \sim 1.39 \times 10^{-3}\ \mathrm{cm}^2\ (\mathrm{Vs})^{-1}$) of the single crystal spiro-OMeTAD is three orders of magnitude greater than the commonly used amorphous spiro-OMeTAD. Hence, single grystal spiro-OMeTAD could further enhanced PSCs device performance for both rigid and flexible devices.

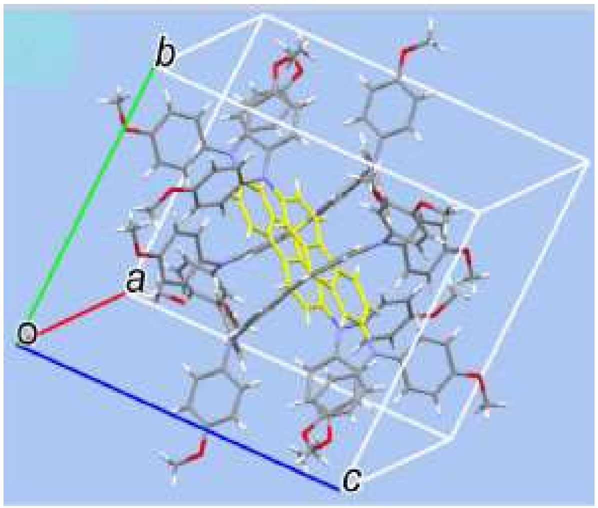

Figure 2.7: Single crystal structure of spiro-OMeTAD HTM [153]

2.3.4.2 Conductive Polymeric-HTMs Flex-PSCs

In quest to fabricate PSCs with less expensive and stable HTMs, several conductive polymeric substances have been utilized as replacement for spiro-OMeTAD molecule. Conductive polymeric HTMs are particularly suited for flex-PSCs as they are low temperature solution-processable and can exhibit good mechanical flexibility. Heo *et al* [2] reported modest PSCs device performance on glass substrates using poly-triarylamine (PTAA), poly-3-hexylthiophene (P3HT), (poly-[[9-(1-octylnonyl)-9H-carbazole-2,7-diyl]-2,5-thiophenediyl-2,1,3-benzothiadiazole-4,7-diyl-2,5-thiophenediyl]) (PCDTBT) and poly-[2,1,3-benzothiadiazole-4,7-diyl[4,4-bis(2-ethylhexyl)-4H-cyclopenta[2,1-b:3,4-b]dithiophene-2,6-diyl]] (PCPDTBT) as polymeric HTMs. Poly(3,4-ethylenedioxythiophene)/poly(styrenesulfonate) (PEDOT:PSS) is a relatively high conductive polymer that has been widely used in solar cells, light emitting diodes (LEDs), flexible displays and sensors [156]–[158]. Its conductivity ranges between order of 1 and 10^{-5} S cm^{-1} dependent on the ratio of PEDOT to PSS [158]. It has also found tremendous application as HTM in both rigid and flex-PSCs [159]. PEDOT:PSS is used in the inverted flex-PSCs architecture with a good alignment with PCBM where it transports holes across the flexible substrate. The group of Li [160] recorded PCE of 14% for flex-PSCs employing PEDOT:PSS HTM. The work function of PEDOT:PSS can be tuned to better align with the valence band of the perovskite film [161], thereby improving holes collection and consequently enhancing device performance.

PTAA is a conductive polymer with high hole carrier mobility, approximately ranging from 10^{-2} to 10^{-3} cm^2 $(Vs)^{-1}$. Its HOMO energy level is close to the valence band (VB) maximum of perovskite film and well aligned with gold (Au) electrode (as shown in Figure 2.8), hence, guaranteeing efficient holes collection and transport. Flex-PSC employing PTAA as HTM was first reported by Ryu *et al* [149] achieving a PCE of 11.1% on a PEN-ITO substrate with device parameters J_{sc} of 18.7 mA cm^{-2}, V_{oc} of 0.99 V and *FF* of 60%. Shin group [30] reported a remarkable PCE of 15.3% for PTAA-HTM flex-PSC in conjunction with ZSO-ETM and a PCE of 14.85% at steady state. PTAA-HTM based flex-PSC reached a steady-state PCE of 16.0% under 100 $mWcm^{-2}$ intensity of 1 sun [135].

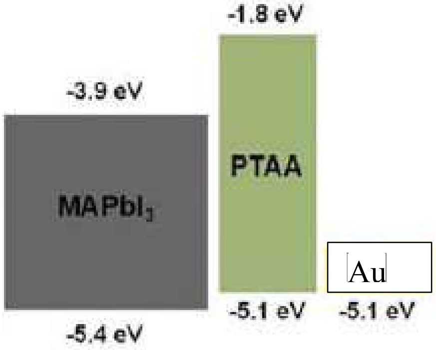

Figure 2.8: Energy band diagram of PTAA HTM utilized in perovskite solar cells [149]

Jo *et al* [162] introduced 1,4-bis(4-sulfonatobutoxy)benzene and thiophene moieties (PhNa-1T) conductive polymer with conductivity of 2.6 × 10^{-4} S cm^{-1} as HTM for flex-PSC in inverted device architecture. PhNa-1T (structure shown in Figure 2.9) exhibits good hole transport in the direction of out-of-plane with a high work function (5.2 eV) that is close to the perovskite film VB appropriate for formation of Ohmic contact between the two layers. It is solution-processable at low temperature forming a smooth surface with relatively low root mean square (RMS) roughness on PEN-ITO flexible substrate advantageous for good interaction between the HTM and perovskite layer.

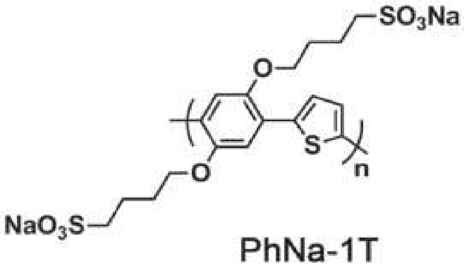

Figure 2.9: PhNa-1T HTM molecular structure [162]

2.3.4.3 Inorganic-HTMs PSCs

Owing to their high cost and short term stability, organic-HTMs would be desired to be replaced with inexpensive, easily synthesized and more stable p-type inorganic semiconducting transparent HTMs. The use of p-type semiconductors such as copper thiocyanate (CuSCN), copper iodide (CuI) and nickel oxide (NiO) as HTMs for PSCs on rigid substrates have been reported in literatures [163]. NiO is a wide gap p-type metal oxide with cubic crystal structure [163]. As a result of its good hole carrier conductivity and solution processing potential at room temperature it was utilized as HTM for flexible organic solar cell (flex-OSC) on PET-ITO flexible substrate via sputtering with a modest

PCE of 2.5% [164]. Its large VB energy of 5.45 eV adequately matched that of perovskite film in inverted device architecture creating proper Ohmic-contact between their layers. Hence, its suitability as an efficient HTM that can provide improved device performance.

In their work, Choy and co-workers [165] reported the first NiO_x inorganic semiconducting HTM on flexible substrate. They synthesized NiO_x nanocrystals (NCs) ink by dispersing different quantities of NiO_x-NCs in deionized water to obtain varying concentrations. The NiO_x-NCs ink was used to fabricate room temperature solution-processed surface-nanostructured and flawless NiO_x film via spin-coating for high-performance flex-PSC exhibiting adequate stability. Recombination due to monomolecular Shockley-Read-Hall and $NiO_x/CH_3NH_3PbI_3$ interface can be significantly reduced by the surface-nanostructured and flawless NiO_x film. Both steady state photoluminescence (ss-PL) and time resolved photoluminescence (TRPL) showed very fast quenching for NiO_x better than PEDOT:PSS as shown in Figure 17 establishing the hole carrier extraction at the NiO_x-NCs/$CH_3NH_3PbI_3$ interfacial layer leading to high current density (J_{sc}) value. The device performance of the NiO_x-HTM flex-PSC are J_{sc} of 20.66 mA cm^{-2}, V_{oc} of 0.997 V, *FF* of 70.5% and a high PCE of 14.53%.

Yin *et al* [103] reported the spin-coating of NiO_x NPs dispersed in deionized water on a PEN-ITO flexible substrate to form NiO_x films. The spin-coating speed was 2000 rpm and lasted for 30 s. The film underwent thermal treatment at 130°C in ambient air for 20 min. They noted that the high transmission of the PEN-ITO was nearly retained after deposition of NiO_x. A PCE of 13.43% (13.29% at steady state) was recorded with J_{sc} of 18.74 mA cm^{-2}, V_{oc} of 1.04 V and *FF* of 68.9%.

CuSCN is a low cost, chemically stable and high hole carrier mobility (of approximately ranging from 0.01 to 0.1cm^2 (Vs)$^{-1}$) p-type semiconductor which is transparent across the visible and near-infrared spectral of light [166]. With its high VB of 5.3 eV comparable with both perovskite film VB (5.4 eV) and work function of Au (5.1 eV) contact electrode and solution-processability at low temperature, CuSCN have been employed as HTM in both N-I-P normal [167] and P-I-N inverted [168], [169] architecture with superior PCEs recorded of up to 16.6% on rigid substrate. These properties make CuSCN a potential HTM candidate for flex-PSCs.

CuO_x and CuI are also low-cost, chemically stable and low-temperature solution-processable inorganic-HTMs having VB energies 5.1 eV and 5.2 eV respectively with demonstrated high PCEs for rigid-PSCs [170]–[173]. Their performances on flexible substrates need to be investigated, as they meet the requirements for deployment in flex-PSCs. Inorganic-HTMs could ultimately replace organic-HTMs and fast-track the commercialization of both rigid and flex-PSCs.

2.3.4.4 Carbon-based-HTMs Flex-PSCs

Carboneous materials such as grapheme oxide (GO), reduced-graphene oxide (r-GO) and carbon nanotubes (CNTs) have found applications in PSCs as HTMs with impressive device performances [174], [175]. Yusoff *et al* [176] tuned the work function (WF) of GO with addition of varying concentration of silver trifluoromethanesulfonate (AgOTf). The WF-tuned GO was subsequently used as hole interfacial material (HIM) in conjunction with PEDOT:PSS-HTM in the fabrication of rigid and flex-PSCs. The devices fabrication utilized spin-coating solution processing technique and annealin treatment of not more than 120°C. GO with properly tuned WF should be suitable for deployment as a standalone HTM in flex-PSCs with appreciable performance.

2.3.5 PSCs Contact Electrodes

Au, Ag, and Al are the most widely used contact device electrodes [177]. They are highly conductive and possess high work-functions that ensured formation of Ohmic contact with layer unto which they are deposited preventing Schottky junction formation. Ag and Al have higher reflectance coefficient than Au and alloyed AgAl contact electrode has been reported for rigid-PSC [178]. Usage of metal-based electrodes has also been reported widely for flex-PSCs. These metal contact electrodes are thermally deposited under high vacuum environment on devices limiting large area fabrication of flex-PSCs and consequently hindering commercialization potentials. Au and Ag are expensive metals that should be replaced in favour of low-cost contact electrode materials for flex-PSCs. Non-thermally deposited, inexpensive electrodes such as laminates plastic/metal-mesh and carbon-based electrodes are recently being used for the fabrication of flex-PSCs [179]. These types of electrodes would lead the way to commercialization of flex-PSCs as they support large scale production for roll-to-roll and printable flex-PSCs owing to their flexibility, transparency, chemical stability, good conductivity and matching energy levels with PSCs materials.

Laminate plastic/metal-mesh electrodes are transparent, flexible and highly conductive. PSCs utilizing laminate electrodes are fabricated in two steps with the perovskite layer deposited on one substrate (rigid or flexible) while the counter electrode with or without HTM is laminated on it. By this technique large area rigid and flex-PSCs can somewhat easily be manufactured. Troughton *et al* [120] synthesized pliable plastic/metal-mesh laminate that comprised Ni embedded PET film over which PEDOT:PSS and pressure sensitive adhesive mixture was deposited via doctor-blading. The prepared laminate was thermally treated at 60 ºC for 15 min. The fabrication of the flex-PSC was completed as shown in Fig. 18 by laminating the (PET-Ni)-PEDOT:PSS+conductive-Adhesive through hot-pressing (after heating at 120 ºC for 5 min) with finger pressure on the Ti-foil-(TiO_2-Al_2O_3)-$CH_3NH_3PbI_3$-spiro-OMeTAD making contact with the Ti-foil. An impressive PCE of 10.3% was reported for the device. Makha and co-workers [180] replaced Ni with 100 nm thick Ag-mesh and employed sorbital as conductive adhesive layer, thereby producing (PET-Ag)-PEDOT:PSS+sorbitol laminate. Their laminate was annealed at 120°C for 10 min for lamination on the HTM layer with application of finger pressure. The PSC device fabricated on glass-FTO substrate showed a decent PCE of 7.6%.

Carbon-based top electrodes such as CNT, carbon-black/graphite composite and grapheme have been reported for PSCs with good performance [174]'[175]. Wong *et al* [181] synthesized CNT laminate by the floating chemical deposition technique in a tube furnace. The as-synthesized CNT laminate was placed on taped-FTO substrates containing perovskite layer with and without HTM layer. Toluene drops were severally added to moist the CNT laminate and the perovskite surface. Cotton stick was used to clean the area where CNT film is not needed after toluene dried up. To ensure better electrical contact the CNT and FTO were soldered. The photovoltaic performance of the devices were measured under 100 mW cm^{-2} of AM 1.5 irradiation. The HTM-free device recorded a PCE of 6.29%, while the spiro-OMeTAD-HTM device had a PCE of 9.90%. Flex-PSCs utilizing CNT laminate was reported by Wang's group [98] using similar procedure demonstrated by Wong and co-workers. Flexible Ti-foil substrate was used in their work with a PCE of 8.31% under irradiation of AM 1.5G 100 mW cm^{-2}.

Due to the versatility of CNT laminate electrode, Qui *et al* in two separate publications reported the use of CNT sheet electrode in fiber-shaped flex-PSCs. After deposition of ETM, perovskite film and HTM according to the procedures reported in their work on stainless steel wire [121] and Ti-wire [125], CNT sheet was wrapped around the devices to complete the flex-PSCs. To guarantee proper contact between the CNT sheets and the perovskite layer, the produced fiber-shaped flex-PSCs were dipped in isopropanol and afterward dried at 80ºC for 30 min. The devices recorded PCEs of 3.3% and 3.6% respectively. The device structure is depicted in Figure 2.10.

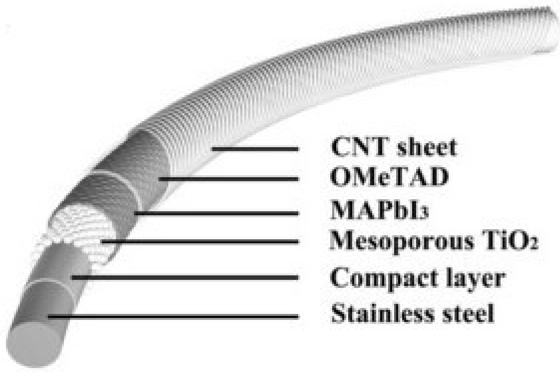

Figure 2.10: CNT back contact fiber perovskite solar cells [121]

In another report, Wei *et al* [182] used highly conductive flexible thermoplastic free-standing carbon electrode that is inexpensive with easy low temperature (below 100°C) preparation method for the fabrication of PSC. The carbon electrode comprised of carbon pastes with varying weight percent of carbon-black powder and graphite flake (80% total) and 20wt% polyvinyl acetate (PVAc). The flexibility of the carbon film was investigated by repeated bending for 50 times without any noticeable damage. The resistance before and after bending varied slightly demonstrating that the carbon film is highly flexible. The electrode was hot-pressed onto the perovskite layer for the fabrication of HTM-free PSCs. The hot-pressing procedure improved the conductivity of the carbon electrode by reducing its resistivity. The optimized carbon film components and applied hot-press pressure achieved high PCE of 13.53%. This electrode qualifies for deployment in flex-PSCs for good performance and flexibility.

Flexible multi-layered graphene (MG) on top of perovskite film with no HTM was reported by Yan's group [183] with PCE of 11.5% achieved. The MG was excellently mounted on the perovskite layer with chemically reactive graphene-CH_3NH_3I paste. It enhanced hole collection and blocked electron via a Schottky barrier, greatly hindering charge recombination at the interface. The tremendous characteristics and performances exhibited by carbonaceous electrodes make all-carbon-electrodes (bottom and top) flex-PSCs that are cheap, stable, high performing and mechanically robust a possibility.

2.3.6 Stability

Stability and durability are important factors for the possible commercialization of PSC as $CH_3NH_3PbI_3$ is known to degrade in the presence of moisture and ultraviolet radiation which characterized outdoor deployment of photovoltaic devices [5] and [10]. The stability of PSC is determined by the tolerance *t*-factor which is the ratio of the distance between A-X to that between B-X [11].

$$t = \frac{(R_A + R_X)}{\sqrt{2}(R_B + R_X)} \qquad (1).$$

Hui Seon et al [16] reported a stable PSC that was subjected to 500 h stability test with an improved 14% PCE for his solar cell after 200 h due to an increment in the form factor. Anyi et al tested for stability for over 1000 h in an outdoor operating environment after achieving a PCE of 12.8%.

Materials variations have also been reported in so many literatures to achieve higher PCE and help improved stability.

2.3.7 Mechanism of perovskite solar cell

Electron beam induced current EBIC has been used to investigate the cross-section of $CH_3NH_3PbI_{3-x}Cl_x$ [5], [24]. The absorber material generates electron-hole pairs when the electron beam is directed to it, these electron and hole are separated and photocurrents are induced inside the cell [24]. Arianna et al [25] gave a comprehensive plausible reaction mechanism for a $CH_3NH_3PbI_{3-x}Cl_x$ embedded into a mesoporous TiO_2 with spiro-OMeTAD acting as organic hole-transport-layer (HTL).

The reaction equation of primary charge separation due to injection of electron:

$$(e^- \ldots h^+)_{CH3NH3MetalI3} \longrightarrow e_{CB}^-{}_{(metal\ oxide)} + h^+{}_{(CH3NH3MetalI3)}$$

$$h^+(_{CH3NH3MetalI3}) \longrightarrow h^+_{(HTL)} \qquad (2a).$$

The reaction equation of primary charge separation due to injection of hole:

$$(e^- \ldots h^+)_{CH3NH3MetalI3} \longrightarrow h^+(HTL) + e^-(_{CH3NH3MetalI3})$$

$$e^-(_{CH3NH3MetalI3}) \longrightarrow e_{CB}^-{}_{(metal\ oxide)} \qquad (2b).$$

The electron-hole exciton annihilation equation is given by:

$(e^{-} \ldots h^{+})_{CH3NH3MetalI3} \longrightarrow hv$ (3).

$(e^{-} \ldots h^{+})_{CH3NH3MetalI3} \longrightarrow \nabla$ (4).

Charge recombination occurs at the metal oxide/HTL interface and it is given as:

$$e_{CB}^{-}{}_{(metal\ oxide)} + h^{+}{}_{(HTL)} \longrightarrow \nabla \quad (5)$$

They posited that charge separation primarily occur at the two junctions with metal oxide and the HTL concurrently. Photoexcitation of the perovskite creates injection of extremely fast electron and hole at the same time [25]. Recombination of electron and hole to form exciton is reported to be slow due to long path length of the perovskite [5, 24-25] and mobility of current carriers are high up to time scale of microsecond [30]. Figure 2.11 demonstrates the charge transfer mechanism in PSC.

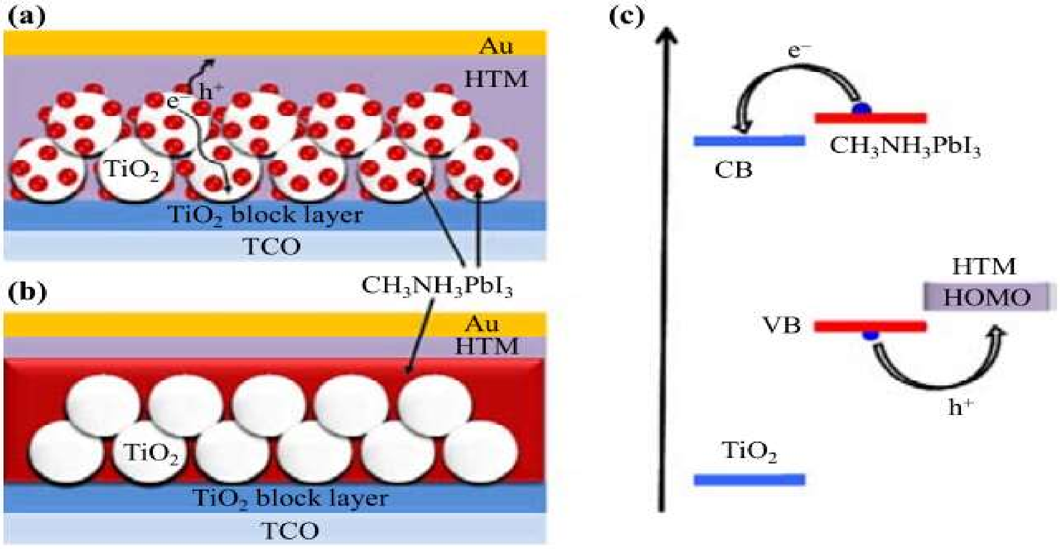

Figure 2.2.31: Schematic showing mechanism of perovskite solar cell [12]

CHAPTER 3

MATERIALS AND METHODS

3.1 Materials

Platinic (H_2PtCl_6) acid, ethylene glycol (EG) purriss grade, fluorine-doped tin oxide (FTO) glass (7 Ωsq^{-1}) and indium-doped tin oxide coated polyethylene terephthalate ITO-PET (14 Ωsq^{-1}) were purchased from Sigma Aldrich. Acetone, 2-propanol and methanol were all purchased from Sigma Aldrich. Ti-Nanoxide T/SP paste, N719 sensitizer, Iodolyte Z electrolyte were all products of Solaronix, Switzerland.

3.2 Photofabrication of Platinum (Pt) Counter Electrodes

The photofabrication process involves the use of UV light for the reduction of platinic acid precursor to platinum (Pt) metal.

FTO and ITO-PET substrates were cleaned successively using detergent, deionized (DI) water, acetone and 2-propanol for 1 hour by ultrasonication process using Branson 3510. The substrates were heated at 70 ºC for 20 min to completely remove the organic cleaning agents. 0.02 M H_2PtCl_6 solution in EG was prepared. The H_2PtCl_6 readily dissolved in the EG solvent at room temperature. 20 ul of the platinic acid solution was then spin coated on the pre-cleaned FTO substrate with an exposed area of 0.25 cm^2 at 2000 rpm for 45s using Specialty Coating System (SCS) 6800 spin coater series. Figure 3.1 shows both the exposed area of the FTO and the platinic acid precursor. The H_2PtCl_6 solution coated FTO substrate was then exposed to UV irradiation using Lumen Dynamics Omnicure series 2000 at 2 W cm^{-2} in an ambient environment for a specific duration of time. The UV light intensity temperature was measured by an homemade Arduino-based temperature sensor. The maximum temperature recorded at UV light intensity of 2 W cm^{-2} was 40 ºC.

Figure 3.1: Photographic images showing an exposed area of 0.25 cm^{-2} of FTO covered with scotch tape (left) and ethanolic platinic acid solution (right)

3.3 Pulsed laser Ablation Synthesis

In this experiment the pulsed laser ablation setup comprises of a solid state Q-switched Neodymium-doped Yttrium Aluminum Garnet [$Nd:Y_3Al_5O_{12}$ (Nd-YAG)] laser operating in the second harmonics with a wavelength of 532nm, a prism, a convex lens with focal length of 1m, beaker containing liquid, magnetic stirrer and magnetic rotator. The Neodymium ion Nd(III) provides the lasing activity while the YAG serves as the host crystal structure for the Nd-YAG brilliant laser. The laser delivered had energy of 290mJ measured using power meter, a pulse width of 5ns and operates at a 10Hz pulse repetition rate. The laser was focused towards the Cu powder sample dispersed in water inside a beaker placed on a magnetic rotator with the aid of the prism and convex lens. Figure 3.2 below shows the schematic diagram of the setup.

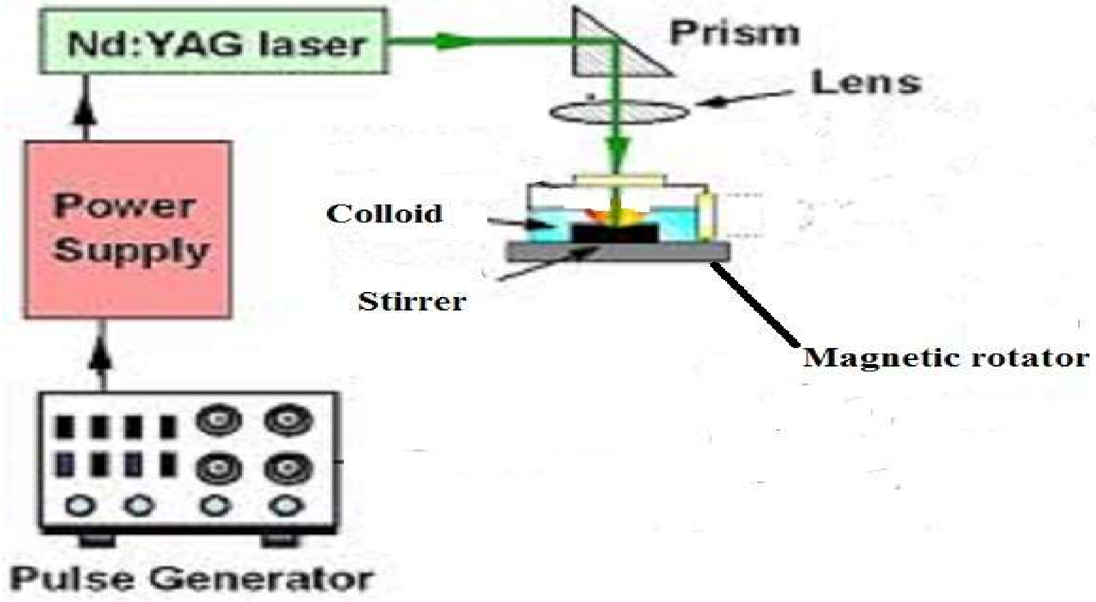

Figure 3.2: Pulsed laser ablation in liquid experimental setup

3.4 Dye Sensitized Solar Cells Fabrication

Dye sensitized solar cells were fabricated using the photofabricated Pt CEs. The procedures for the fabrication of the different components of the DSSCs such as the photoanodes, dye sensitizer preparation, and DSSCs components coupling are described below.

3.4.1 TiO_2 Photoanodes Fabrication

TiO_2 photoanodes were prepared by blade coating Ti-Nanoxide T/SP paste on an 0.25 cm^2 exposed area of a precleaned FTO glass. The 0.25 cm^2 exposed area was achieved by covering the FTO glass with scotch tape leaving only an area of 0.25 cm^2 for coating of TiO_2 photoanode. The TiO_2 coated FTO was heated at 450 ºC for 30 mins on a hot plate in open air. Prior to the heating, the masking scotch tapes were removed. After the TiO_2

paste had been baked for 30 mins, the TiO_2 photoanode was allowed to cool down gradually to room temperature. The samples were then soaked in N719 dye for 24 h.

3.4.2 ZnO Flexible Photoanode Fabrication

For the flexible photoanode DSSCs, ZnO semiconducting was employed due to its low temperature processing potential. ZnO dispersion in butanol was utilized for coating on ITO-PET. Prior to coating, the ZnO dispersion was stirred for 2 h at 60 ºC to achieve needed viscosity for a paste-like ZnO, which was then blade coated on ITO-PET and sintered at 120 ºC. The sample was allowed to cool to room temperature before being immersed in N719 dye for 24 h.

3.4.3 CuO Photocathodes Fabrications

For the p-type DSSCs, the as-synthesized pulsed laser ablated CuO colloid was centrifuged at 1000 rpm for 5 min to remove the water used for the synthesis. The as-synthesized CuO was further washed with ethanol and centrifuged to ensure the water used for the synthesis has been removed. The as-synthesized CuO was then dispersed into ethylene glycol (EG) and stirred for 3 days at a temperature of 90 ºC to achieve appropriate viscous CuO. 10 ul of the EG dispersed CuO was drop-coated on an exposed 0.25 cm^2 precleaned FTO. The coated sample was heated at 500 ºC for 30 min and allowed to cool to room temperature before being immersed in N719 prepared in three solvents of EG, methanol and propanol.

3.4.4 N719 Dye Solution Preparation

N719 dye sensitizer was dissolved in three different solvent of ethylene glycol, methanol and propanol. The solutions were sonicated for 30 min to dissolve the N719 dye. N719 prepared with methanol was used for all TiO_2 photoanodes and ZnO flexible photoanode. Meanwhile, all N719 dye prepared in all the three solvents were used for p-type CuO photocathode in investigating the effects of these solvents on the photovoltaic performance of p-type CuO DSSC.

3.4.5 Dye Sensitized Solar Cells Coupling

The DSSCs fabrication was completed by coupling the photoanodes and the photofabricated Pt CEs in the case of the n-type TiO_2 based DSSCs using acrylic super glue gel. Triiodide/iodide electrolyte was introduced into the cells before being hand pressed to seal the electrolyte in between the electrodes and completing the cells fabrication. For the p-type CuO based DSSCs, the CuO photocathode and Pt CEs were coupled using with the aid of clips. Iodine based electrolyte was injected into the cells by capillary effect. The cells were left for some minutes prior to measuring the IV characteristics.

3.5 Perovskite Solar Cells Fabrication

The procedure for the fabrication of mixed cation and mixed halides perovskite solar cells are detailed in the subsections below.

3.5.1 Preparation of TiO_2 Compact Layer

TiO_2 compact hole blocking layer was prepared by diluting 369 ul of titanium isopropoxide in 2.53 ml of isopropanol in a glass bottle. 35 ul of 2 M HCl was diluted in 2.53 ml of isopropanol in another glass bottle to achieve 0.013 M of HCl. The two solutions were then mixed under stirring to obtain 0.23 M of titanium isopropoxide solution. The solution was tightly sealed as it is an anhydrous solution and to precipitate when exposed to air and moisture.

3.5.2 Preparation of TiO_2 Mesoporous Layer

Mesoporous TiO_2 layer material was prepared by diluting Ti-Nanoxide T/SP in ethanol at 2:7 mass ratio. The mixture was sonicated for 30 min in a Branson ultrasonic bath before being used for the fabrication of perovskite solar cells.

3.5.3 Preparation of Spiro-OMeTAD Hole Transport Layer

Spiro-OMetAD was used as hole transport material in the fabrication perovskite solar cells. The spiro-OMeTAD was prepared by mixing 90 mg of spiro-OMeTAD, 36 ul of 4-Tpd and 22 ul of 520 mg/ml of predissolved liTFSI (in 1 ml Acetonitrile) in 1 ml of anhydrous chlorobenzene at room temperature.

3.5.4 Synthesis of Cesium trimethyl ammonium mixed halides

Cesium trimethyl ammonium mixed halides were synthesized by mixing two different ratio of CsCl and methyl ammonium iodide (MAI) with bismuth triiodide (BiI_3) to make sample 1 and sample 2 of the mixed cation and mixed halides lead-free perovskite solar cells. Sample 1 contains 0.02384 g of CsCl, 0.21456 g of MAI (making CsCl:MAI mass ratio of 1:9) and 0.5838 g BiI_3. While sample 2 contains 0.07152 g of CsCl, 0.16688 g of MAI (making CsCl:MAI mass ratio of 3:7) and 0.5838 g BiI_3. The two samples were dissolved at room temperature without stirring in dimethyl formamide (DMF) and dimethyl sulfoxide (DMSO) at the solvent volume mixing ratio of 9:1. It was observed that the samples readily dissolved in the solvents within 10 min. Figure 3.3 illustrates the synthesized cesium trimethyl ammonium mixed halides at the given ratio.

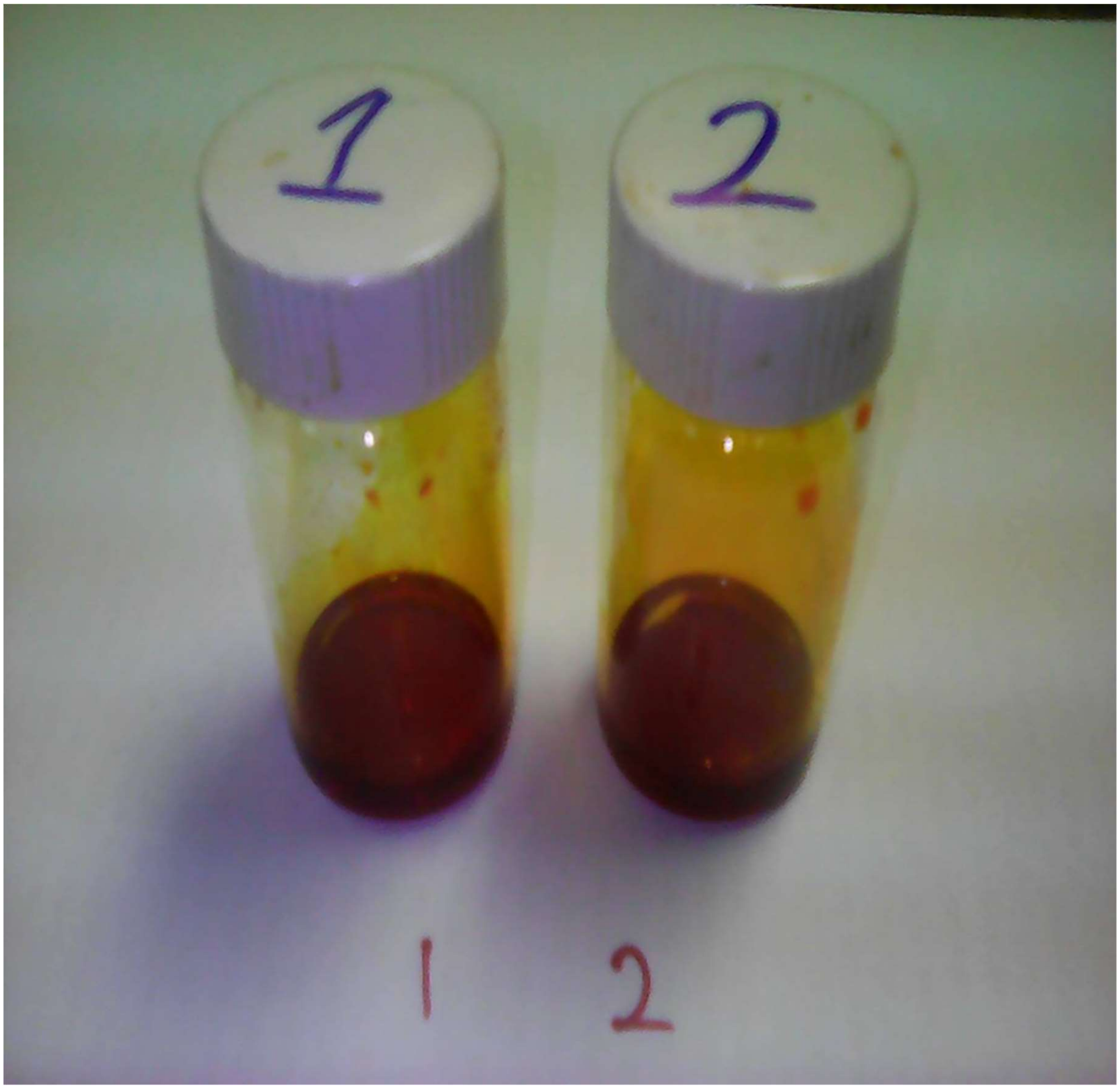

Figure 3.3: Photographic images showing the synthesized solution of mixed cations and mixed halides bismuth perovskite 1) CsCl:MAI @ 1:9 and 2) CsCl:MAI @ 3:7

3.5.5 Fabrication of Cesium trimethyl ammonium mixed halides lead-free perovskite solar cells

FTO transparent conductive glasses of 2 cm by 1 cm were pre-patterned by etching one edge of the samples using zinc power and 2 M HCl. For the etching process, zinc powder was spread on one edge of the FTO glass followed by dropping of HCl on the zinc power covered area of the glass. After the reaction bubbles have settled down, the FTO glasses were washed with deionized water. The FTO glasses were then cleaned successively in ultrasonic bath with deionized water, acetone and ethanol for 1 h. On completion of the ultrasonic cleaning, the samples were thermally treated in oven at 120 ºC for 30 mins in order to remove the organic solvents used in cleaning process.

Figure 3.4 shows a schematic of the fabrication process of the mixed cation and mixed halides bismuth perovskite solar cells. 0.4 cm of the unetched edge of the FTO glasses were covered with scotch tape (to be used as anodic contact point) before being mounted on a spin coater for the deposition of TiO_2 compact layer. 50 ul of the prepared titanium isopropoxide solution was spin coated at the rate of 3000 rpm for 40 s in nitrogen environment. The TiO_2 compact layer coated FTO glasses were sintered at 450 ºC for 30 min and allowed to cool down gradually. Following the same procedure used for the deposition of the TiO_2 compact layer, mesoporous TiO_2 was coated on the FTO-TiO_{2CL}. The mesoporous TiO_2 was thermally treated at 450 ºC for 45 min on an hot plate in ambient air environment and allowed to gradually cool down to room temperature.

The mixed cation and mixed halides cesium methylammonium bismuth triiodide perovskite was deposited by a one-step spin coating technique at the rate of 2000 rpm for 30 s in an argon filled glove box. The perovskite samples were annealed at 110 ºC for 10 min inside the glove box. After the samples cooled down to room temperature spiro-OMeTAD solution was spin coated on them at 3000 rpm for 30 s and thermally treated at 100 ºC for 15 min in the glove box. The samples were removed from the glove box after the hot plate reached 25 ºC. the samples were masked with metal masks for deposition of gold (Au) back contact layer using gold thermal evaporator. 60 nm Au back contact was coated on the samples under vacuum.

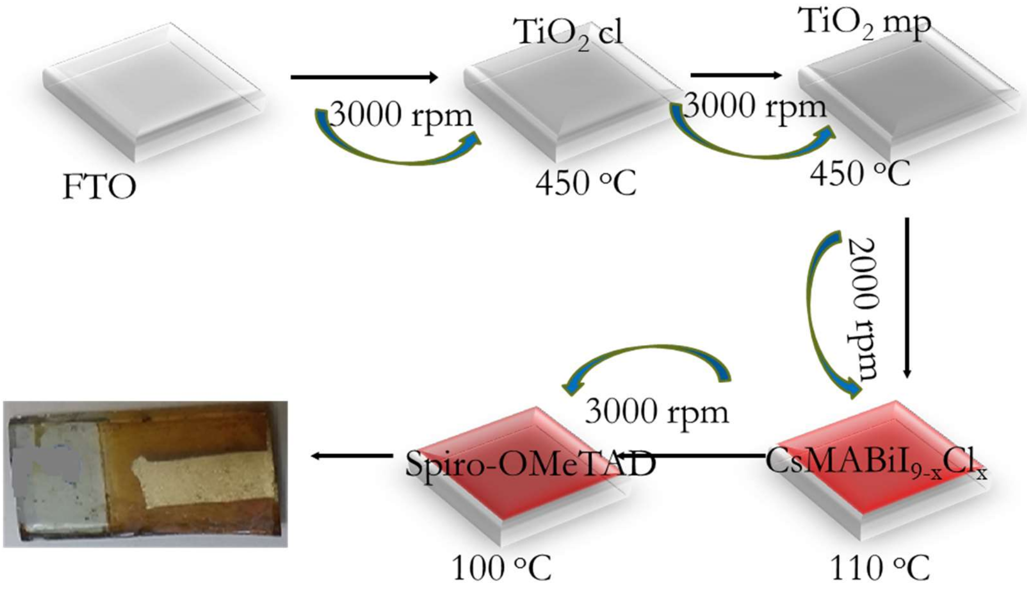

Figure 3.4: Fabrication steps for the mixed cation and mixed halides bismuth perovskite solar cells

3.6 Characterization techniques

3.6.1 Optical Characterization

i. The UV-Vis. absorption and transmittance spectra of the synthesized and fabricated samples were recorded using the Jasco 670 double beam spectrophotometer available in the Laser Research Laboratory of Physics department of King Fahd University of Petroleum and Minerals.

ii. The photoluminescence (PL) spectra of the synthesized samples and fabricated solar cells were obtained using Fluorolog FL#-iHR, HORIBA Jobin Yvon with Xenon lamp light source having 350nm excitation wavelength.

3.6.2 Structural Characterization

This X-ray diffraction (XRD) is a valuable technique used for the investigation of crystallinity and phase identification of a material. Analysis of XRD results can be used to determine the crystal structure, crystallite size and sample identification. XRD involves irradiation of a sample with X-ray beams of known wavelength and measurement of the diffraction of the beam at a certain angle (θ). The inter-atomic d-spacing is calculated using the Bragg's formula:

$$n\lambda = 2d\sin\theta \qquad (6).$$

XRD pattern uniquely identifies different crystalline materials. The XRD analysis of the synthesized materials was conducted on Rigaku mini-XRD with CuK_{α} radiation source having wavelength λ=0,1540 nm at a scanning rate of 2 ^{0}/min within 2θ range.

3.6.3 Morphological Characterization

i. Field Emission Scanning Electron Microscopy

The scanning electron microscope is a device used for the investigation of the structure, composition and defects in materials. The SEM images are obtained by scanning high energy electron beam on the surface of the sample. The principle of operation of SEM is such that signals are generated from the surface of a sample in its solid state when electron beam of high energy is focused on the sample. The image obtained reveals the morphology, orientation and the composition of the sample. A conventional SEM is able to measure areas within 1centimeter to 5 microns in dimension of width with magnification to approximately 30000x. Meanwhile, a field emission scanning electron microscope (FESEM) can additionally provide elemental and topographical information at 10^6 order of magnitude.

The synthesized samples morphologies were studied using Lyra TESCAN FESEM.

ii. Transmission Electron Microscopy (TEM)

This technique entails a process in which highly accelerated electrons transmit through a nanometer thickness sample while interacting with the sample to generate magnified images which is focused on a fluorescent screen. When electrons are absorbed by the sample at small magnification, an image contrast occurs and this is determined by the sample thickness and elemental composition.

FEI titan 80-300 CT TEM instrument was utilized to obtain the TEM images, high-resolution TEM (HRTEM) and selected area electron diffraction of the synthesized samples.

3.6.4 Compositional Characterization

Please X-ray photoelectron spectroscopy (XPS) would be employed as a spectroscopic technique for the investigation of the elemental compositions, electronic states and chemical states of the elements in the synthesized materials. It involves the measurement of kinetic energy of ejected photoelectron due to the irradiation of the surface of a sample by an X-ray beam. The XPS working principle is governed by the equation below:

$$B.E = h\nu - (K.E + \phi) \qquad (7).$$

Where B.E is the binding energy of the valence electrons of the sample which is unique for different element, $h\nu$ is the energy of the incident X-ray beam targeted to the sample, K.E is the kinetic energy of the photoelectron ejected from the surface of the sample and ϕ is the work function of the XPS analyzer.

ESCALAB-250Xi system (Thermos-Scientific) with Al Kα radiation (hν = 1486.6eV) was utilized for the XPS of the synthesized materials. Spectra acquisition was done using a constant energy mode with pass energy of 100 and 30 eV for the survey and the narrow scans, respectively. The analysis chamber base pressure was 4×10^{-10} mbar. The data acquisition was carried out using Thermo-Scientific Avantage software was used to acquire the XPS data.

3.6.5 Electrochemical Impedance Spectroscopy (EIS)

The electrochemical impedance spectroscopy measurement of samples was carried using Autolab PG302N potentiostat equipped with NOVA 1.11 and NOVA 2.1 software. The Nyquist plot of the impedance parameters and Tafel plots were carried out on the system. The operating frequency range from 0.1 Hz to 100 kHz at a voltage scan rate of 10 mV/s.

3.6.6 Cyclic Voltammetry

To study the catalytic activity of photofabricated Pt CE samples, three electrodes cyclic voltammetry measurement was conducted. Saturated calomel electrode served as the reference electrode, platinum plate electrode was used as the counter electrode while the photofabricated Pt electrodes served as the working electrodes in the setup. The electrolyte used contained 0.1 M lithium perchlorate ($LiClO_4$), 0.01 M lithium iodide (LiI) and 0.001 M iodine (I_2) all in acetonitrile (AN) solvent. The operating potential for the CV measurement ranges between -0.5 V to 1 V. The CV measurement was carried out on Autolab PG302N equipped with NOVA 2.1 software.

3.6.7 I-V Characteristics

The I-V characteristics of the photovoltaic performance of the fabricated DSSCs utilizing photofabricated Pt CEs were measured using Autolab potentiostat PG302N equipped with NOVA 1.11 software. Oriel lamp solar simulator calibrated to 100 mW cm^{-2} was used as light illumination source for the I-V characteristic measurement. An area of 0.25 cm^{-2} was exposed for the measurement.

3.7 Estimation of solar cell physical parameters

The perovskite solar cell can be modeled as a PN junction solar cell and its characteristic developed as shown in Figure 3.5 and the mathematical model given below:

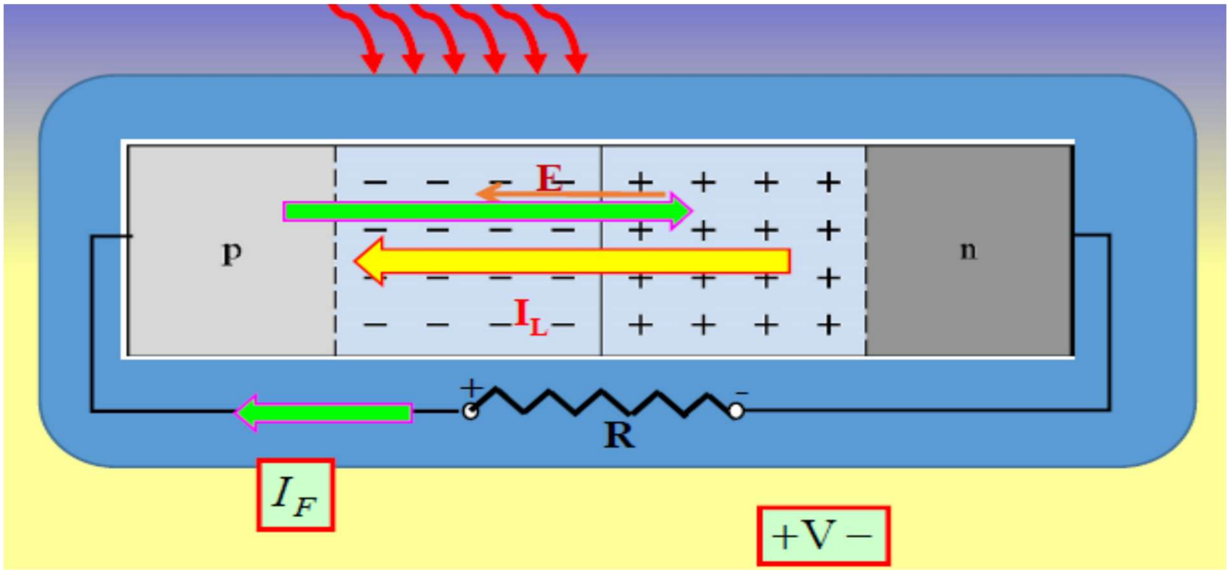

Figure 3.5: Solar cell modeled with PN junction device

As incident photons strike the perovskite solar excitons are photogenerated in the space charge region and dissociate into electron and hole carriers. The rate at which electron-hole pairs are generated are given as [31-32]:

$$g' = \frac{\propto I_{v\,(x)}}{hv} \qquad (8).$$

Where $g^{'}$ is excitons generation rate, $\propto$ is absorption coefficient, $I_v(x)$ in photons intensity after a thickness x, and hν is the energy of the photons.

The electron-hole pair set up an electric field in the space charge region. This drives the generated electrons and holes out of the space charge region through drifting and diffusion as a photocurrent I_L. The photocurrent produces a forward biased voltage across the resistive load, which in turn produces a forward biased current I_F. The net current in the device is in the reverse direction and it is as given below [31-32]:

$$J = J_L - J_F \tag{9.}$$

$$J = J_L - J_S[\exp(\frac{eV}{kT}) - 1] \tag{10.}$$

For short circuit current J_{SC}, R = 0, V = 0

$$J = J_{SC} = J_L \tag{11.}$$

At open circuit

$$J = 0 = J_L - J_S[\exp(\frac{eV_{oc}}{kT}) - 1] \tag{12.}$$

The open circuit voltage V_{OC} is derived as

$$V_{OC} = \frac{kT}{e}\ln[1 + \frac{J_L}{J_S}] \tag{13.}$$

$$V_{OC} = V_t\ln[1 + \frac{J_L}{J_S}] \tag{14.}$$

where J_S is calculated from the expression written below:

$$J_S = \frac{eD_p p_{n0}}{L_p} + \frac{eD_n n_{p0}}{L_n} \tag{15.}$$

$$J_S = en_i^2\left[\frac{D_p}{N_d L_p} + \frac{D_n}{N_a L_n}\right] \quad (16).$$

and

$$p_{n0} = \frac{n_i^2}{N_d},\ n_{p0} = \frac{n_i^2}{N_a} \quad (17).$$

$$L_n = \sqrt{D_n \tau_{n0}},\ L_p = \sqrt{D_p \tau_{p0}},\ D = \frac{\mu kT}{e},\ \mu = \frac{v_d}{E} \quad (18).$$

For non-ideal solar cell, R_S is not equal to zero and R_p is not infinite. The net current density is governed by the following equation:

$$J = J_L - J_S\left[\exp\left(\frac{eV+JA\ \ _S}{kT}\right) - 1\right] - \frac{V+JAR_S}{R_p} \quad (19).$$

where

J_S – saturation current density

J_{SC} – short circuit current density

J_L – photocurrent density

J_F – forward biased current density

T – 300K at room temperature

L_n – electron minority carrier diffusion length

L_p – hole minority carrier diffusion length

n_{p0} – electron minority carrier concentration in the p-region at thermal equilibrium

p_{n0} – hole minority carrier concentration in the n-region at thermal equilibrium

D_n – electron diffusion rate

D_p – hole diffusion rate

N_d – donor dopant concentration

N_a – acceptor dopant concentration

n_i – intrinsic carrier concentration

τ_{n0} – electron minority carrier lifetime

τ_{p0} – hole minority carrier lifetime

A – area

R_S – series resistance

Rp – parallel resistance

μ – mobility of charge carriers

v_d – drift velocity

E – electric field

3.7.1 Power conversion efficiency

The power conversion efficiency (PCE) of a solar cell is defined as the amount of incident light intensity that is converted to electric current. It is the ratio of the maximum electrical power to the maximum power of the intensity of the incident photons. Figure 3.6 shows the I V characteristics curve for a typical solar cell. The efficiency is calculated from the relation given below [31-32]:

$$\eta = \frac{P_m}{P_{in}} \times 100\% \qquad (20).$$

$$\eta = \frac{I_m \times V_m}{P_{in}} \times 100\% \qquad (21).$$

where η is power conversion efficiency, P_m is the maximum electric power output of the solar cell, P_{in} is the maximum power of the incident photons, I_m is the maximum output current of the solar cell and V_m is the maximum output voltage of the solar cell.

Fill factor (FF) is an important parameter that determines the efficiency of a solar cell device. It is the ratio of maximum power output to the product of the short circuit current I_{SC} and the open circuit voltage V_{OC}.

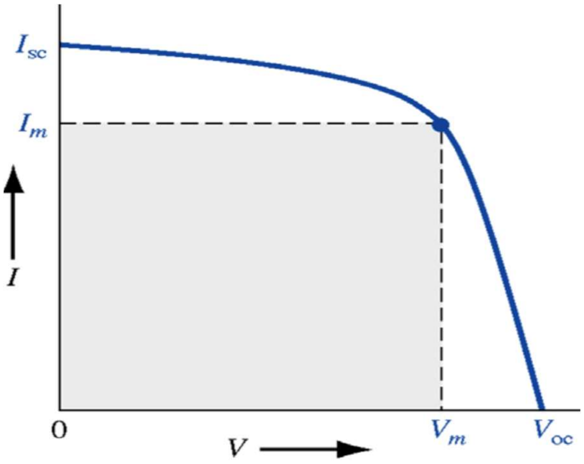

Figure 3.6: Schematic showing IV characteristic of solar cell

$$FF = \frac{I_m \times V_m}{I_{sc} \times V_{oc}} \quad \text{(FF is approximately = 0.7 – 0.8)} \qquad (22).$$

Then the efficiency can be expressed as:

$$\eta = \frac{I_{sc} \times V_{oc} \times FF}{P_{in}} \times 100\% \qquad (23).$$

CHAPTER 4

RESULTS AND CONCLUSION

4.1 Photofabrication of Platinum (Pt) Counter Electrodes

Platinum counter electrodes were photofabricated under different fabrication parameters (conditions) and characterized. Platinic acid precursor solution in EG making 0.02 M were spun coated at 4000 rpm for 30 s at a ramp rate of 500 rpm. 20 ul of the EG solution of H_2PtCl_6 was deposited on an area of 0.25 cm^2 before spinning. Three successive spin coating cycles were conducted to ensure proper adhesion of the Pt precursor solution on the FTO substrates at the chosen spin coating speed. After the spin coating cycles have been completed, scotch tape used for the exposure of the coated area was removed before treatment with UV irradiation at ambient room conditions. On completion of the UV irradiation, the Pt precursor was reduced to Pt on the FTO substrate. The conversion was confirmed by different characterizations reported in this work. To get proper insight into the UV conversion process and attaining optimized parameters for the photofabrication process, effect of irradiation time was studied. The optimized loading amount of the Pt precursor was also investigated by three different spin coating cycles. Finally, we examined the versatility of the photofabrication techniques by using different solvent than EG (in this case ethanol), drop coating method and flexible substrate (PET-ITO was used in this work).

4.1.1 Effect of Irradiation time

To study the effects of irradiation time, samples prepared using three (3) spin coating cycles were treated with different UV irradiation times of 2 h, 1 h and 30 min. The prepared samples with different irradiation times were characterized and used as CEs in fabrication of DSSCs. Figure 4.1 shows the transmittance spectra of the samples at different irradiation times and that of bare FTO glass. The transmittances of all the three samples at different irradiation times are higher than that of bare FTO glass within the visible light spectrum. Figure 4.2 is a photographic images showing the transparency of photofabricated Pt CE (left) in comparison with thermally fabricated Pt CE (right). For an understanding of these recorded enhancement of transmittance in the three samples, the effect of UV irradiation on bare FTO glass was examined. Figure 4.3 shows the transmittance spectra of a precleaned FTO glass that was treated with UV irradiation for different time intervals. The transmittance spectra were measured successively at 30 min, 1 h and 2 h irradiation times. We noticed dependence of transmittance spectra on irradiation time. With this observation, the effect of UV irradiation on the resistivity the FTO sample was investigated by measuring the resistance between two pre-marked points at 15 min, 30 min, 1 h and 2 h UV irradiation time. The resistance of the UV treated FTO was found to improve and has dependency on the irradiation time as shown in Figure 4.4. Meanwhile, transmittance spectra of Figure 4.1 suggest that the UV interaction with the Pt precursor on the FTO glass and subsequent formation of Pt metal equally played part in the enhancement of the transparency of the FTO glass within the visible light region. The sample that underwent 1 h UV irradiation photofabrication showed the highest transmittance across the visible light region of 400 nm to 720 nm.

While those that were treated for 30 min and 2 h respectively had almost same transmittance spectra across same wavelengths.

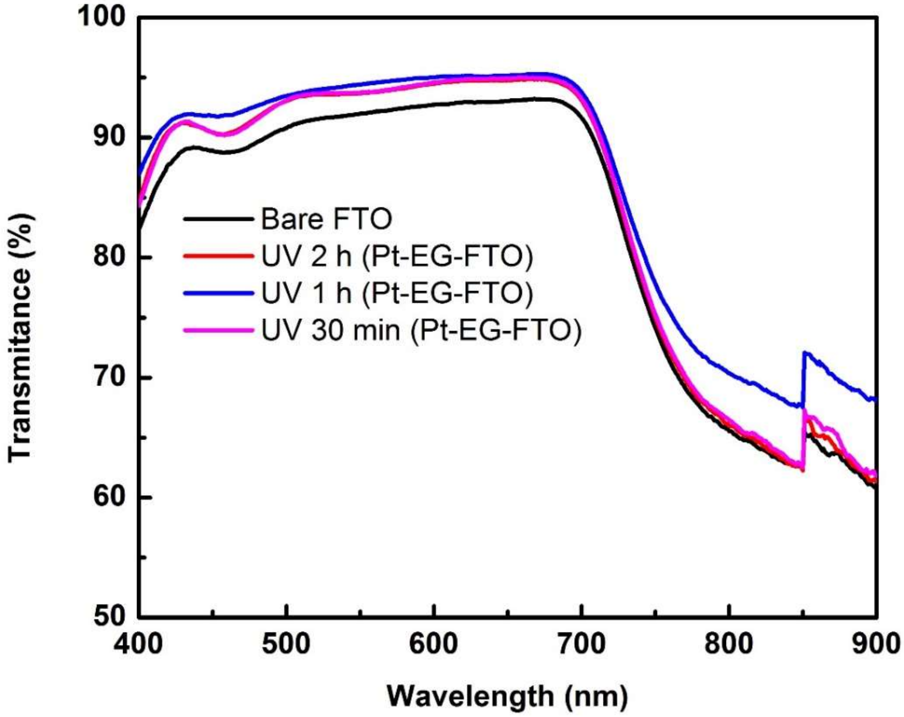

Figure 4.1: Transmittance of photofabricated Pt CEs at different irradiation time

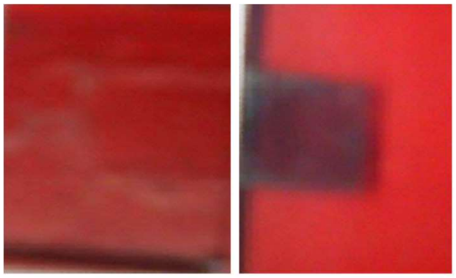

Figure 4.2: Photgraphic images comparing the transparency of typical photofabricated Pt CE (left) and thermally fabricated Pt CE @ 450 ºC (right)

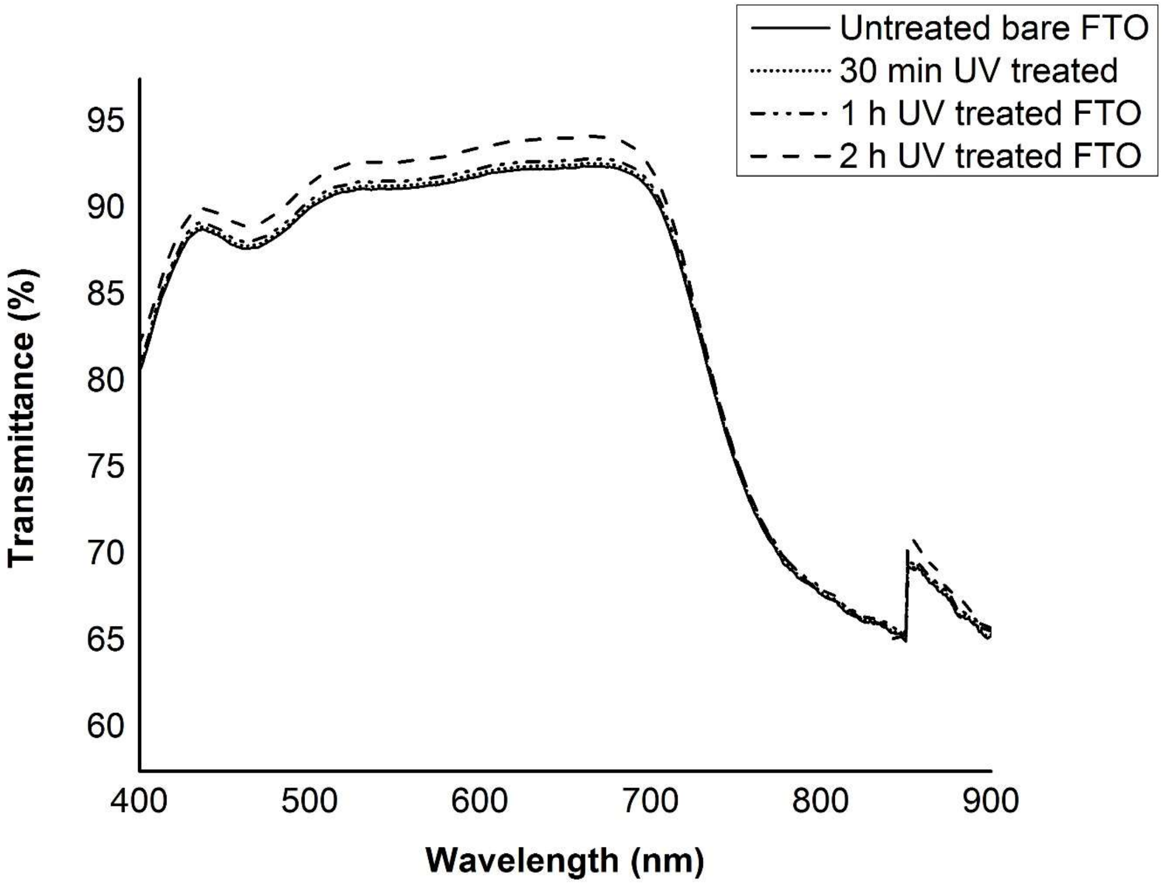

Figure 4.3: Transmittance spectra of UV treated bare FTO at different irradiation time

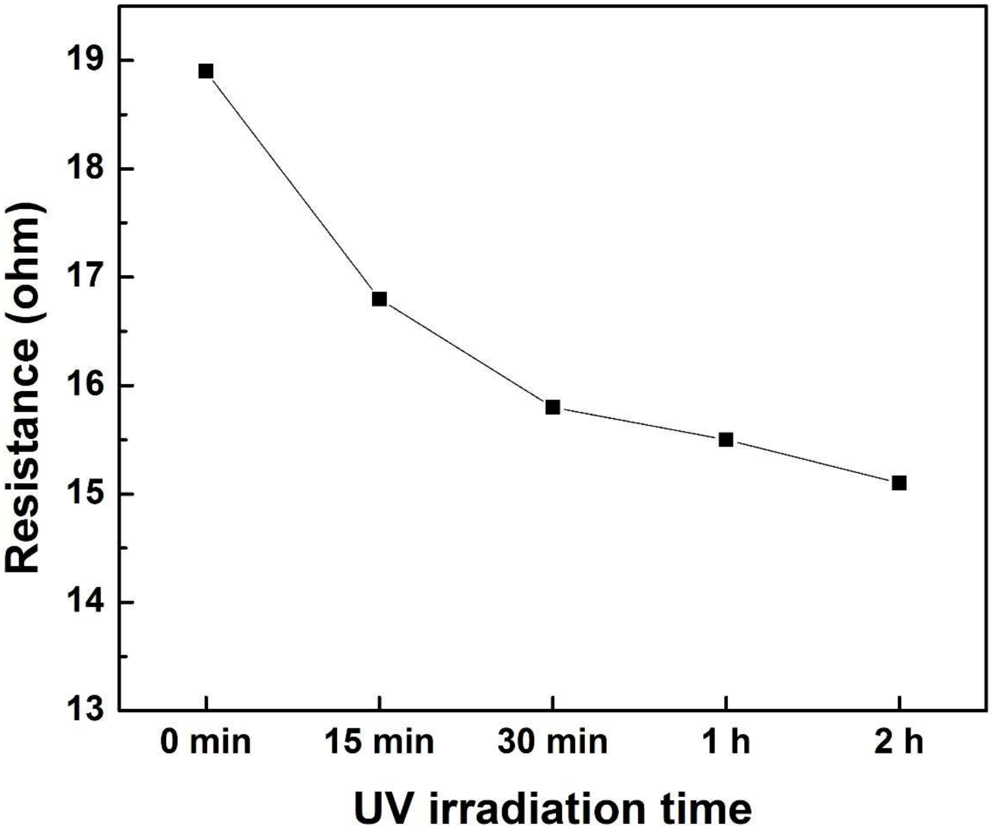

Figure 4.4: Showing effect of UV irradiation on bare FTO resistance at different irradiation time

The photoreduction of the $H_2PtCl_6.6H_2O$ in EG to Pt metal for the photofabricated CEs was investigated by XPS. The XPS spectra of the three samples with different UV irradiation time were compared to understand the effect of UV irradiation time on the photoreduction process. Figure 4.5 shows the XPS spectra of the three different samples with 3 cycles of spin coating and UV irradiated for 30 min, 1 h and 2 h respectively. All three samples exhibit platinum peak at Pt 4f orbital. Small Chlorine peak at Cl 2p orbital is observed to reduce with increase in UV irradiation time. At 1 h UV irradiation time the Cl 2p peak can be seen to have reduced compare to UV irradiation time of 30 min. While the peak is absent at 2 h UV irradiation time. Figure 4.6 compares the platinum peaks of the three samples at the respective UV irradiation time. The Pt peak at 2 h is seen to be lower compare with that of UV irradiation time of 30 min and 1 h. This might be due to degradation of the Platinum coating on the FTO. Hence, optimized UV irradiation time for the photofabrication process is important.

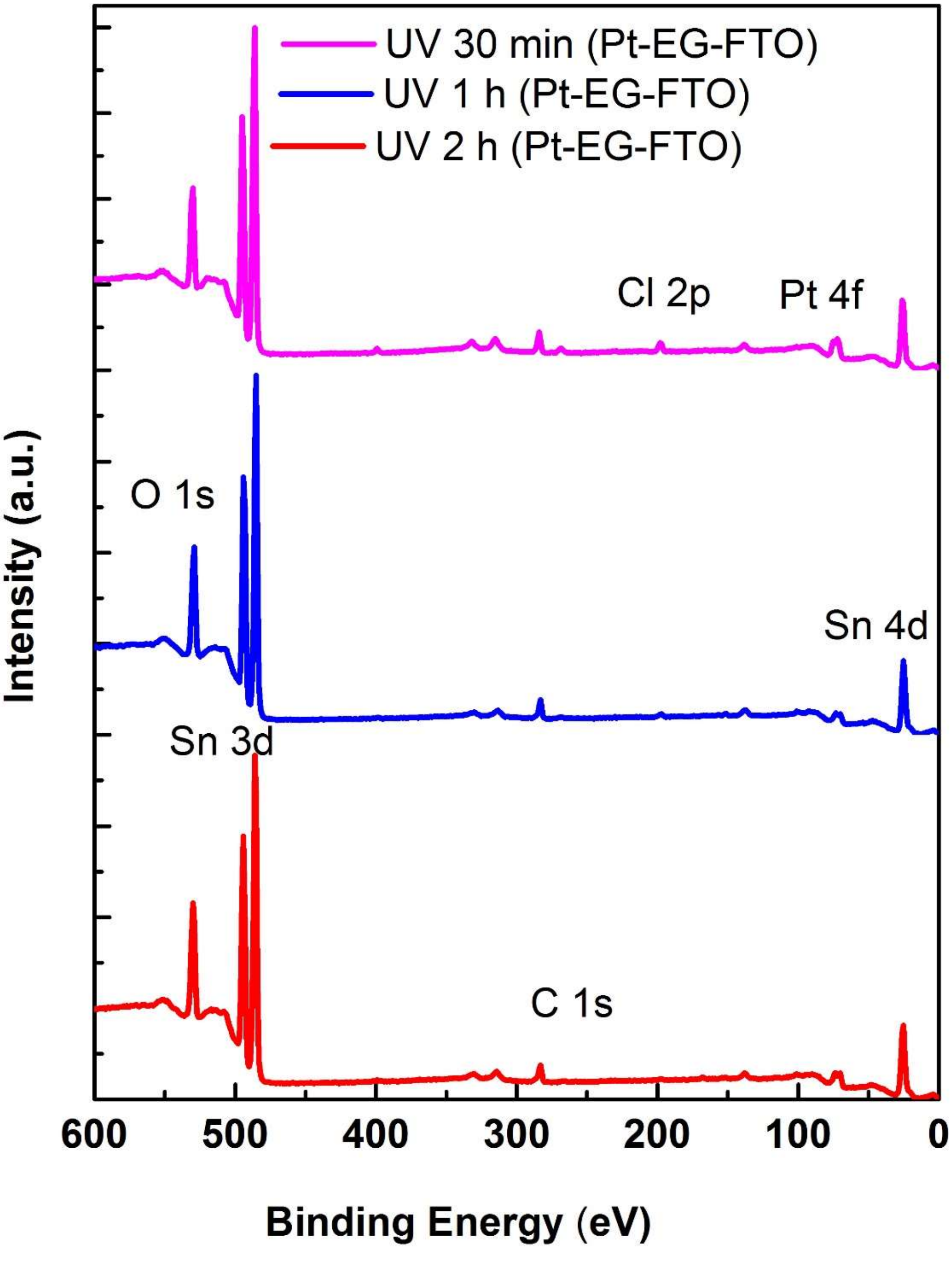

Figure 4.5: XPS survey spectra of (Pt-EG-FTO) at different irradiation time

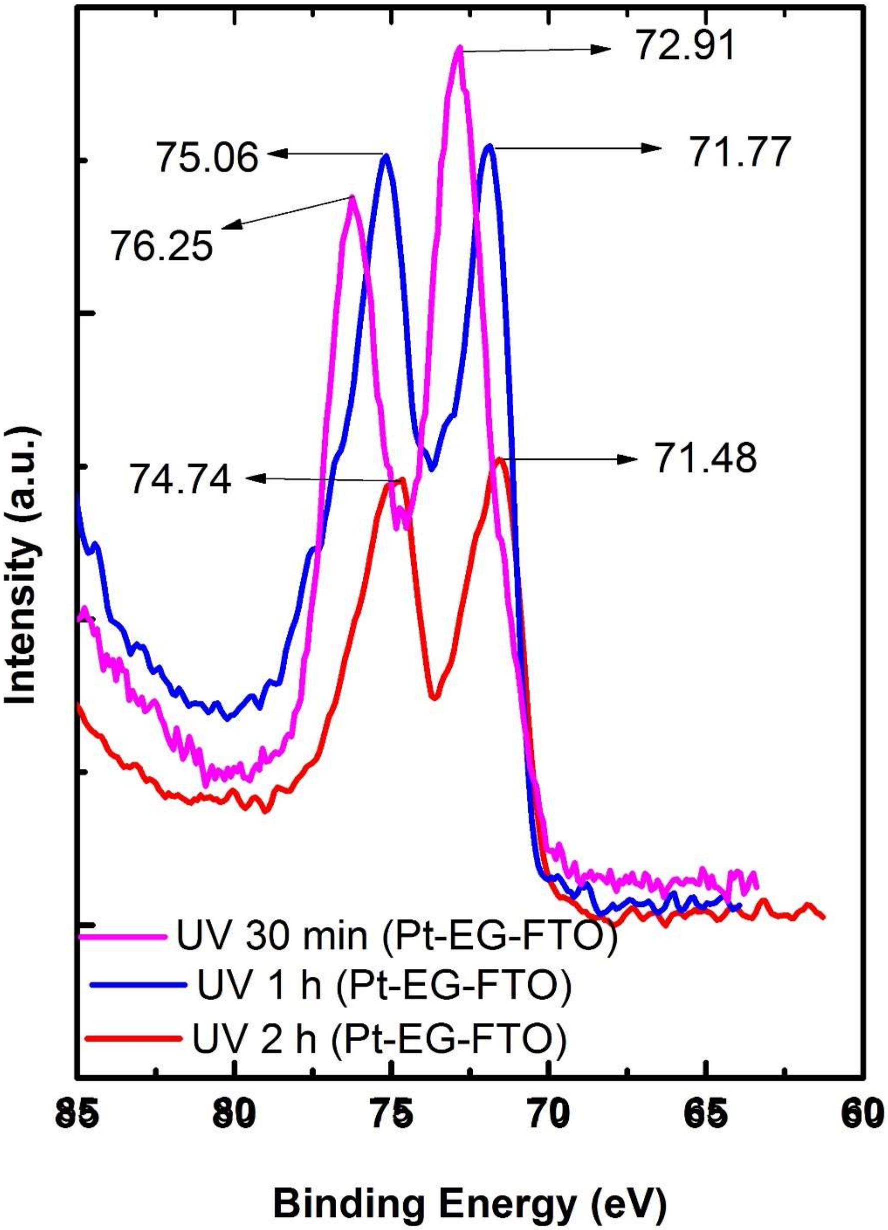

Figure 4.6: XPS spectra of Pt metal of the photofabricated Pt CE (Pt-EG-FTO) at different irradiation time

The SEM images shown in Figure 4.7 (a-c) for the three photofabricated Pt CEs with different UV irradiation time of 2 h, 1 h and 30 min indicate that Pt nanoparticles are well dispersed on the FTOs and no agglomerated site can be seen on the morphology of the photofabricated Pt CEs.

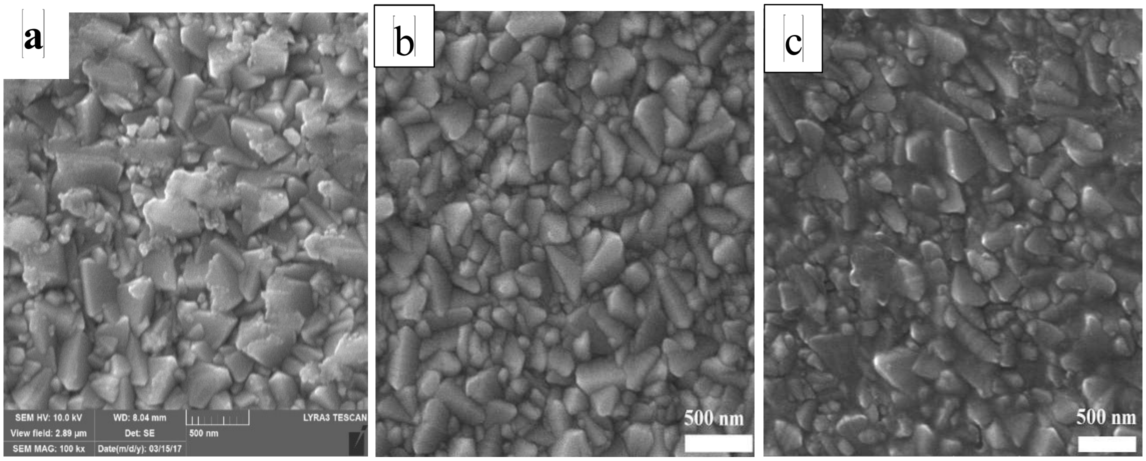

Figure 4.7: SEM images of photofabricated Pt CEs (Pt-EG-FTO) a) 2 h irradiation time b) 1 h irradiation time c) 30 min irradiation time

Electrochemical Characterization

The electrochemical characterization of the samples were carried out in order to study the catalytic activity of the samples in triiodide/iodide electrolyte. Figure 4.8 shows the cyclic voltammetry (CV) analysis of the samples. The bare FTO sample shows no catalytic activity as no reduction or oxidation is present in the CV scan of the sample. UV irradiated samples with 1 h and 2 h show both reduction and oxidation peaks that are aligned throughout the CV scan while sample with 30 min UV irradiation time exhibit a slight shift from them. CV measurement is particularly useful in understand the regeneration of dye molecules from the triiodide/iodide electrolyte after the photoreduction of the dye molecule in generation of electron into the TiO_2 photoanode material, as equilibrium is desired for the continuous functioning of the solar cells. The redox reaction at the electrolyte/photofabricated Pt CE interface is as given below:

$I_3^- + 2e^- \longrightarrow 3I^-$

$3I^- \longrightarrow I_3^- + 2e^-$ 24

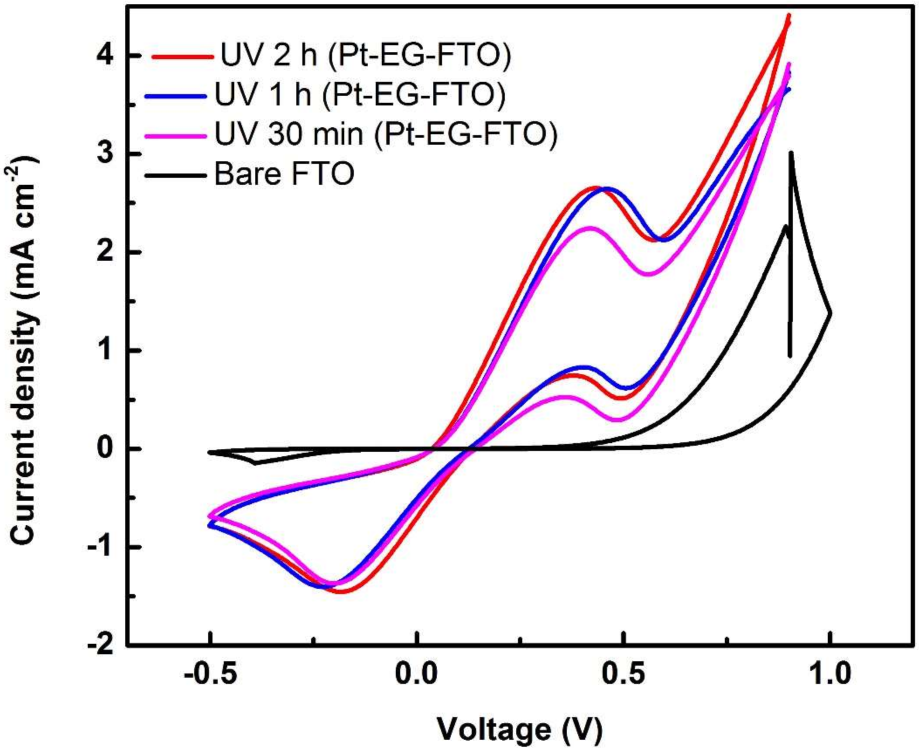

Figure 4.8: CV scan measurement of photofabricated Pt CEs (Pt-EG-FTO) at different irradiation time

The Nyquist impedance plot shown in Figure 4.9 illustrate the charge transfer mechanism between the electrolyte and photofabricated Pt CEs in symmetric dummy cells. The fitting of the Nyquist plots are carried out within the NOVA 2.1 environment. The equivalent circuit used in fitting the Nyquist plot is as shown in Figure 4.10. The series resistance R_S, charge transfer resistance R_{CT} and constant phase element (CPE) of the dummy cells are summarized in Table 4.1. The sample with 1 h UV irradiation exhibits the least series resistance and charge transfer resistance. 2 h UV irradiated sample also performed better than 30 min UV irradiated sample.

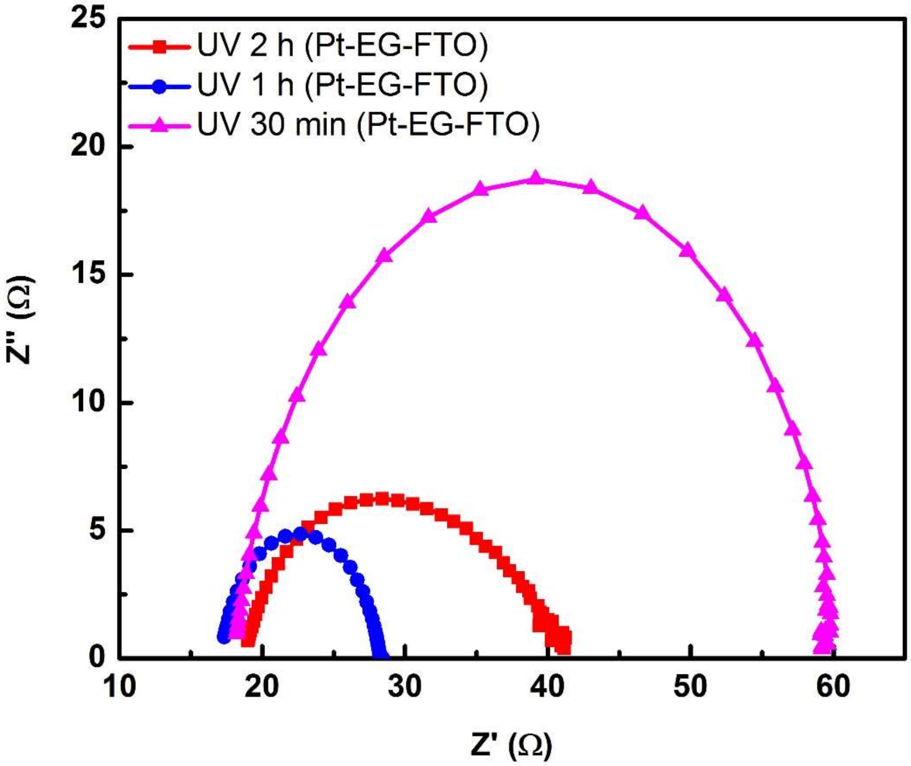

Figure 4.9: Nyquist plots of photofabricated Pt CEs (Pt-EG-FTO) at different irradiation time

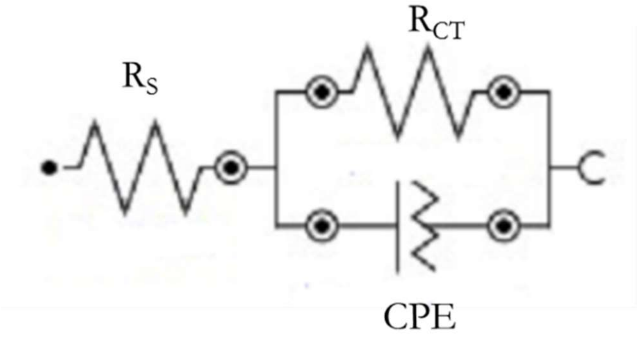

Figure 4.10: Equivalent circuit used for the fitting of Nyquist curve of photofabricated Pt CEs.

Table 4.1: Nyquist fit parameters of photofabricated Pt CEs

Photofabricated Pt-CEs	**R_S (Ω)**	**R_{CT} (Ω)**	**CPE (μF)**	**J_0 (mA cm^{-2})**
UV 2 h (Pt-EG-FTO)	18.21	22.697	11.91	0.57
UV 1 h (Pt-EG-FTO)	17.64	10.639	7.09	1.20
UV 30 min (Pt-EG-FTO)	18.17	40.788	5.69	0.32
4 cycle UV 1 h (Pt-EG-FTO)	29.86	31.858	7.71	
5 cycle UV 1 h (Pt-EG-FTO)	33.595	48.70	9.67	
UV 1 h (Pt-EtOH-FTO)	30.36	24.098	10.38	0.53
UV 30 min (Pt-EtOH-FTO)	37.65	143.53	9.20	0.09
UV 15 min (Pt-EtOH-FTO)	22.17	241.04	5.58	0.05
UV 1 h (Pt-EtOH-PET-ITO)	366.10	1655.30	0.39	0.008

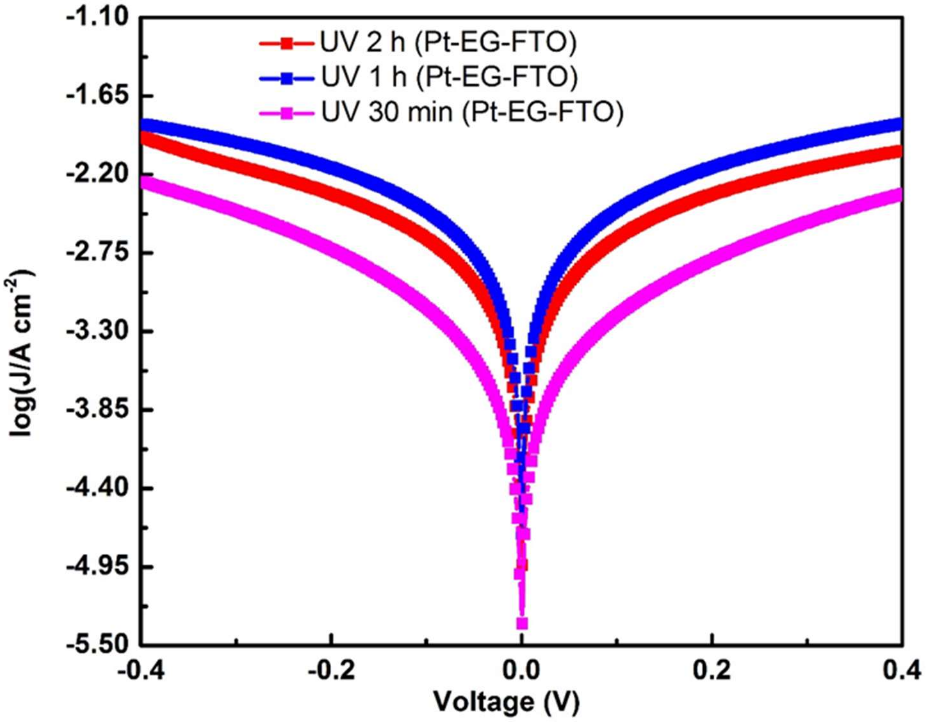

Figure 4.11: Tafel polarization plots of photofabrciated Pt CEs at different UV irradiation times

Figure 4.11 shows the Tafel polarization of the photofabricated Pt CEs exhibiting both anodic and cathodic branches. Pt CE with 1 h UV irradiation time shows the highest logarithmic current density value followed by that with 2 h UV irradiation and then that with 30 min UV irradiation time. The results obtained from the Tafel plot further confirmed the results discussed above.

From the transmittance, XPS and electrochemical characterizations results discussed above, we could conclude that 30 min irradiation was not sufficient to reduce the Pt precursor to Pt metal. While excessive UV exposure appears to be detrimental to the photofabrication process as is the case for the 2 h UV irradiated sample. Hence, 1 h irradiation time seems the optimal value for the UV photofabrication Pt CE technique.

4.1.2 Effects of spin coating cycles

To further our investigations, effects of spin coating cycles of the EG solution of $H_2PCl_6.6H_2O$ were examined. Here we restricted our study to 4 cycles and 5 cycles of spin coating as minimal Pt loading is an essential consideration for the practical utilization of our photofabrication technique. After the completion of the spin coating cycles, the samples were exposed to UV irradiation for 1 h. Figure 4.12 is the transmittance spectra of 3, 4 and 5 spin coating cycles samples, UV treated for 1 h. Transmittance spectra of all samples in this case are also greater than that of bare FTO glass. Further confirming the enhancement of the bare FTO glass transparency. We equally noted that 3 cycles spin coated sample transmittance is higher than 4 cycles and 5 cycles spin coated samples respectively, between the wavelength of 400 nm and 640 nm. While 3 cycles and 4 cycles spin coated samples almost overlap each other between spectra wavelength of 640 nm and 720 nm. The lower transmittance spectrum of 5 cycles spin coated sample as compared to 3 cycles and 4 cycles spin coated samples might be due to increase in the Pt metal thickness on the FTO glass and thereby resulting in loss of transmittance.

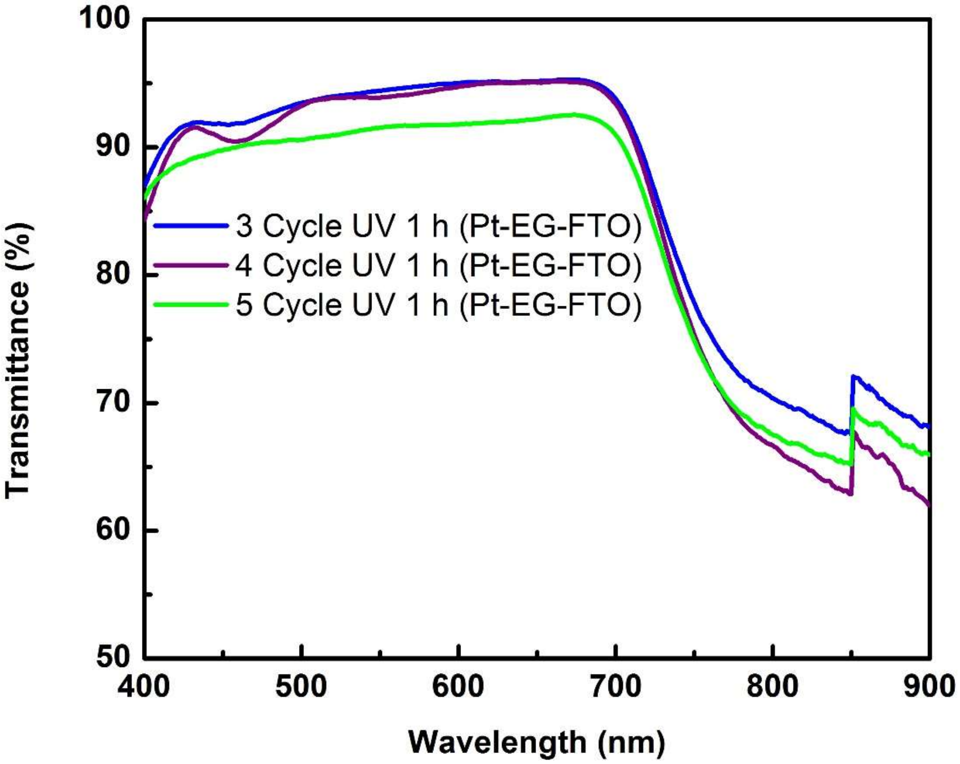

Figure 4.12: Transmittance of photofabricated Pt CEs UV irradiated for 1 h for different spin coating cycles

Figure 4.13 compares the XPS spectra of the three different spin coating cycles samples. The XPS spectra are consistent for samples UV irradiated for 1 h. The platinum peaks for these samples are compared in Figure 4.14. The Platinum peaks for 4 cycles and 5 cycles spin coated samples are formed at same binding energies with the Pt $4f_{7/2}$ orbital peak of 5 cycles spin coated sample slightly higher than that for 3 cycles spin coated sample. In contrast, 4 cycles spin coated sample exhibits platinum peaks slightly away from the binding energies of 3 cycles and 5 cycles spin coated samples. Also, the platinum peaks are much lower compare to the two other samples. This might be due to experimental fabrication error of the Pt CE using 4 spin coating cycles.

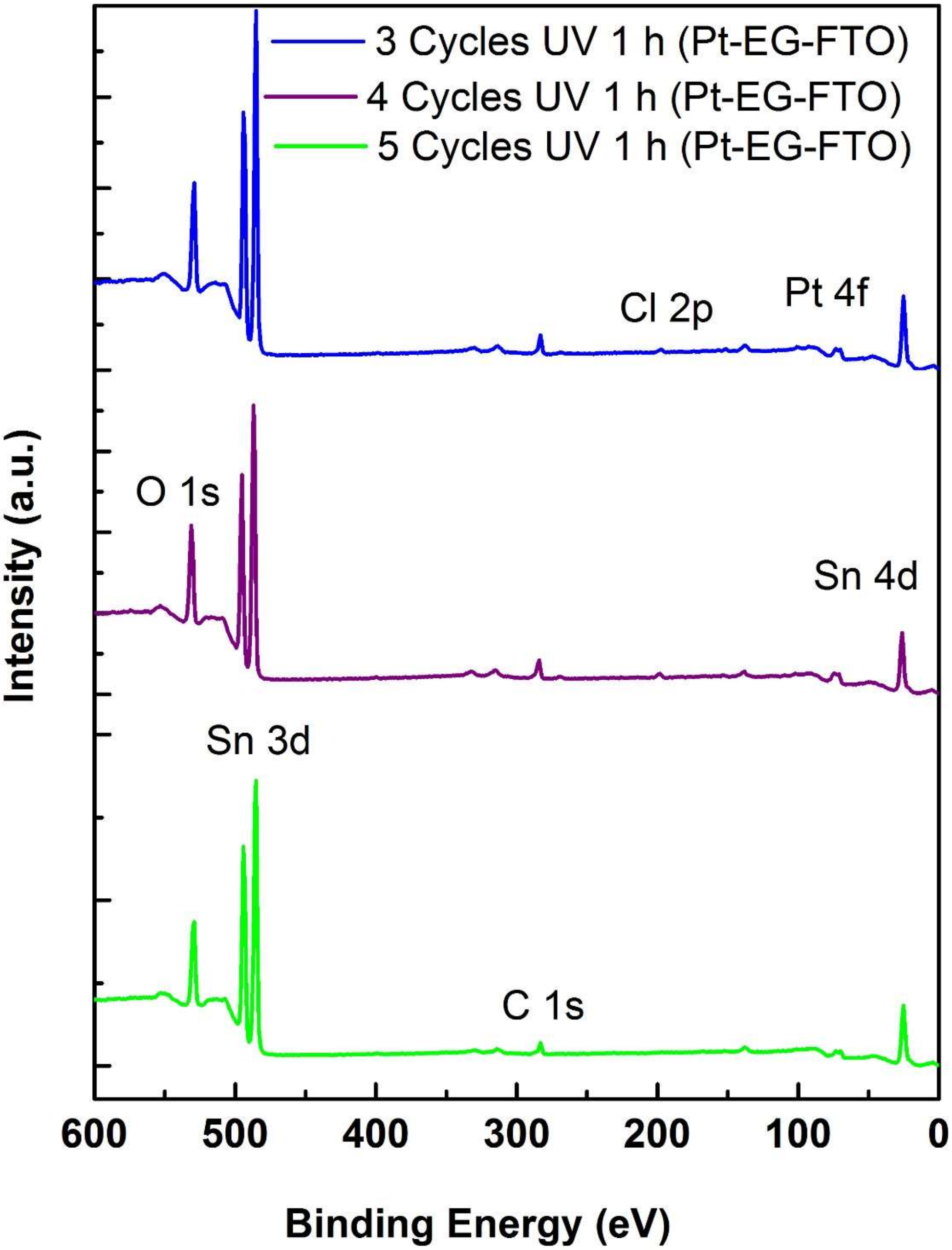

Figure 4.13: XPS survey spectra of Pt CEs (Pt-EG-FTO) with 1 h UV irradiation time for different spin coating circles

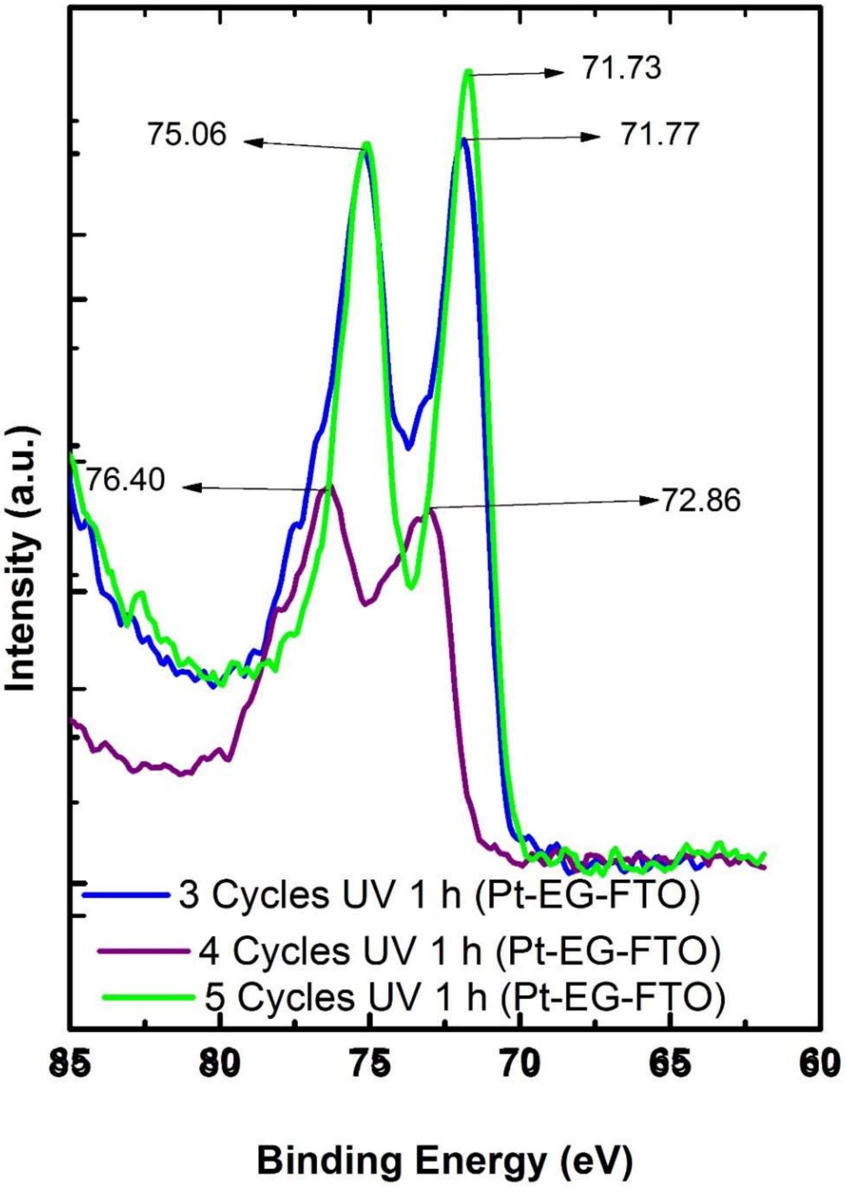

Figure 4.14: XPS spectra of Pt CEs (Pt-EG-FTO) with 1 h UV irradiation time for different spin coating cycles a) survey spectra of the photofabricated Pt CEs b) Pt spectra of the photofabricated Pt CEs

Figure 4.15 is the SEM images comparing of the 3 cycles, 4 cycles and 5 cycles spin coated samples. They exhibit much platinum distribution on the FTO owing to increased spin coating cycles.

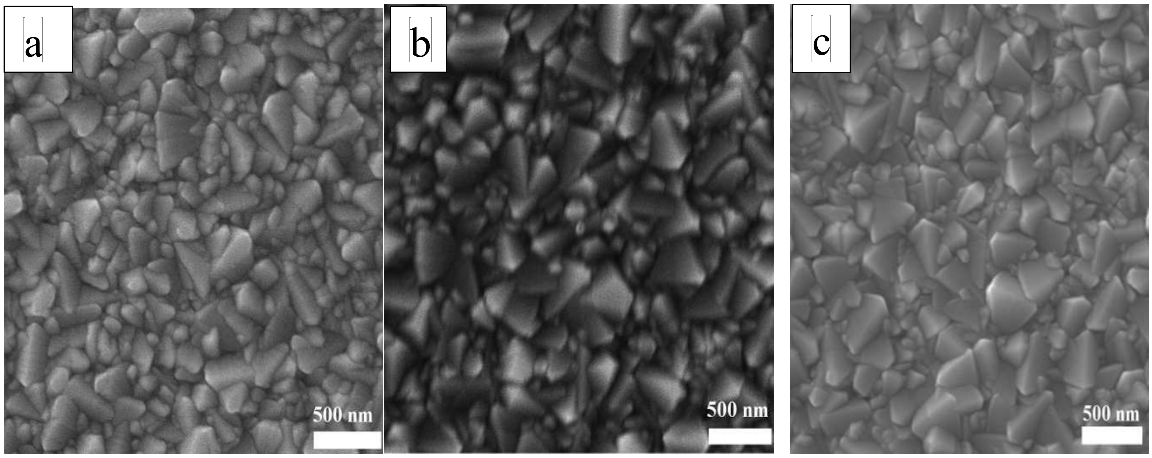

Figure 4.15: SEM images of photofabricated Pt CEs (Pt-EG-FTO) with 1 h UV irradiation time a) 4 spin coating cycles b) 5 spin coating cycles

Electrochemical Characterization

The CV scan of the 3 and 5 cycles samples are seen to overlap more than that of 4 cycle sample as displayed in Figure 4.16. This trend was also observed in the XPS analysis. All the samples at different spin coating cycles exhibits both reduction and oxidation peaks in the CV scan measurement.

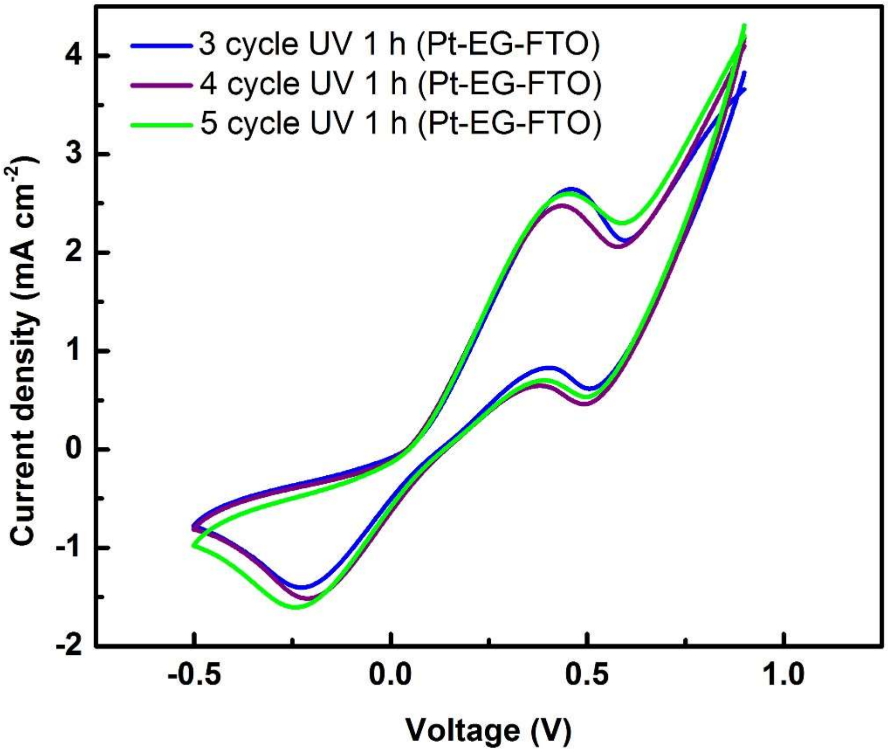

Figure 4.16: CV scan measurement of photofabricated Pt CEs (pt-EG-FTO) with 1 h UV irradiation time and different spin coating cycles

Figure 4.17 shows the Nyquist plots of the 4 and 5 spin coating cycles photofabricated Pt CEs. The Nyquist plot parameters of the 3, 4 and 5 cycles spin coating are listed in Table 1 From the comparison of the different cycles photofabricated electrodes, 3 spin coating cycles with 1 h UV irradiation outperformed all other samples from the result of the different characterization conducted. Higher logarithmic current density was recorded for Pt CE with 3 spin coating cycles compared with the values of the 4 and 5 spin coating cycles as ssown in Tafel plot of Figure 4.18. Particularly the result of the XPS, CV and EIS measurements. Despite the fact that 4 and 5 cycles spin coated samples are expected to have more Pt loading, their performances are less compare to the 3-cycle spin coated sample. This may be due to solvent event as EG may require more UV irradiation time to be totally removed from the photofabricated Pt CEs

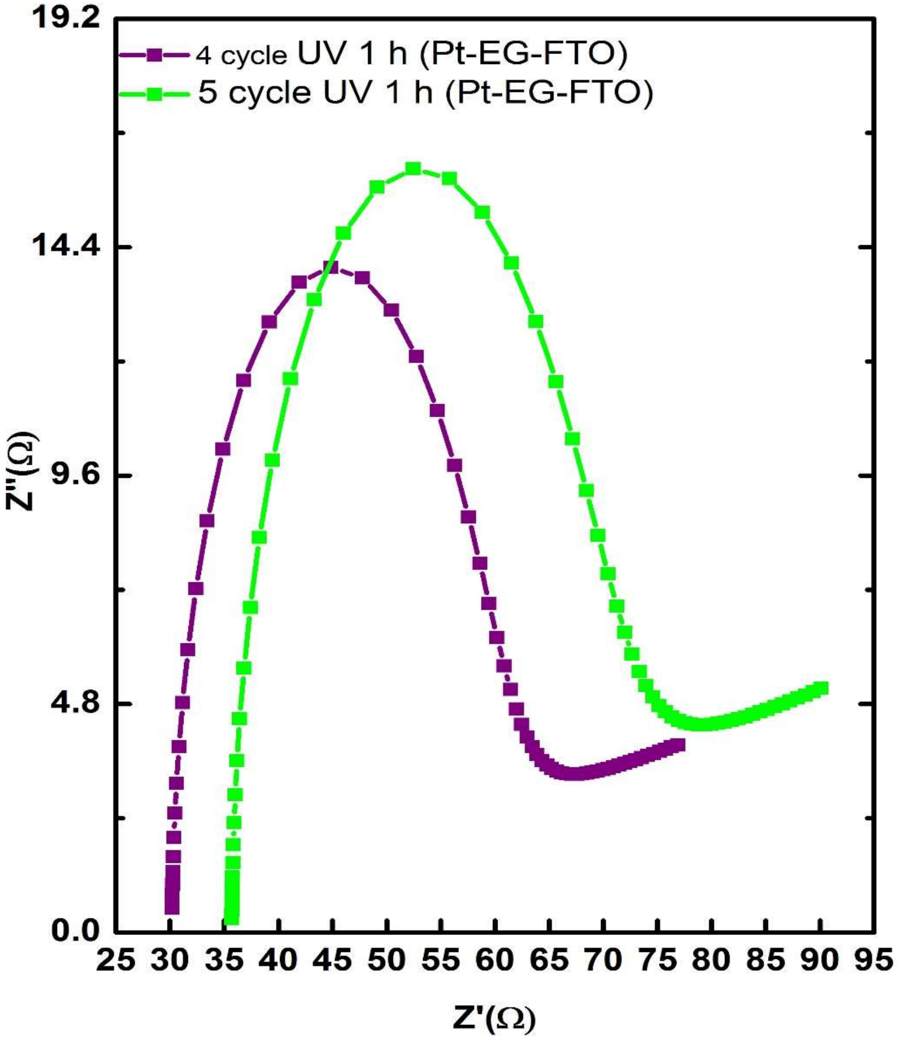

Figure 4.17: Nyquist plots of photofabricated Pt CEs (Pt-EG-FTO) with 1 h UV irradiation time and different spin coating cycles

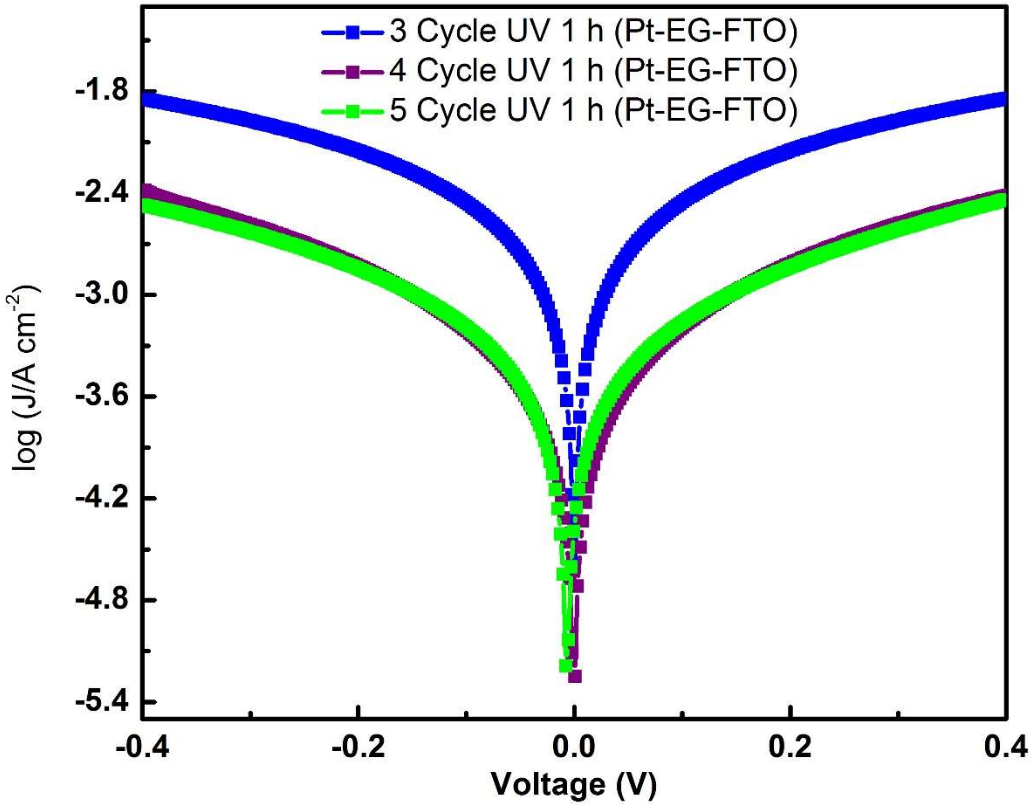

Figure 4.18: Tafel polarization plots of photofabricated Pt CEs at different spin coating cycles with 1 h UV irradiation

4.1.3 Effects of solvents

The versatility of our photofabrication technique with respect to different solvents is reported. Here, we chose ethanol as a representative solvent of other suitable solvents that are used in the synthesis of Pt metal from $H_2PtCl_6.6H_2O$ precursor. Ethanol has an advantage of low boiling point of 78 ºC over EG, it can therefore evaporate easily compare to EG. Owing to this advantage, drop casting method was used in depositing the platinic acid in ethanol precursor for the photofabrication process. The drop casting method utilized much lower platinic acid solution, leading to minimal Pt loading as compared to spin coating process that results in wastage of material. For the drop casting process, 30 ul of 0.02 M ethanol solution of $H_2PtCl_6.6H_2O$ was dropped on an exposed area of 0.25 cm^2 of FTO glass. Three samples were prepared using this approach and UV irradiated for 1 h, 30 min and 15 min, respectively. Figure 4.19 shows the transmittance spectra of the photofabricated Pt CEs from the ethanolic platinic acid solution. All the transmission spectra of the three samples are greater than the transmittance spectrum of bare FTO across the visible light wavelength region.

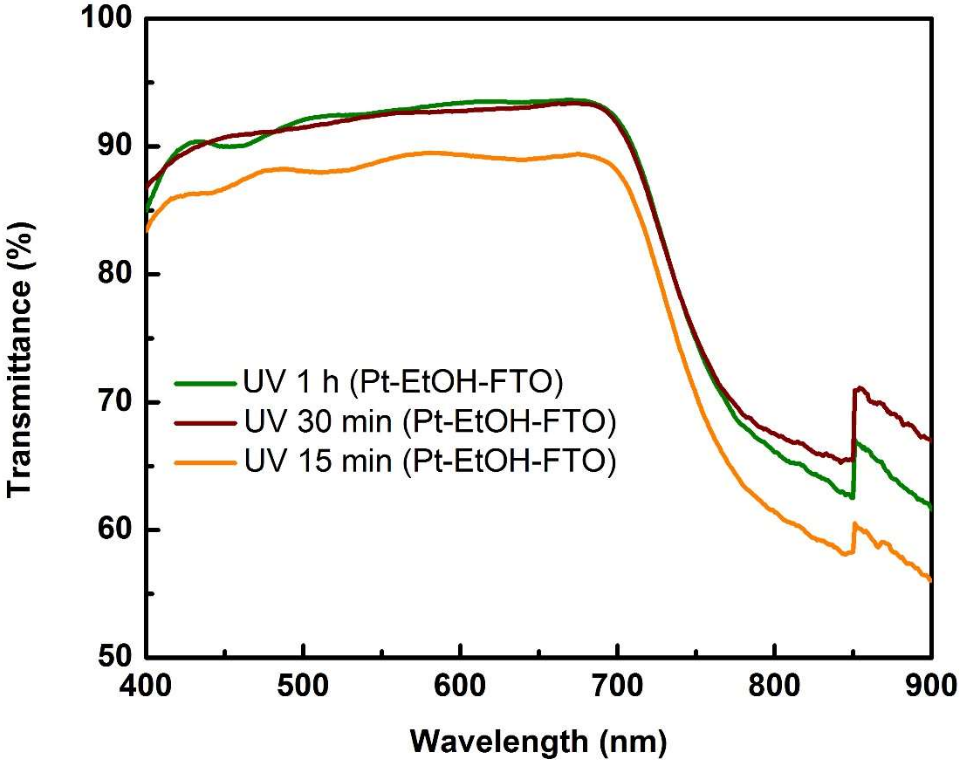

Figure 4.19: Transmittance spectra of Pt CEs (Pt-EtOH-FTO) with different irradiation time

Figure 4.20 is the XPS spectra of the photofabricated Pt CEs from ethanol based platinic acid solution. All three samples at different UV irradiation time show much prominent platinum peaks than platinum peaks of all samples photofabricated from EG platinic acid solution. This indicates that there are better and more efficient platinum loading for drop coated precursor samples than there are for the spin coated samples. The effect of UV irradiation time can as well be seen from the XPS spectra. As UV irradiation time increases from 15 min to 1 h, the platinum peaks can be seen to increase with respect to the irradiation time (Figure 4.21). Meanwhile, the Chlorine peaks decrease with increase in UV irradiation time, confirming the photoreduction of the $H_2PtCl_6.6H_2O$ in ethanol to Pt.

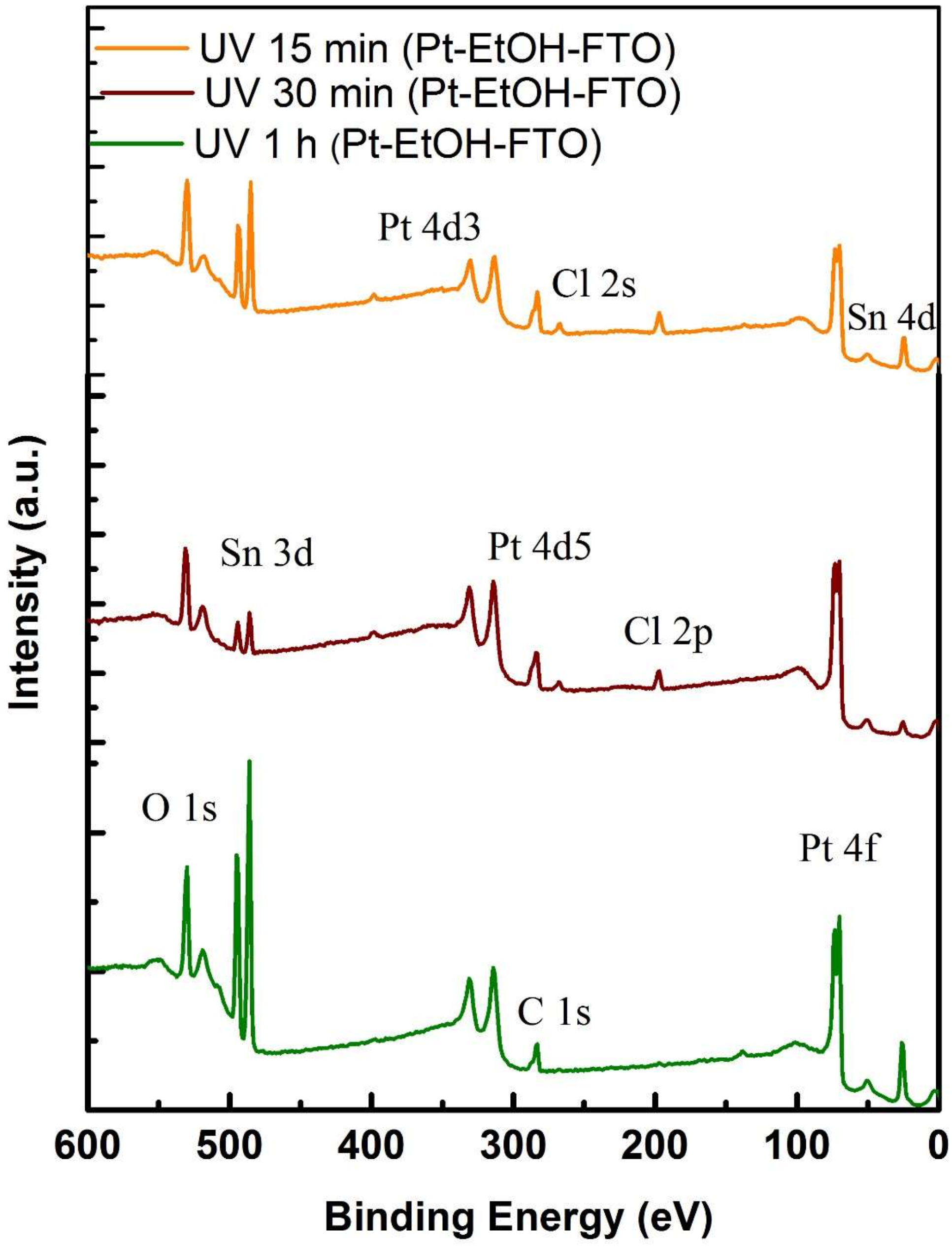

Figure 4.20: XPS survey spectra of photofabricated Pt CEs (Pt-EtOH-FTO) with different UV irradiation time

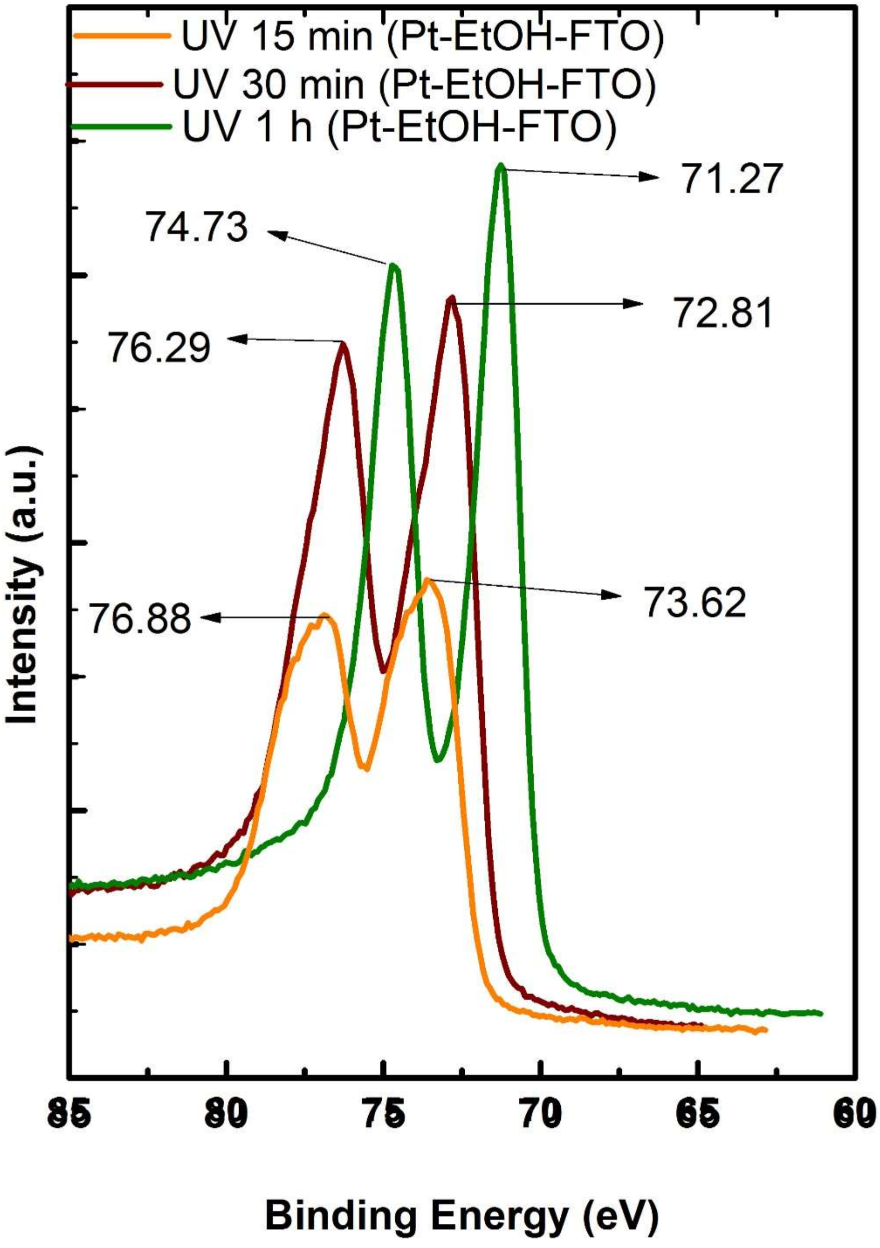

Figure 4.21: XPS spectra comparing Pt peaks of photofabricated Pt CEs (Pt-EtOH-FTO) with different irradiation time

The SEM images of UV irradiated samples at different irradiation time are presented in Figure 4.22. Figure 4.22a and 4.22b show well dispersed and high platinum loading on the FTOs. However, Figure 4.22c indicates that the ethanolic platinic acid solution has only been partially photoreduced, with its SEM image not properly defined, as sheet and cloud-like structures could be seen in the image.

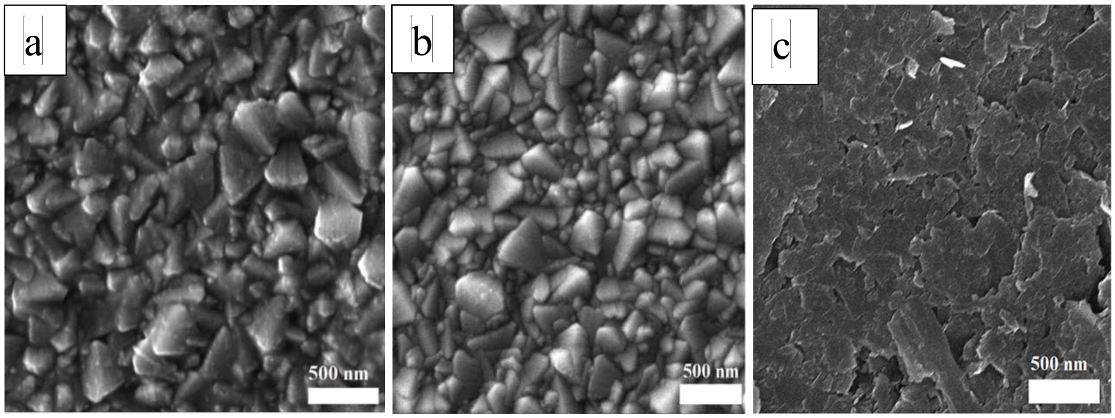

Figure 4.22: SEM images of photofabricated Pt CEs (Pt-EtOH-FTO) a) 1 h UV irradiation time b) 30 min UV irradiation time c) 15 mins UV irradiation time

Electrochemical Characterization

The CV scan measurement of the photoreduced ethanolic platinic acid based Pt CEs are presented in Figure 4.23. Consistent with the XPS spectra and SEM images, 15 min UV irradiated sample showed poor catalytic activity as it exhibits little reduction and oxidation peaks in the CV scan measurement. On the other hand, 1 h UV irradiated sample showed a more prominent reduction and oxidation peaks, making it exhibits very good catalytic activity. Pt CE photofabricated with 30 min UV irradiation equally manifest good catalytic activity.

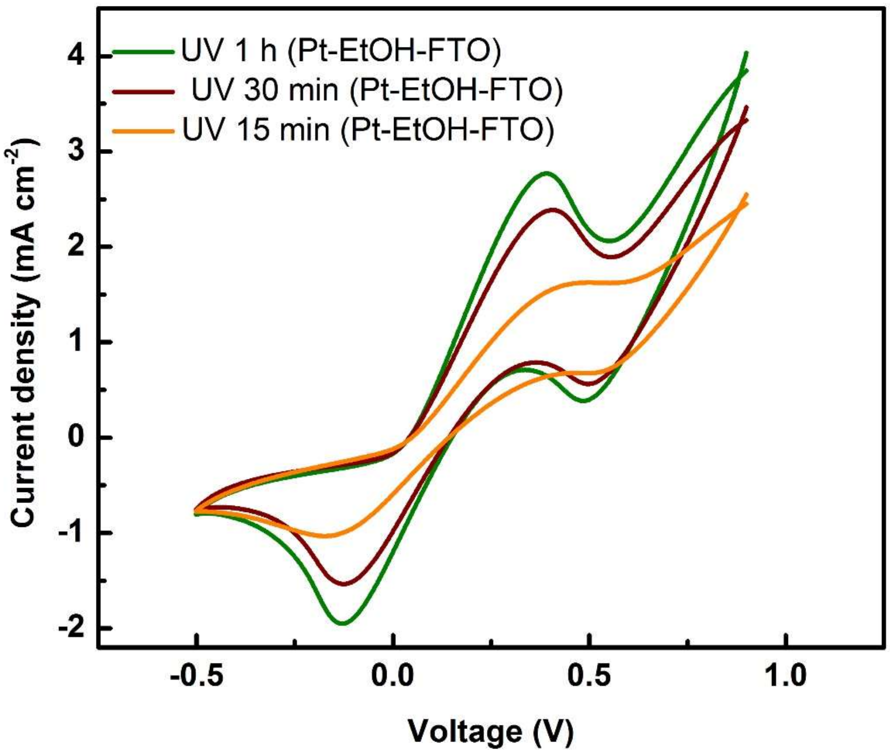

Figure 4.23: CV scan measurement of photofabricated Pt CEs (Pt-EtOH-FTO) with different UV irradiation time

The Nyquist plot parameters of all ethanolic based photofabricated Pt CEs are presented in Table 4.1. Owing to the good Pt loading and high catalytic activity UV 1 h (Pt-EtOH-FTO) has a small series resistance and small charge transfer resistance. The Nyquist plot further confirmed the insufficiency of 15 irradiation time for the photofabrication process. The series and charge transfer resistances are to be higher than all photofabricated Pt CEs. Figure 4.24 shows the Nyquist plots of the Pt-EtOH-FTO photofabrciated Pt CEs with different UV irradiation time. Figure 4.25 is the Tafel plot of the (Pt-EtOH-FTO) Pt CEs. Pt-EtOH-FTO UV 1 h exhibits the highest logarithmic current density.

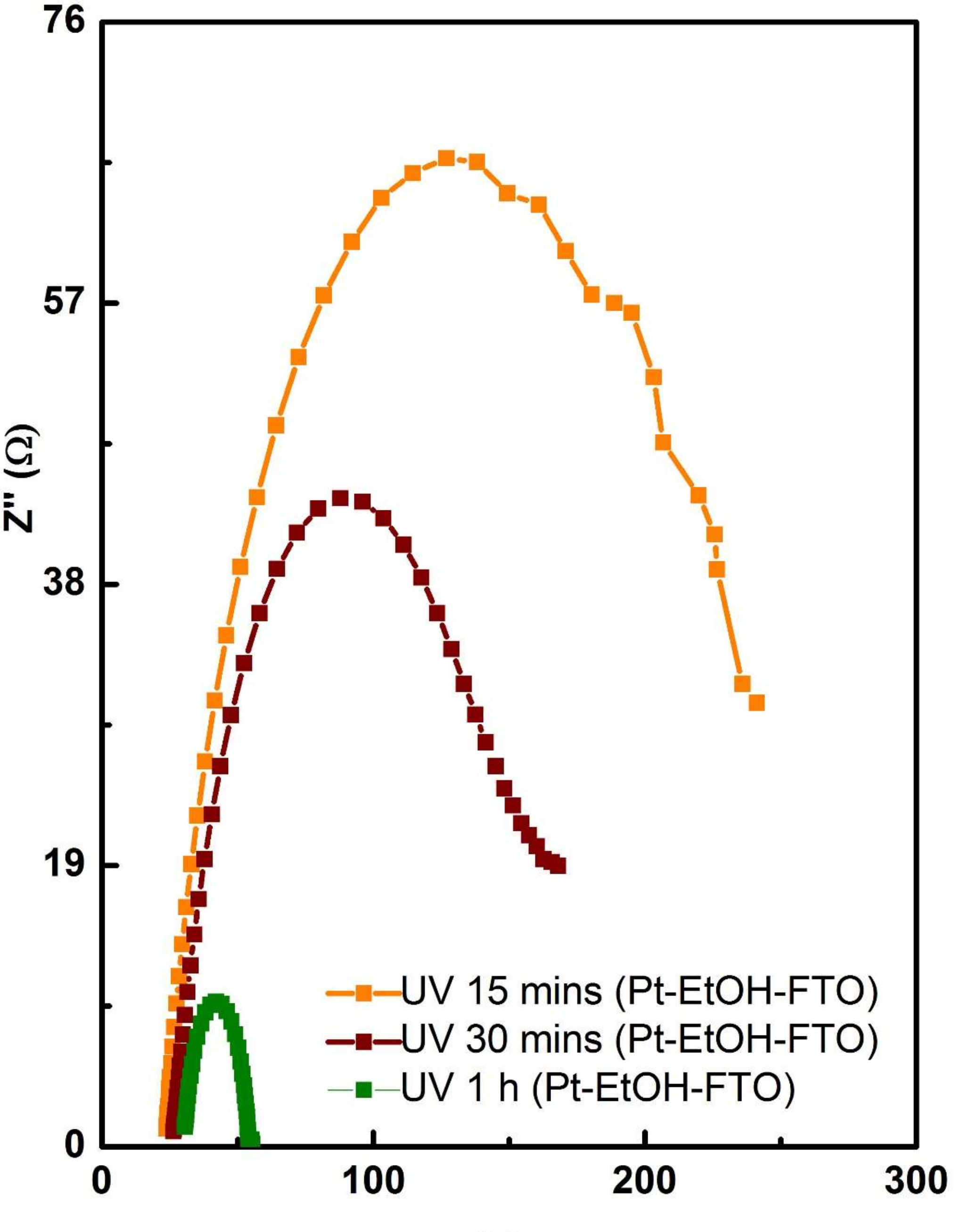

Figure 4.24: Nyquist plots of photofabricated Pt CEs (Pt-EtOH-FTO) with different UV irradiation time

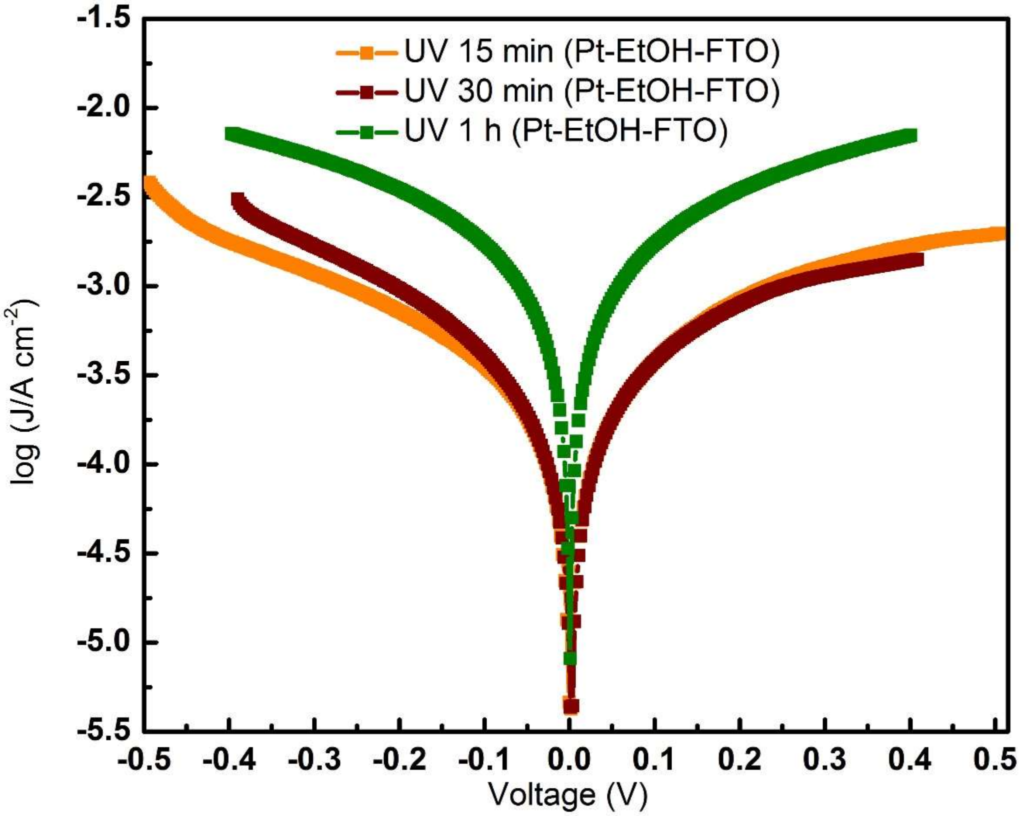

Figure 4.25: Tafel polarization plots of Pt-EtOH-FTO Pt CEs at different UV irradiation times

4.1.4 Photofabrication of Pt on PET-ITO

Flexible Pt CE on PET-ITO (Pt-EtOH-ITO-PET) was photofabricated as a demonstration of the versatility and potential area of application of the photofabrication technique. 5 ul ethanolic platinic acid precursor was drop casted on an exposed area of 0.25 cm^2 of PET-ITO substrate and then treated with 1 h UV irradiation time. The ambient temperature of not more than 40 ^{o}C of the UV irradiation intensity particularly make it suitable for use on flexible substrates. Figure 4.26 is the transmittance spectra of the photofabricated Pt flexible CE. The obtained spectra show improvement of the transparency of the photofabrciated Pt flexible CE as compared to bare PET-ITO substrate. This is consistent with the transmittance results obtained for photofabricated Pt CEs on FTO substrates. Figure 4.27 shows the SEM morphology image of the Pt flexible CE with well dispersed Pt seen in the image and some agglomeration sites can as well be seen in the image. The catalytic activities of photofabricated Pt flexible CE were investigated by CV scan, EIS Nyquist measurement and Tafel plot. Figure 4.28 and Figure 4.29 show the CV scan measurement and Nyquist plot of the photofabricated Pt flexible CE. The Tafel is as shown in Figure 4.30.

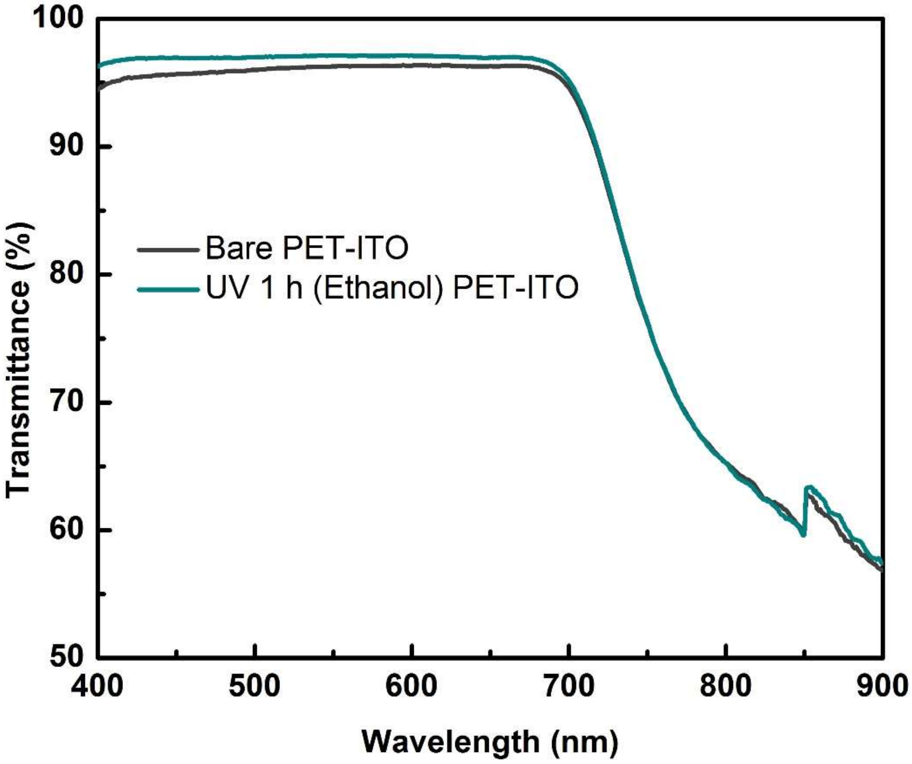

Figure 4.26: Transmittance spectra photofabricated Pt CE (Pt-EtOH-ITO-PET) with 1 h UV irradiation time

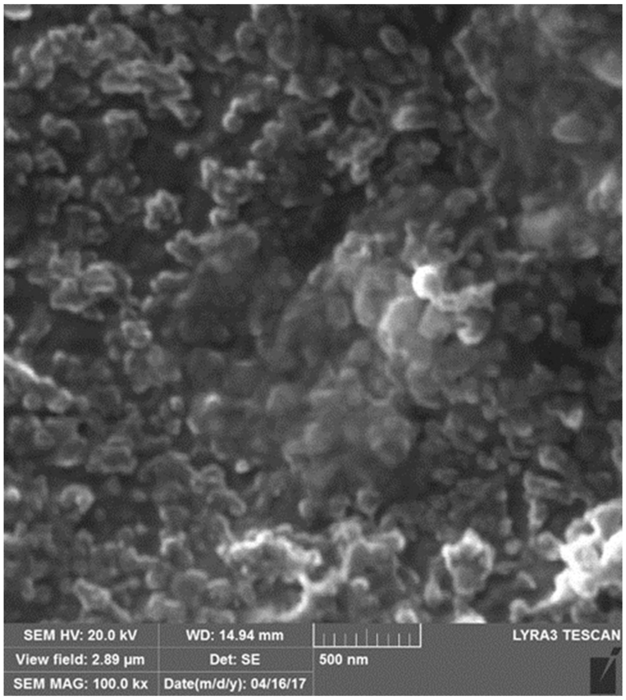

Figure 4.27: SEM image of photofabricated Pt CE (Pt-EtOH-ITO-PET) with 1 h UV irradiation time

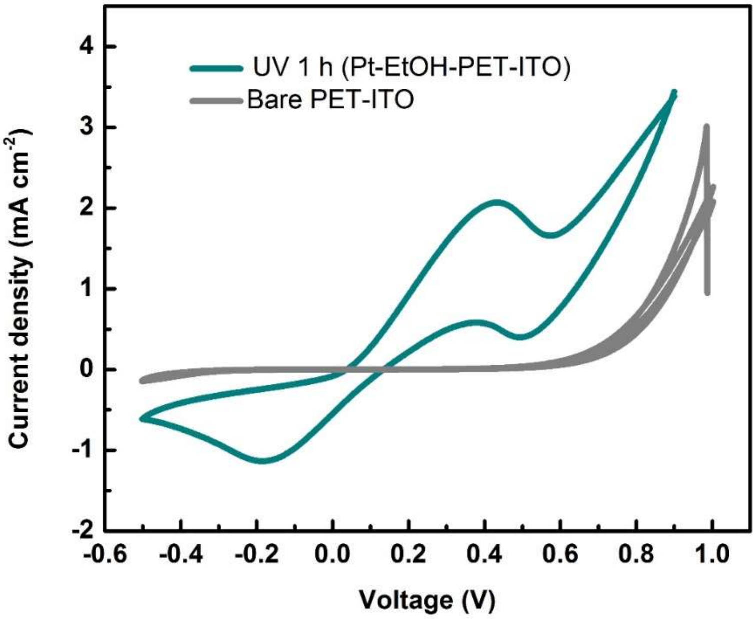

Figure 4.28: CV measurement scan of Pt-EtOH-ITO-PET with 1 h UV irradiation time

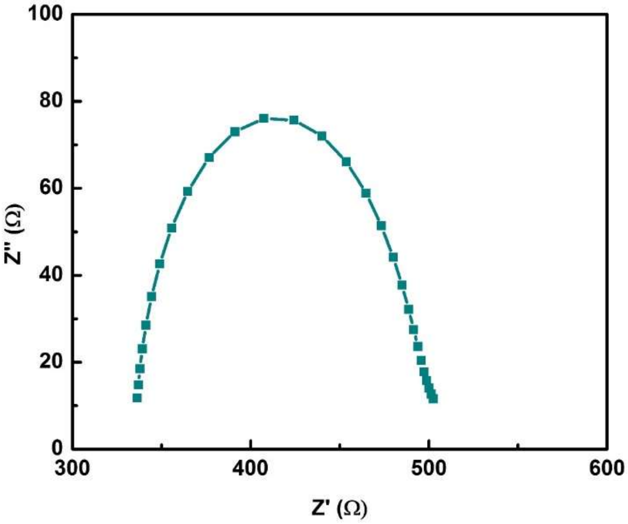

Figure 4.29: Nyquist plot of Pt-EtOh-ITO-PET Pt CE with 1 h UV irradiation time

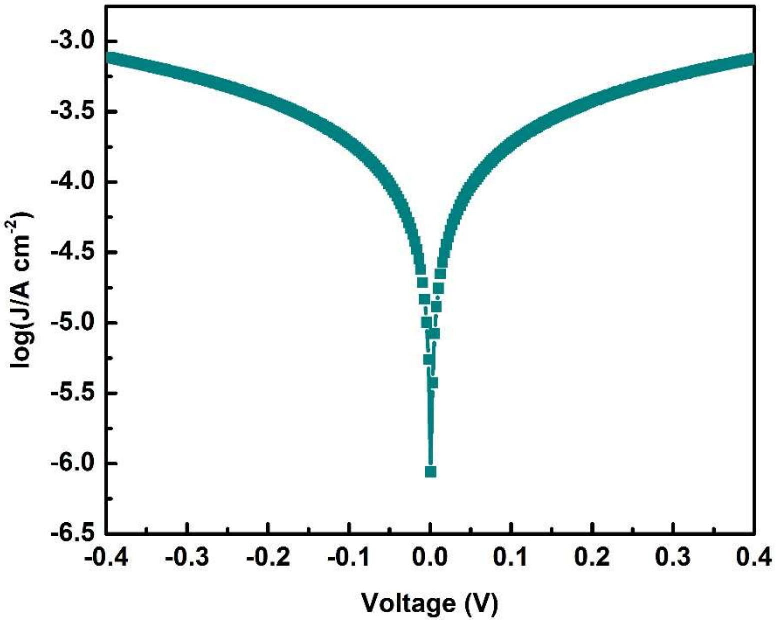

Figure 4.30: Tafel plot of photofabricated flexible Pt CE

4.1.5 Solar cells performance

Figure 4.31 shows the fabricated DSSCs for both rigid (left) and flexible (right) utilizing the photofabricated Pt CEs.

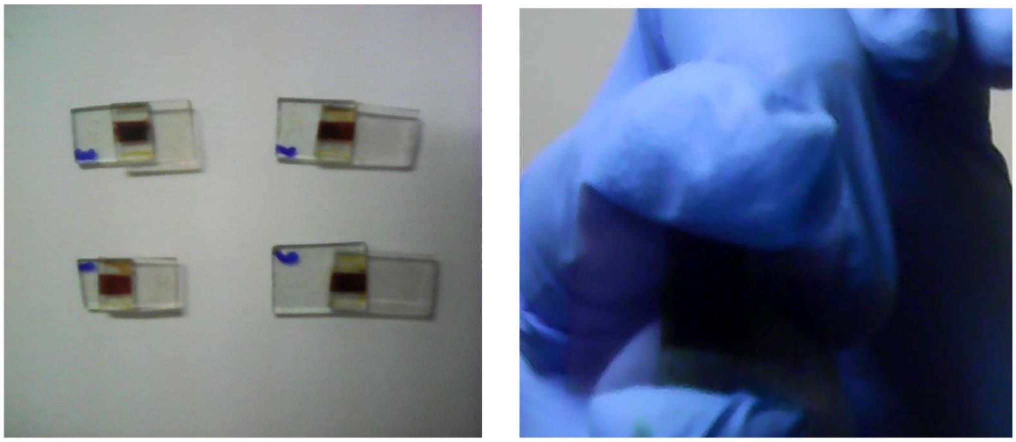

Figure 4.31: Photographic images of typical fabricate rigid DSSCs utilizing photofabricated Pt CEs (left) and flex-DSSC utilizing photofabricated flexible Pt CE (right)

The photovoltaic performances of all Pt CEs used in the fabrication of DSSCs were measured and the IV characteristics are given in Figure 4.32 and Figure 4.33 with front illumination. The photovoltaic parameters of the fabricated DSSCs using the photofabricated Pt CEs are listed in Table 4.2.

The photofabricated Pt CEs were used for the fabrication of bifacial DSSCs and their photovoltaic performances were measured under the illumination of AM 1.5 G solar simulator at 100 mW cm^{-2} light intensity. Typical DSSCs fabricated using the photofabricated Pt CEs while The front and rear illuminated DSSCs I-V parameters are summarized in Table 4.2. Figure 4.32 illustrates the front illumination I-V curve for the spin coated (Pt-EG-FTO). Figure 4.33 shows I V characteristic curve of ethanol based drop coated (Pt-EtOH-FTO) and Figure 4.34 is the I V characteristic curve of flex-DSSC utilizing the flexible (Pt-EtOH-ITO-PET) CEs. Figure 4.35 – 4.37 show the rear illumination I-V curves for the DSSCs fabricated with the respective Pt CEs. It is seen that the Pt CEs with 1 h UV irradiation time outperformed other Pt CEs with UV irradiation time other than 1 h for both EG and EtOH based fabricated Pt CEs respectively. Further confirming the good catalytic activities of Pt CEs fabricated with 1 h UV irradiation time as established by electrochemical CV, EIS and Tafel characterizations. Solvent effect shows EtOH based Pt CEs to be better and more efficient for DSSCs than EG based Pt CEs. Pt-EtOH-FTO CE with 1h UV photoreduction exhibited the best performance efficiency of 7.29 % and the highest open circuit voltage V_{OC} of 810 mV for front illumination. In a similar trend, DSSC utilizing Pt-EtOH-FTO CE with 30 min UV irradiation time performed better than all DSSCs fabricated with Pt-EG-FTO CEs with efficiency of 5.07 % as compared to the best EG based CEs of 5.01 % (for UV 1 h (Pt-EG-FTO)). It is noted that DSSCs fabricated employing Pt CEs with 4 and 5 spin coating cycles exhibit higher current density than those with 3 spin coating cycles. Flexible DSSC based on UV 1 h (Pt-EtOH-ITO-PET) CE and employing ZnO as photoanode recorded a PCE of 3.26 %.

All DSSCs employing photofabricated Pt CEs retained more than 77 % of their front illumination efficiencies when illuminated from the rear. The percentage ratio of the rear illumination efficiency to the front illumination efficiency (η_R) is given in Table 4.2. The h_R trend is consistent with the reported transmittance spectra of the photofabricated CEs. UV 2 h (Pt-EG-FTO) CE retained the highest percentage conversion efficiency ratio at 85.92 % slightly above 85.42 % of UV 1 h (Pt-EG-FTO) CE. Flexible DSSC recorded h_R

of 79.75 %. Hence, our photofabrication technique proved adequate for utilization in bifacial DSSCs. Difference in PCEs between front and rear illumination of DSSCs is observed to be largely due to the reduced photocurrent density of the rear illuminated DSSCs. This reduction in photocurrent density can be ascribed to electrolyte layer in the cell which behaved as a barrier between the incident light radiation and the dye sensitizer. The electrolyte is known to reflect incident light away, thereby reducing the amount of light available for the photoexcitation of the dye molecules.

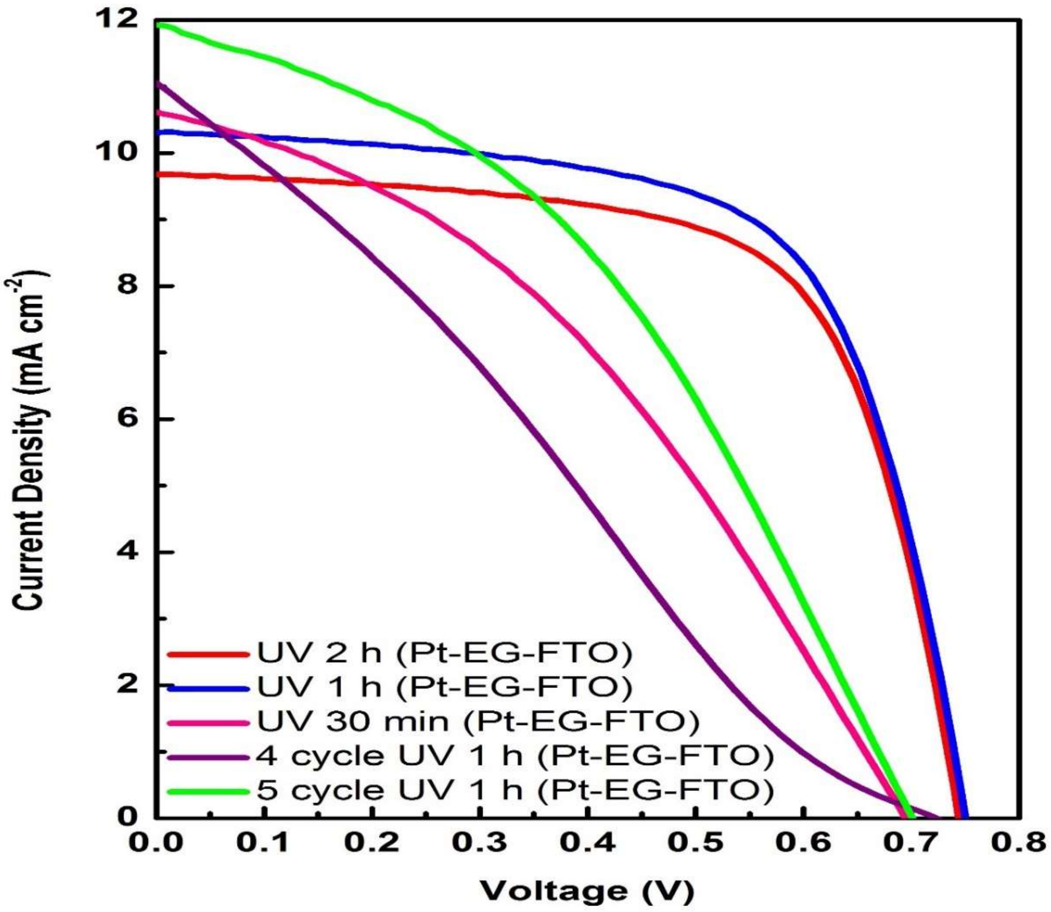

Figure 4.32: IV curve of DSSCs based on photofabricated Pt CEs (Pt-EG-FTO)

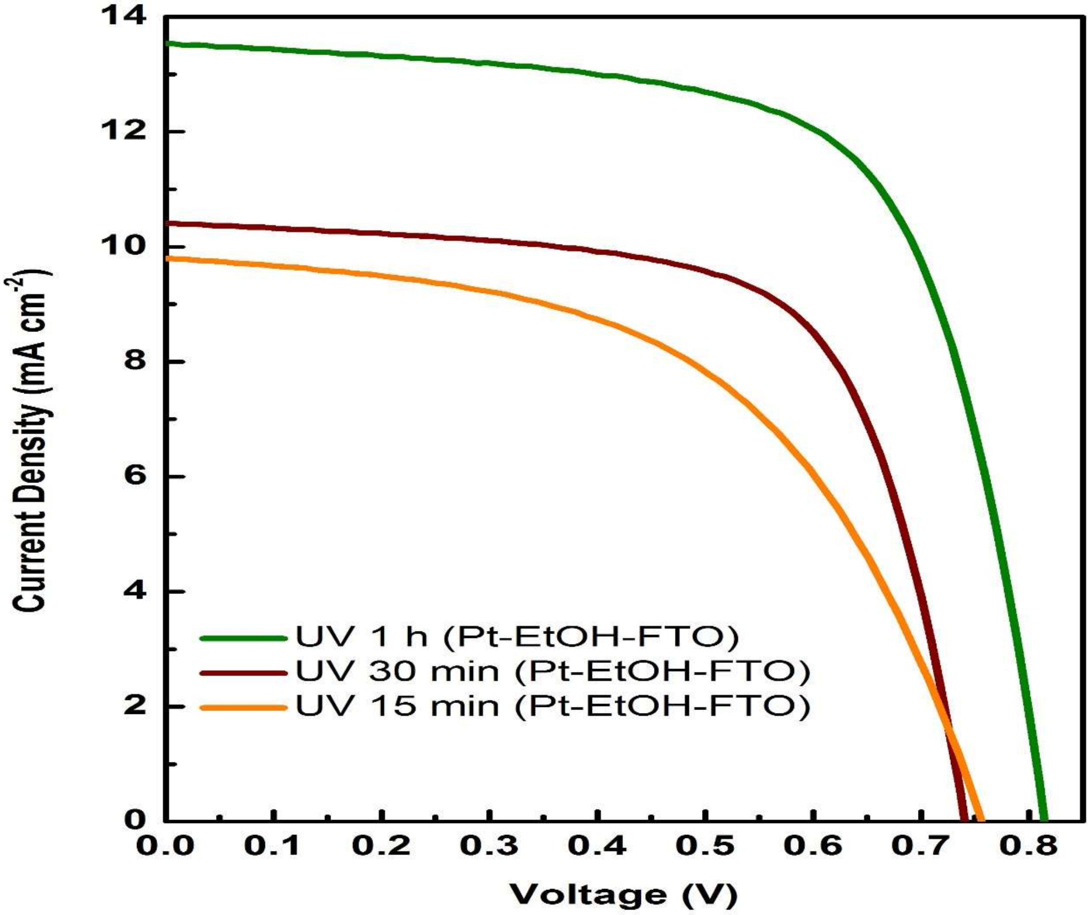

Figure 4.33: IV characteristics curve of DSSCs with photofabricated Pt CEs (Pt-EtOH-FTO)

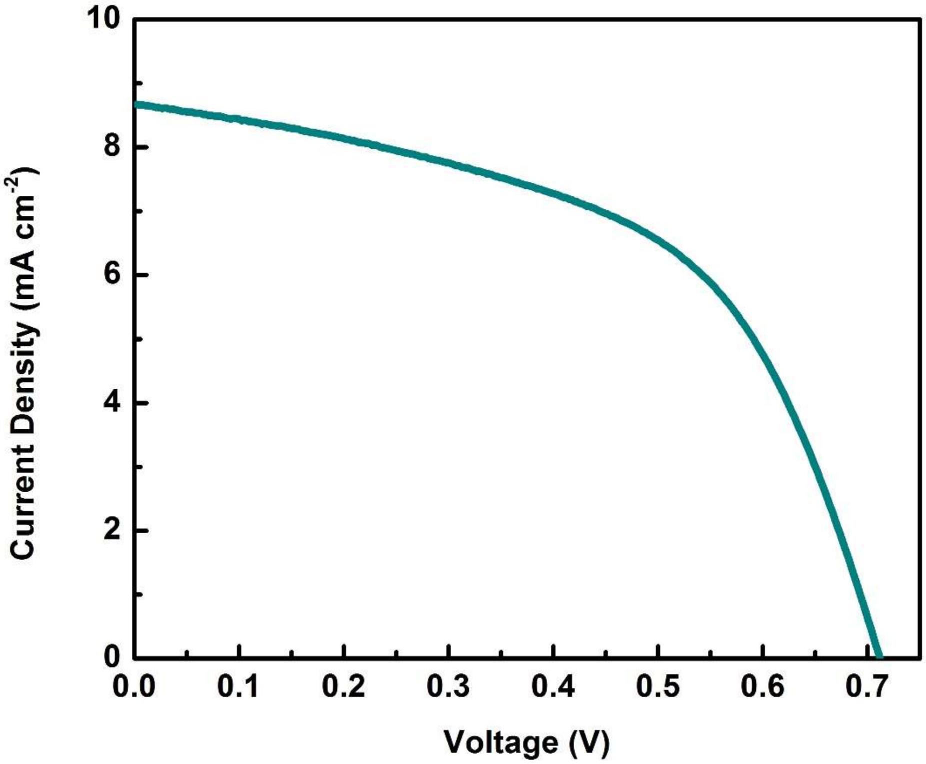

Figure 4.34: IV curve of flexible DSSC utilizing flexible photofabricated Pt CE

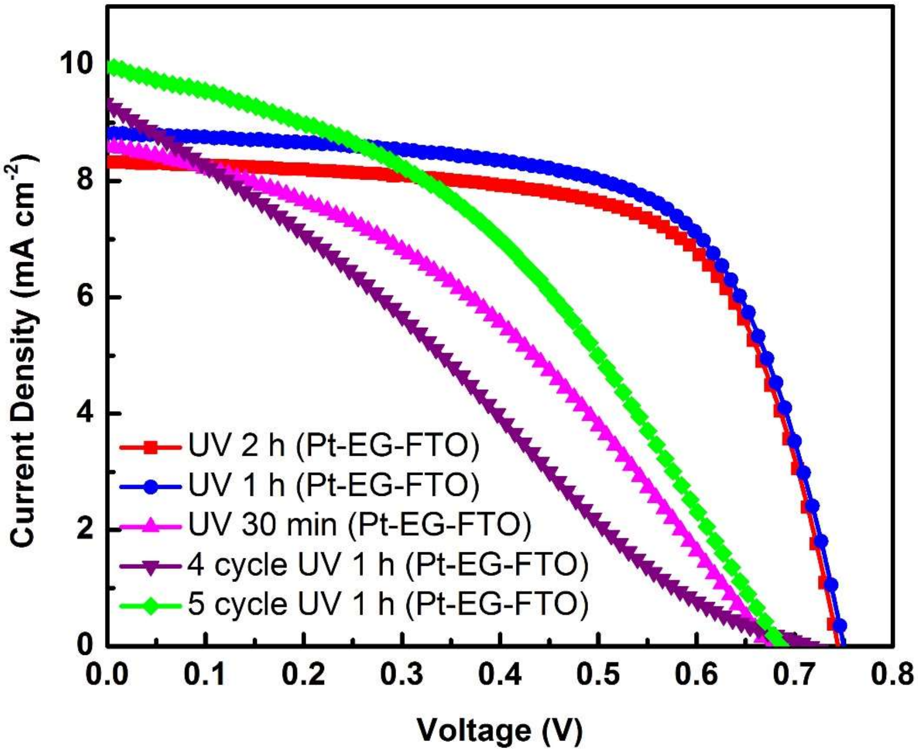

Figure 4.35: I V characteristics curves of rear illuminated DSSCs utilizing photofabricated (Pt-EG-FTO) Pt CEs

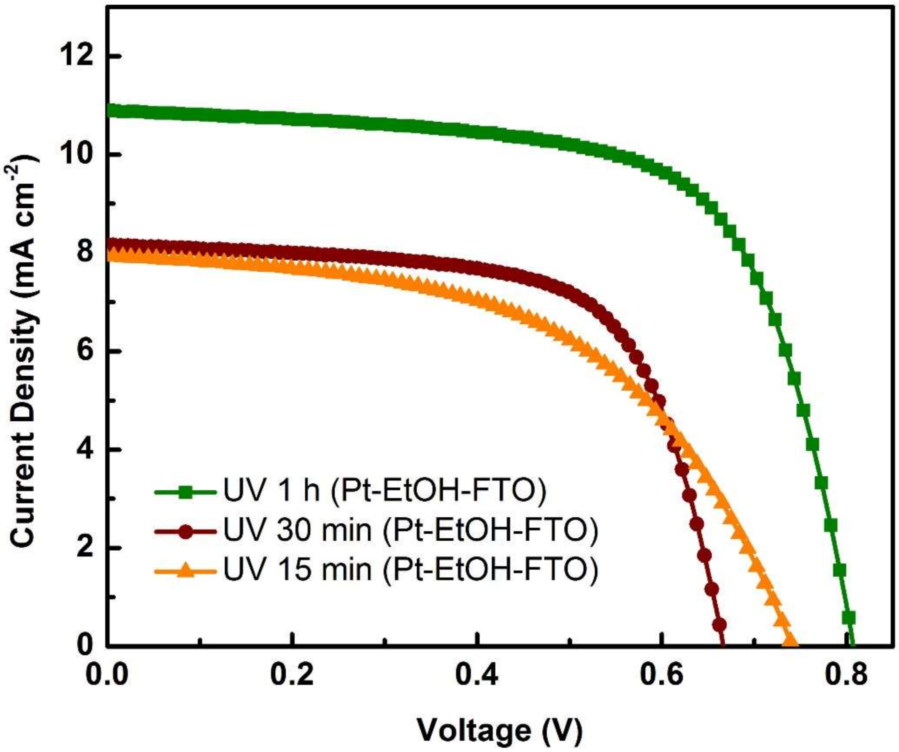

Figure 4.36: I V characteristics curves of rear illuminated DSSCs utilizing photofabricated (Pt-EtOH-FTO) Pt CEs

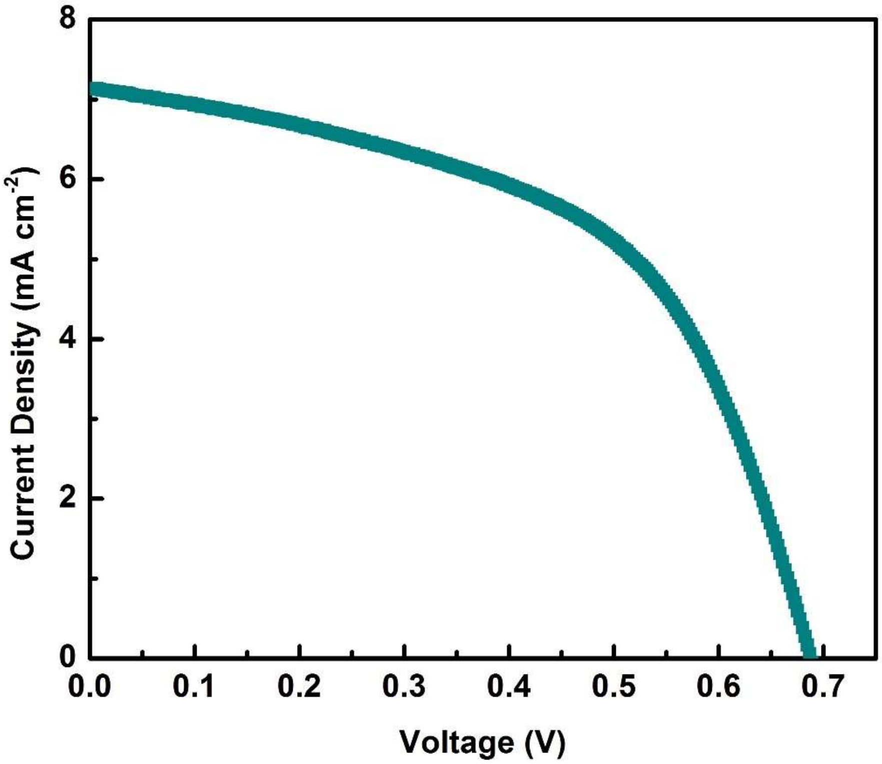

Figure 4.37: I V characteristics curves of rear illuminated flex-DSSC utilizing photofabricated (Pt-EtOH-ITO-PET) Pt CEs

As a reference for comparison, thermally fabricated Pt CE at 450 ºC was used to fabricate DSSC. An efficiency of 7.54 % was recorded slightly above the best photofabricated Pt CE DSSC. The photovoltaic parameters for this cell are listed in Table 4.2 for both front and rear illumination. Figure 4.39 showed the front and rear illumination I-V curves for the DSSC fabricated with thermally prepared Pt CE. The rear illumination photovoltaic performance significantly deviates from the performance recorded for the front illumination. The deviation can be seen to result from the drastic drop in photocurrent density of the rear illuminated DSSC which consequently led to significant loss in fill factor. The high reflectance (low transmittance) of the thermally prepared Pt CE as shown in Figure 4.38 is responsible for observed loss in photovoltaic parameters with a significantly reduced PCE of 2.71 %. A η_R 35.94 % was recorded for this cell, 41.97 % less difference when compared with the photofabricated CE having the least η_R of 77.91 %.

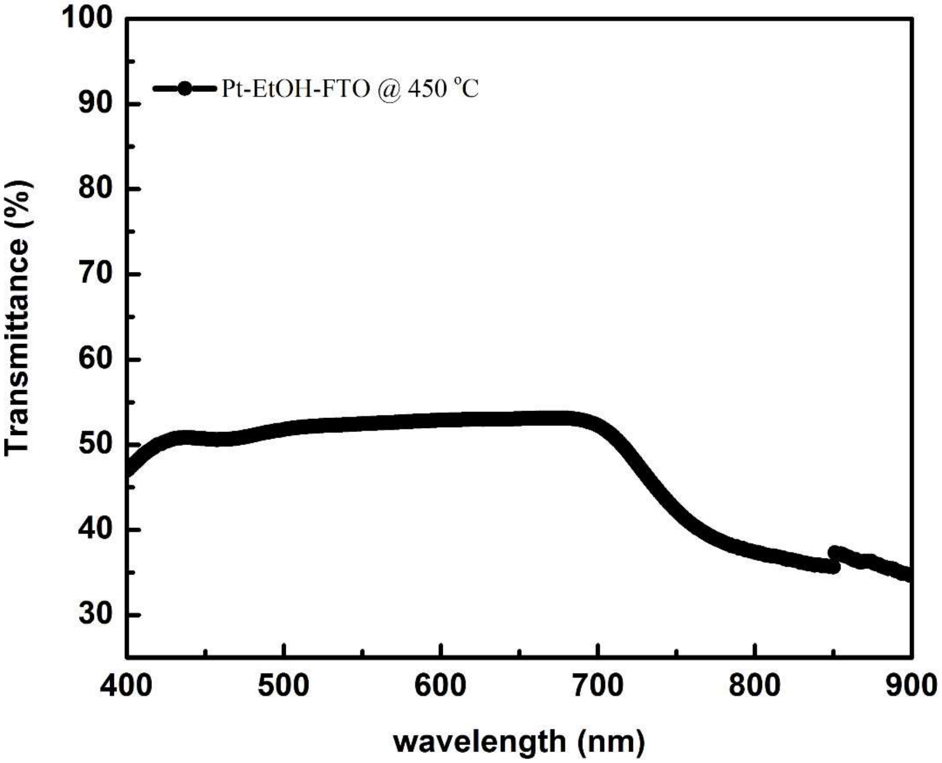

Figure 4.38: Transmittance spectrum of thermally fabricated Pt CE @ 450 °C

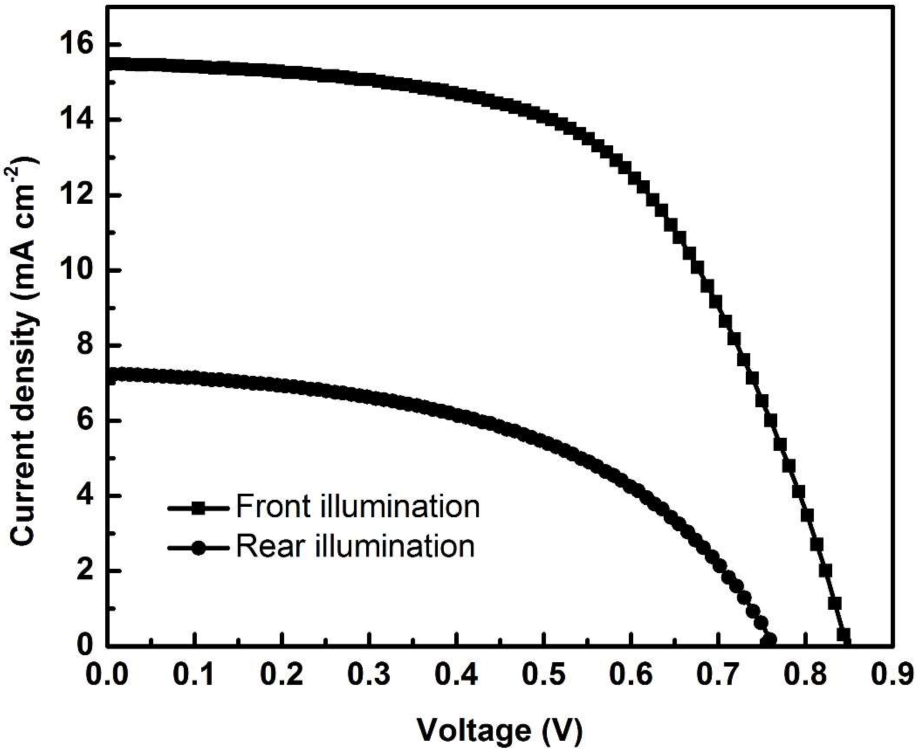

Figure 4.39: I V curve of Pt CE @ 450 ºC showing front and rear illumination performance

Table 4.2: Photovoltaic performance parameters of fabricated DSSCs utilizing photofabricated Pt CEs

Photofabricated Pt-CEs	**Illumination**	**J_{SC} (mA cm^{-2})**	**V_{OC} (V)**	**FF (%)**	**η (%)**	**η_R (%)**
UV 2 h (Pt-EG-FTO)	Front	9.68	0.74	66.47	4.76	85.92
	Rear	8.32	0.74	66.43	4.09	
UV 1 h (Pt-EG-FTO)	Front	10.31	0.75	64.90	5.01	85.42
	Rear	8.82	0.75	65.15	4.28	
UV 30 min (Pt-EG-FTO)	Front	10.59	0.69	38.49	2.81	79.36
	Rear	8.57	0.67	38.88	2.23	
4 cycles UV 1 h(Pt-EG-FTO)	Front	10.97	0.71	25.64	2.00	85.00
	Rear	9.25	0.72	25.52	1.70	
5 cycles UV 1 h (Pt-EG-FTO)	Front	11.91	0.70	41.04	3.42	79.23
	Rear	9.95	0.68	40.19	2.71	
UV 1 h (Pt-EtOH-FTO)	Front	13.53	0.81	66.56	7.29	80.25
	Rear	10.89	0.802	67.03	5.85	
UV 30 min (Pt-EtOH-FTO)	Front	10.40	0.74	66.77	5.07	77.91
	Rear	8.16	0.72	67.18	3.95	
UV 15 min (Pt-EtOH-FTO)	Front	9.79	0.75	53.10	3.92	78.57
	Rear	7.93	0.74	52.62	3.08	
UV 1 h (Pt-EtOH-PET-ITO)	Front	8.67	0.71	53.35	3.26	79.75
	Rear	7.14	0.687	53.02	2.60	
Pt-EtOH-FTO @ 450 ºC	Front	15.49	0.84	57.73	7.54	35.94
	Rear	7.225	0.759	49.51	2.71	

4.2 CuO P-type Dye Sensitized Solar cells

CuO was synthesized from Cu powder dispersed in DI water an ablated for 30 min using Nd-YAG pulsed laser. The synthesis of the CuO from Cu powder was observed from change in colour of the dispersed Cu powder. The dispersed Cu powder changes from red to black after it has been converted to CuO by laser ablation as shown in Figure 4.40. The as-synthesized CuO was characterized by SEM, TEM, XRD, XPS, UV-Vis prior to usage in dye sensitized solar cells. The dependence of I-V performance of the CuO as a function of N719 solvent variation was equally examined, so was absorbance of the dye desorption investigated in order to understand the role of the N719 solvent in cell performance of p-type CuO DSSCs.

Figure 4.40: Photographic images showing Cu powder dispersed in DI water before ablation (left) and CuO colloid in DI water after ablation (right)

Compositional, morphological, optical and structural characterizations

The element composition of the as-synthesized nanospherical CuO was investigated by XPS. The XPS survey in Figure 4.41 shows the as-synthesized CuO to be pure and Figure 4.42 confirmed the Cu component to be Cu^{2+} ionic state due to the strong satellite peaks that can be seen at 942 eV and 961 eV. Hence, establishing the formation of CuO by PLAL. The morphology of the as-synthesized CuO revealed a nanosphere CuO particles with sizes ranging from 30 nm to 200 nm. The large particles observed in the SEM image of Figure 4,43a are due to agglomeration of the as-synthesized sample in DI water. Few non-spherical nanoparticles could also be seen in the SEM image. The TEM image shown in Figure 4.43b confirmed the nanospherical morphology of the as-synthesized CuO with structure ranging from 10 nm to about 40 nm.

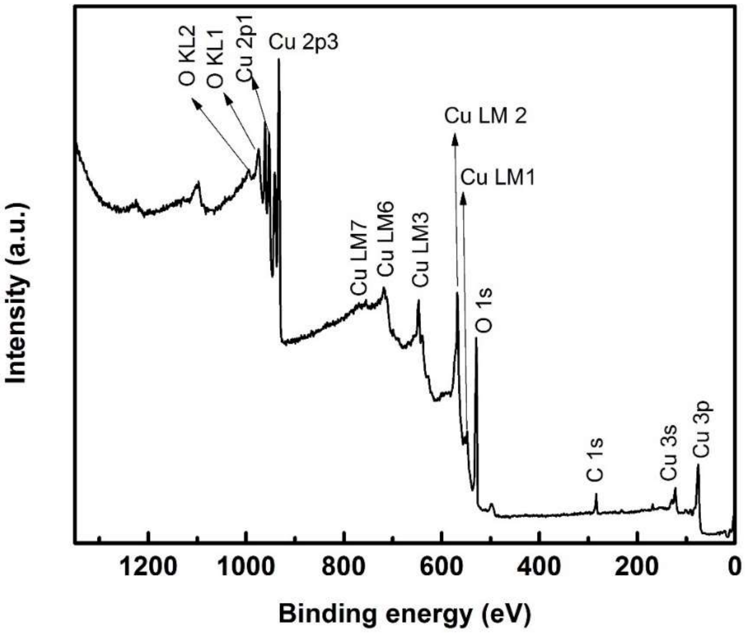

Figure 4.41: XPS survey spectrum of as-synthesized CuO

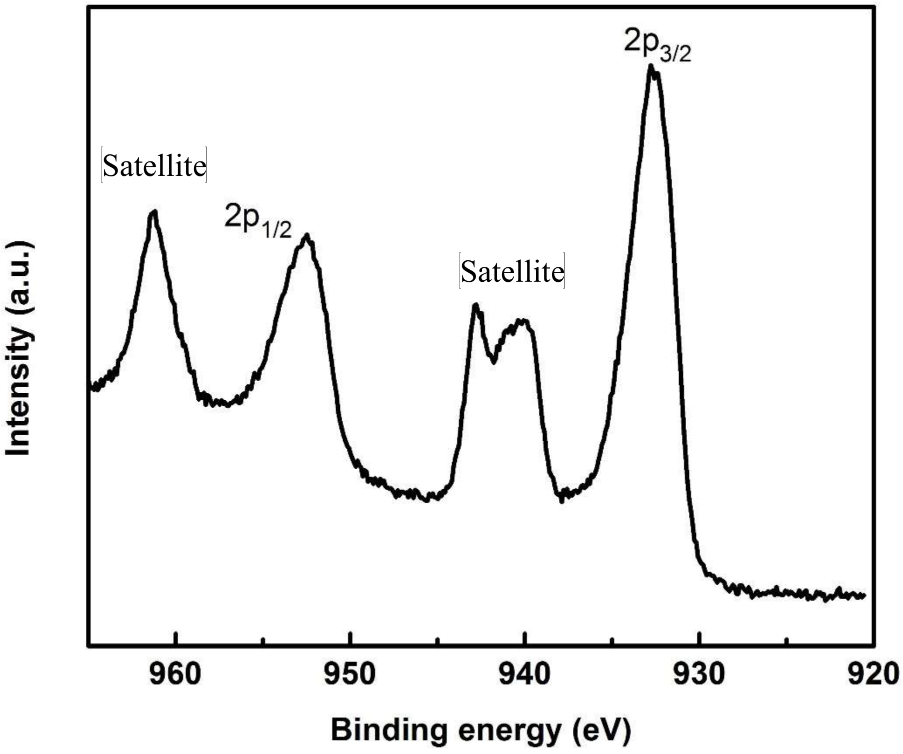

Figure 4.42: XPS spectra of Cu 2p state of the as-synthesized CuO

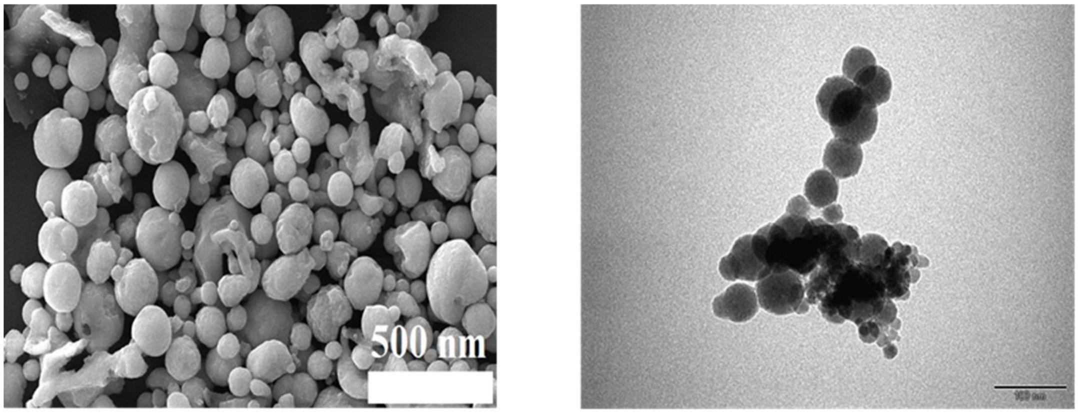

Figure 4.43: a) SEM image of as-synthesized CuO nanosphere b) TEM image of as-synthesized CuO nanospheres

The crystal structure of the synthesized CuO was investigated by XRD. The XRD peaks shown in Figure 4.44 confirm the crystallinity of the synthesized CuO with no impurity peaks recorded. The XRD manifest a simple cubic structure.

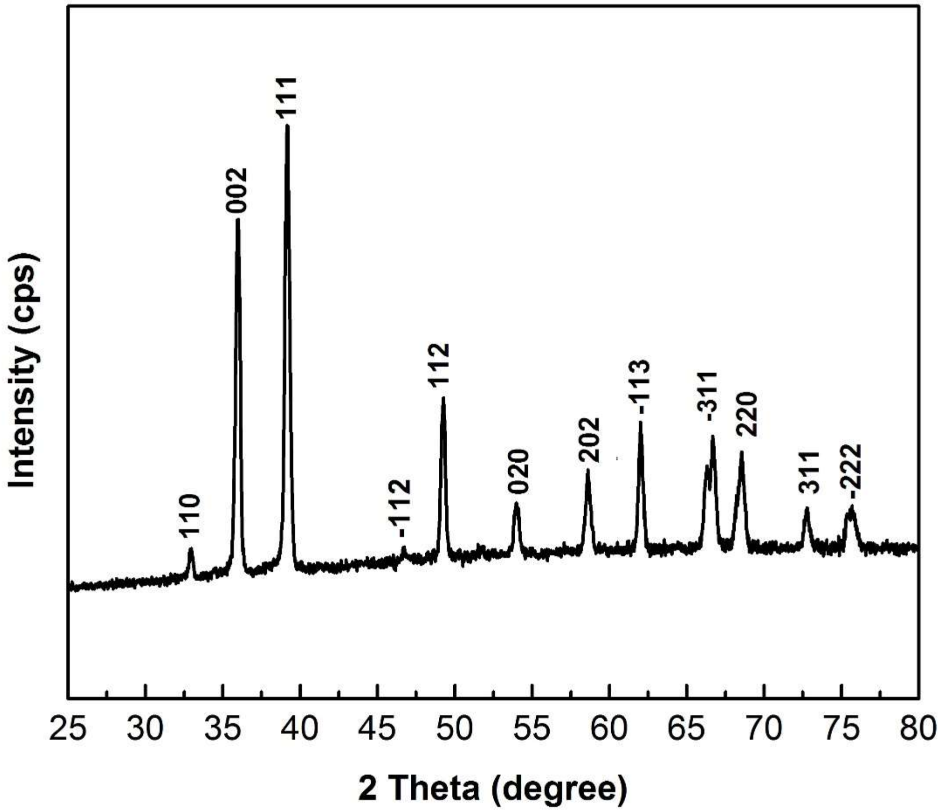

Figure 4.44: XRD spectra of CuO nanosphere synthesized by PLAL

The absorbance spectra of the CuO nanosphere is given in Figure 4.45 The absorbance spectra showed relatively low broad peak across the visible light region and high narrow peaks in the ultraviolet light region. The energy band gap of the synthesized CuO was deduced using the Tauc plot technique as shown in Figure 4.46 and an energy band gap of 3.54 eV was recorded.

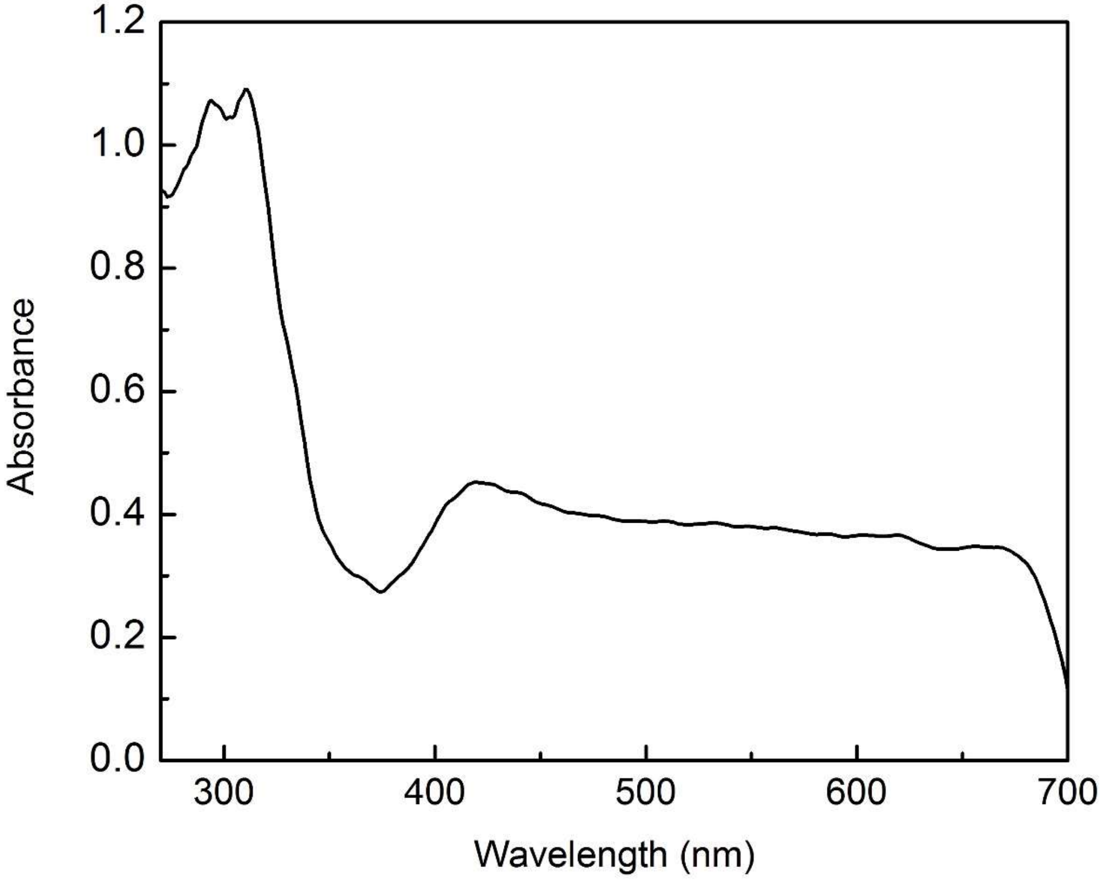

Figure 4.45: Absorbance spectra of CuO nanosphere synthesized by PLAL

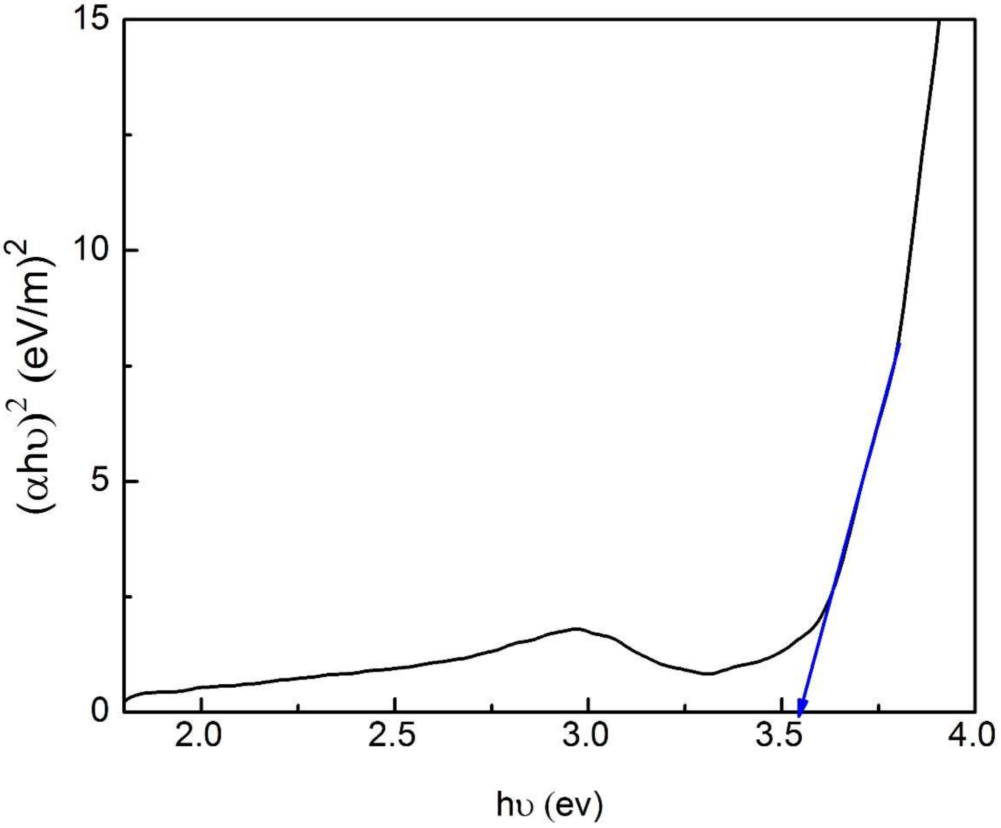

Figure 4.46: Tauc plot derived from the absorbance of the synthesized CuO with the energy gap indicated by the extrapolated line

I V characterization

The as-synthesized CuO was used for the fabrication of p-type DSSCs in N719 dye prepared using ethylene glycol (EG), methanol and propanol. Figure 4.47 shows the images of the fabricated p-type CuO DSSCs in all respective N719 solvents.

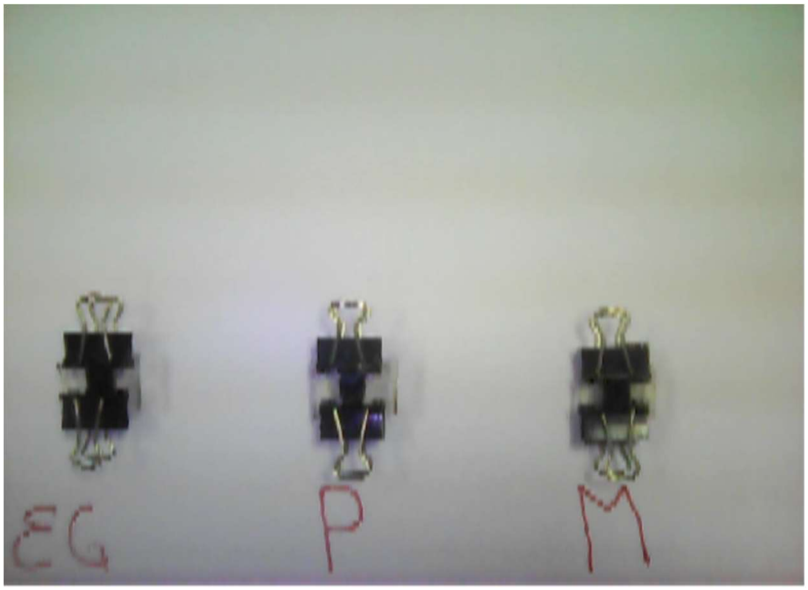

Figure 4.47: Photographic images of fabricated p-type CuO DSSCs in different N719 solvents of ethylene glycol, propanol and methanol

Figure 4.48 gives the IV curve of the fabricated p-type DSSCs in the three solvents. Methanol based N719 p-type DSSC showed the poorest device performance with current density (J_{SC}) of 0.1 mA cm^{-2} and a voltage of 160 mV with fill factor 21.04 % and power conversion efficiency of 0.00032 % respectively. Propanol based N719 p-type DSSC exhibits the highest current density (J_{SC}) of 0.227 mA cm^{-2} and the least open circuit voltage V_{OC} of 140 mV with fill factor 23.34 % and power conversion efficiency of 0.0082 % respectively. EG based N719 dye showed the highest photovoltaic conversion efficiency of 0.0340 % with open circuit voltage V_{OC} of 390 mV and fill factor of 41.04 % respectively. Current density of 0.2 mA cm^{-2} was recorded for the cell. The photovoltaic performance parameters are listed in Table 4.3

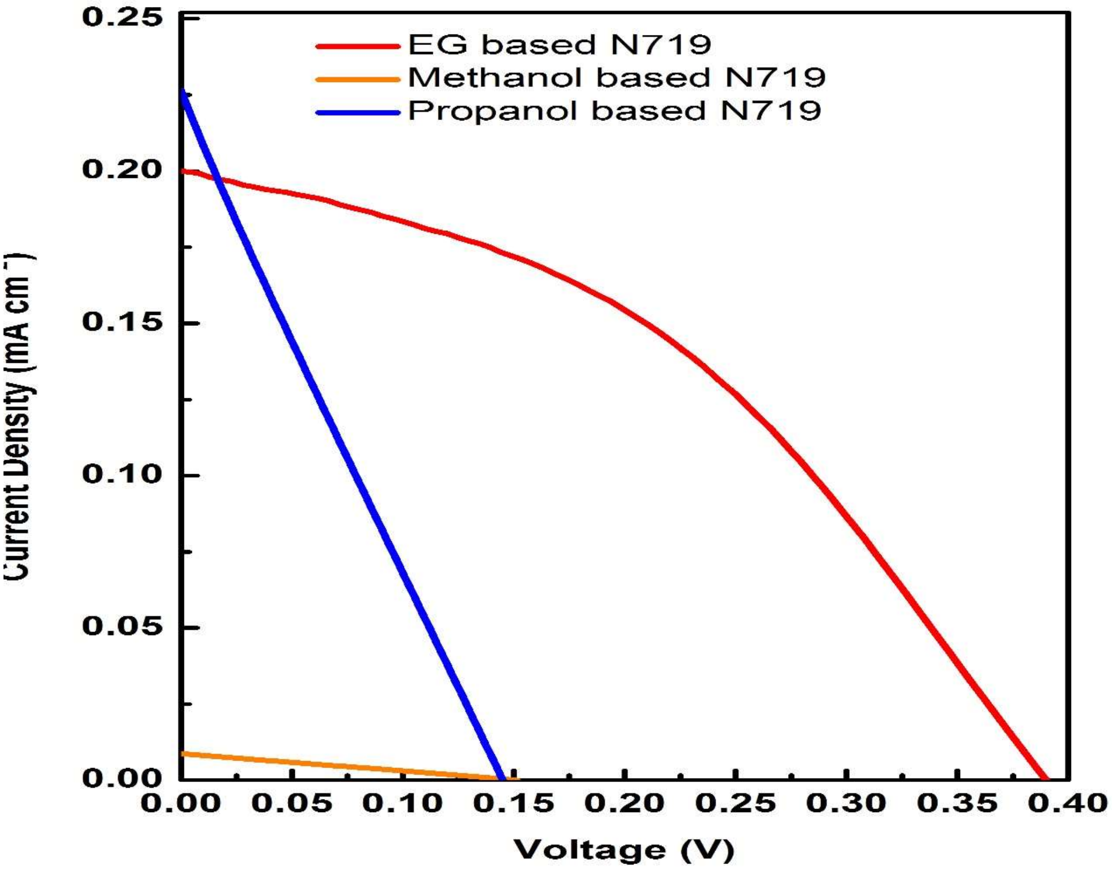

Figure 4.48: IV charateristic vurve of CuO p-type DSSCs based on different N719 dye

The Nyquist plot of the electrochemical impedance spectroscopy of the three fabricated p-type DSSCs are shown in Figure 4.49. The inset shows the equivalent circuit used for the fitting og the Nyquist curves. Methanol based N719 DSSC showed very high series resistance and charge transfer resistance. These could explain the reason for the low current density recorded for this sample. Propanol based N719 DSSC exhibited relatively low series and charge transfer resistances compared with the other two cells. These low resistance values are consistent with the high current density recorded by the propanol based N719 DSSC sample.

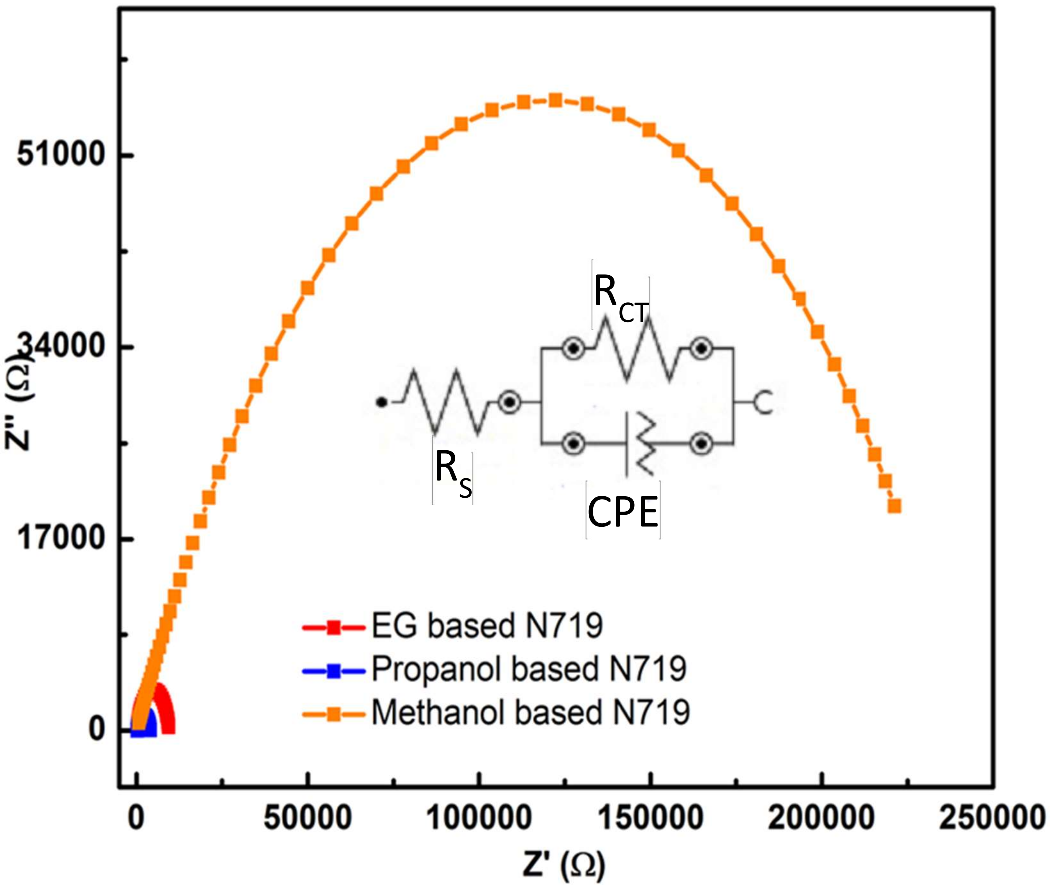

Figure 4.49: Nyquist plots of p-type CuO DSSCs with different N719 solvents

Figure 4.50 shows the magnified plot for the Nyquist plot of propanol based N719 DSSC and EG based N719 DSSC. Figure 4.51 is the Bode plots of the fabricated p-type DSSCs with the equation of photogenerated electron lifetime embedded in the plots.

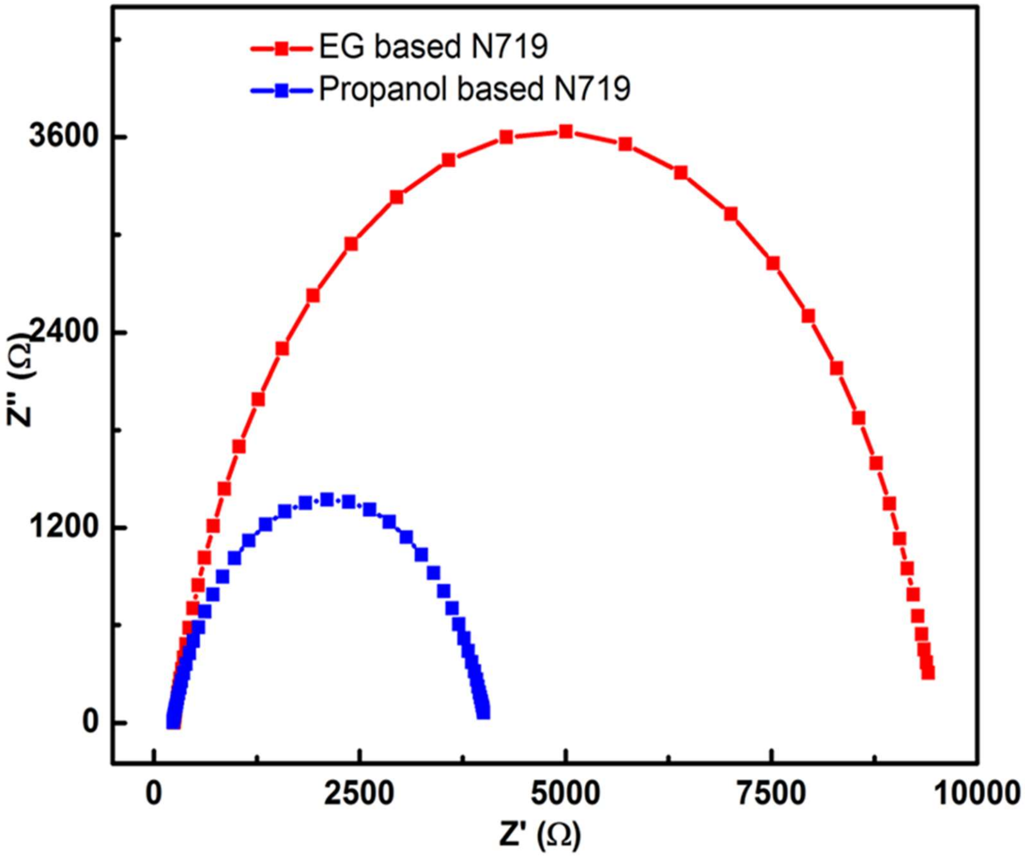

Figure 4.50: Nyquist plots of DSSCs based on EG and propanol N719 solvents showing magnified plots

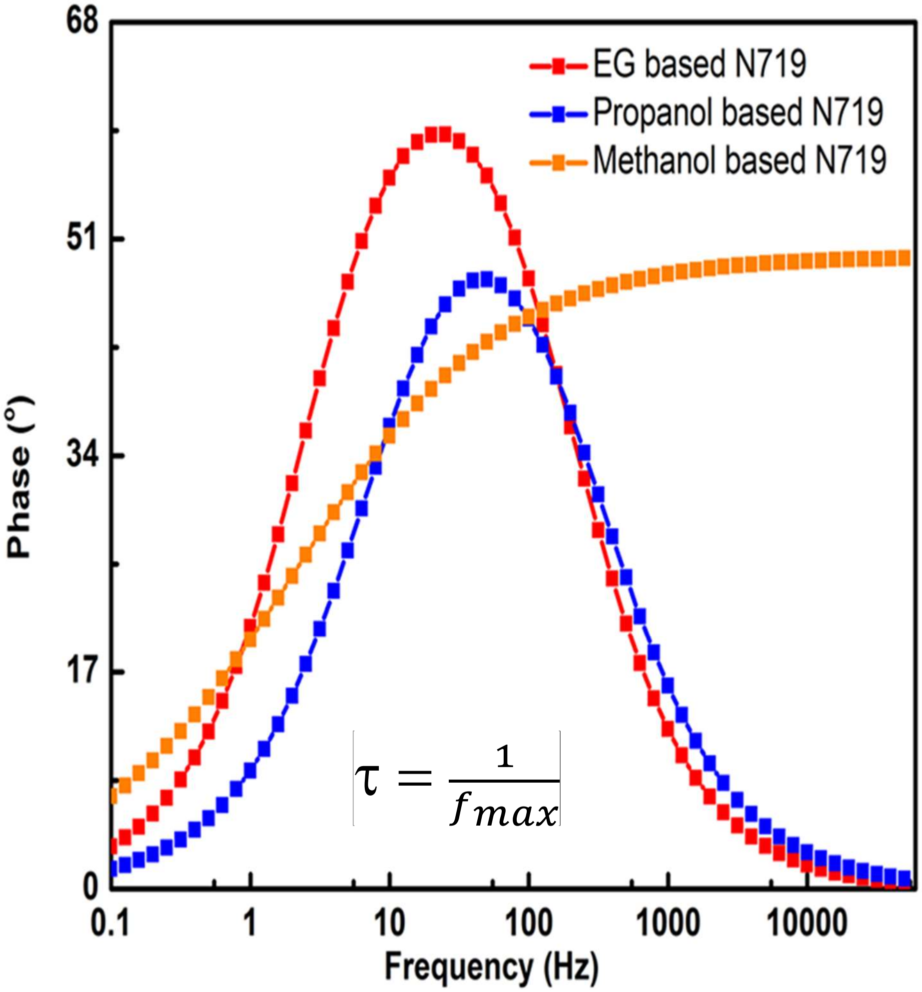

Figure 4.51: Bode plots of fabricated p-type CuO DSSCs utilizing N719 in different solvents

Table 4.3: IV characteristics of CuO p-type DSSC in different N719 dye solvents

Sensitizer	J_{SC} (mA cm^{-2})	V_{OC} (V)	FF (%)	η (%)	R_S (Ω)	R_{CT} (kΩ)	CPE (μF)	τ (s)
N719-EG	0.20	0.39	41.04	0.034	130.57	9.4359	6.217	0.0399
N719-PrOH	0.25	0.14	23.34	0.0082	254.23	3.66	4,9742	0.02
N719-MtOH	0.01	0.15	21.04	0.00032	3024.6	218.48	0.27419	0.00002

Dye-adsorption in the three different N719 dye solvents

In order to understand the influence of dye adsorption on CuO p-type DSSC, 1 ml 0.1 M NaOH was used to desorb the absorb dye by each of the CuO photocathodes in all three solvents based N719 dye. Figure 4.52 shows the UV-Vis absorbance spectra of the desorb dye in NaOH. EG based dye showed the highest absorbance peak in both visible and ultraviolet light spectra. The peaks in the UV region is considerably higher than that in the visible light region. Both propanol and methanol based N719 dye sensitizers are almost aligned across the UV-Vis light spectra. Propanol based N719 dye showed slightly higher peak between 500 nm and 900 nm wavelengths than methanol based N719 dye sensitizer. While methanol based n719 showed higher peaks across the UV region that the propanol based N719 dye sensitizer.

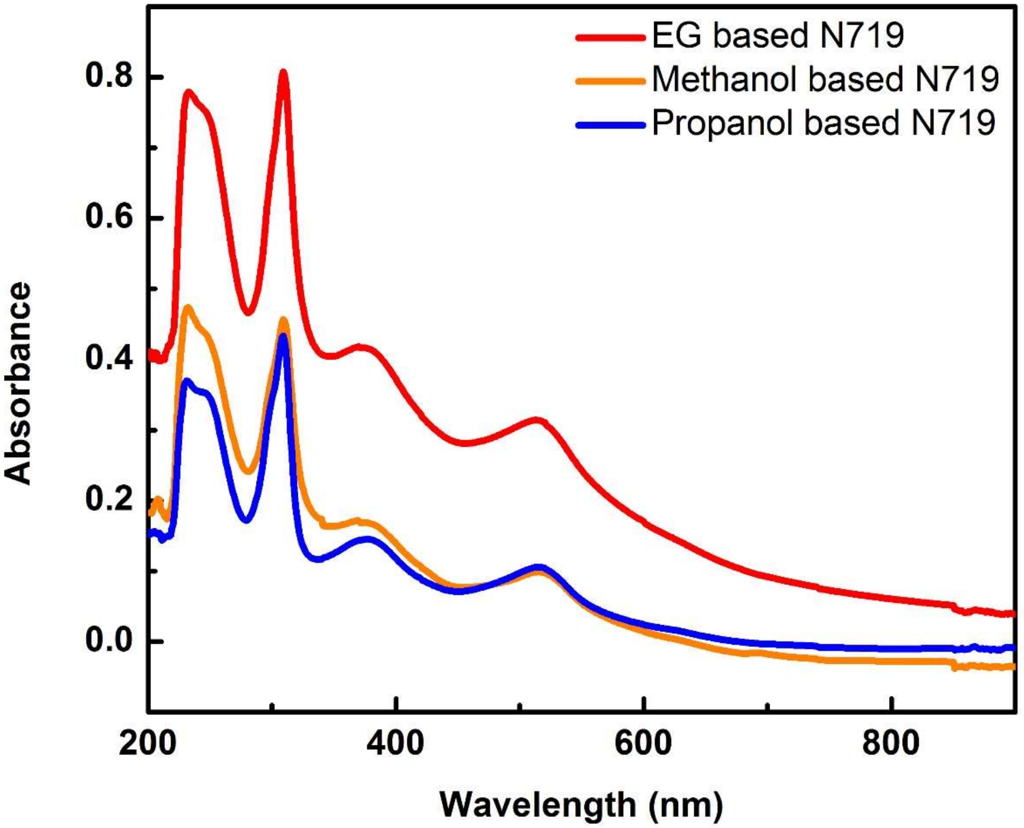

Figure 4.52: Absorbance of the desorped N719 dye of the three solvent in 2 ml NaOH

4.3 Cesium trimethyl ammonium mixed halides lead-free perovskite solar cells

Morphology and crystal structure

Figures 4.53 and 4.54 show the SEM images of CsCl:MAI (1:9) and CsCl:MAI (3:7) respectively. The two samples showed the presence hexagonal and bar-like morphologies in micrometer scale. The large size particles are particular advantageous for perovskite solar cells as would have long diffusion length within the particle and prevent recombination photogenerated electron-hole pairs. Figure 4.53 shows more hexagonal structure particles than the bar-like particles while population of bar-like particles are more prominent in the SEM images of Figure 4.54. These observations suggest that the hexagonal structures result from the MAI-BiI_3 while the bar-like structure is from the CsCl materials as the SEM of the two samples manifest the combination proportion of the mixed cation and mixed halides lead-free perovskite solar cells.

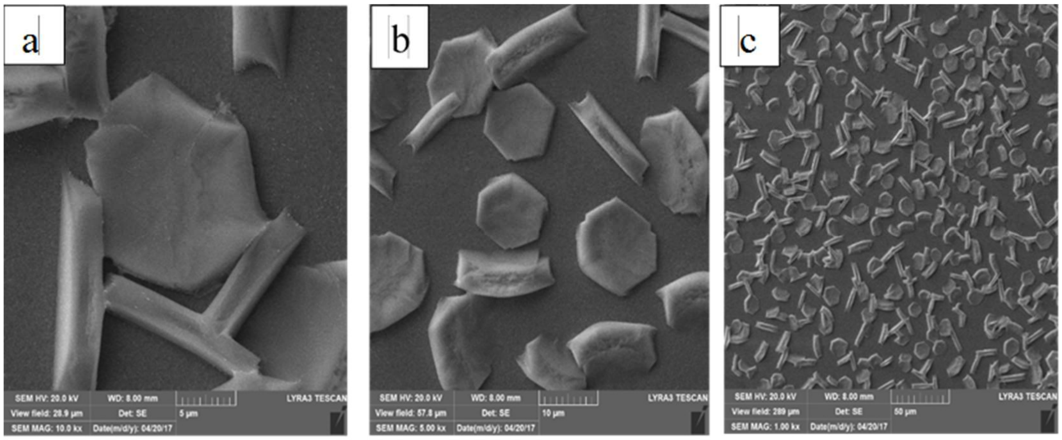

Figure 4.53: SEM images of CsCl:MAI (1:9) lead-free Bismuth perovskite

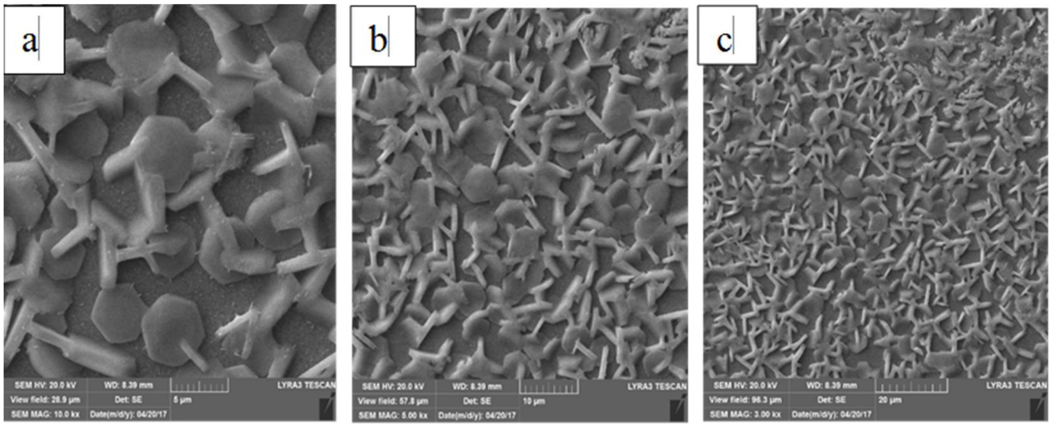

Figure 4.54: SEM images of CsCl:MAI (3:7) lead-free Bismuth perovskite

The crystal structure of the perovskite samples was determined by dissolving the respective samples ratio in 2 ml methanol and sonicated in an ultrasonic bath for 30 min. The samples solutions were transferred into another vial and left inside fume hood overnight to allow for the evaporation of methanol. The samples were taken from the vials and placed on sample holders' measurement and determination of the single crystals structure of the mixed cation and mixed halides lead-free bismuth perovskites. The XRD pattern of the synthesized perovskite is given as shown in Figure 4.55. All peaks marched database suggested materials with Br appearing in place of Cl. This is probably due to the absence of the chemical composition of the synthesized perovskite samples in the database. And since Br and Cl are same halides materials family the database suggested Cesium trimethyl bismuth iodobromide was used to fit the peaks of the synthesized perovskite materials.

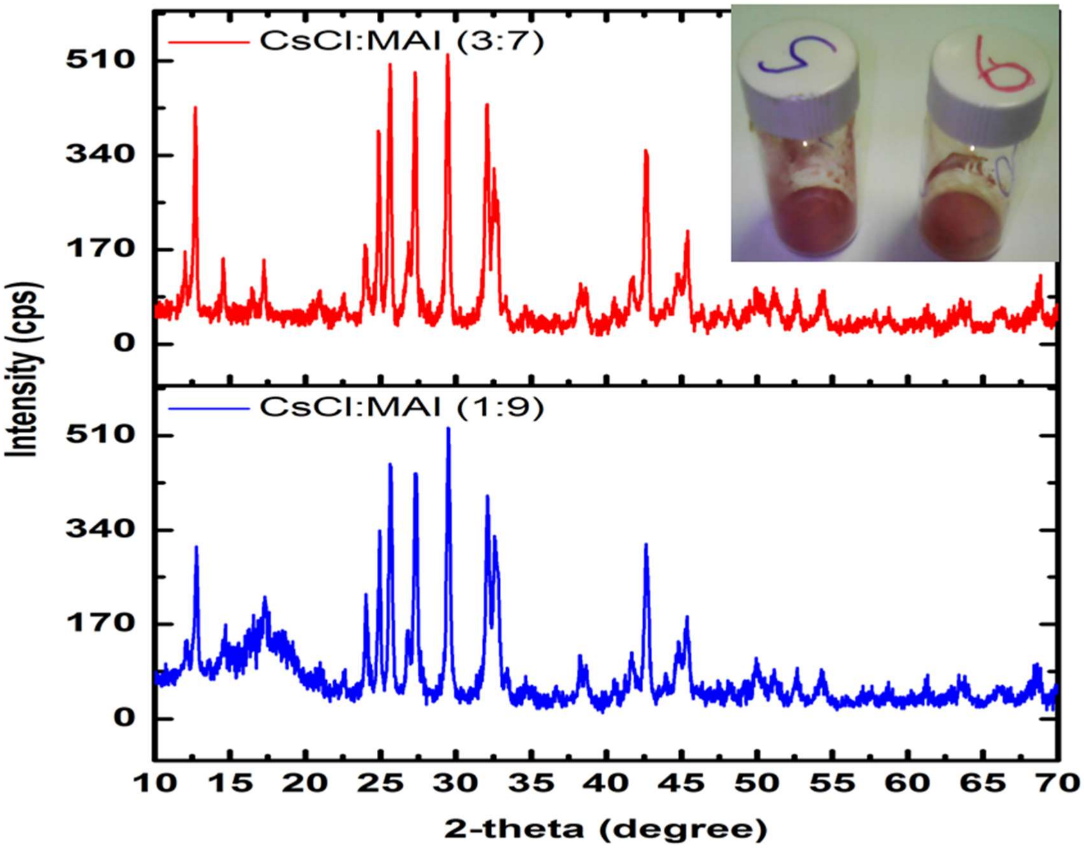

Figure 4.55: XRD pattern of the CsCl:MAI lead-free Bismuth perovskite

The light absorbance spectra of the synthesized perovskites samples were measured by UV-Vis spectra measurement. The two synthesized samples visible light responsiveness with broad peaks within the visible light spectrum. Figure 4.56 shows the absorbance spectra of the samples.

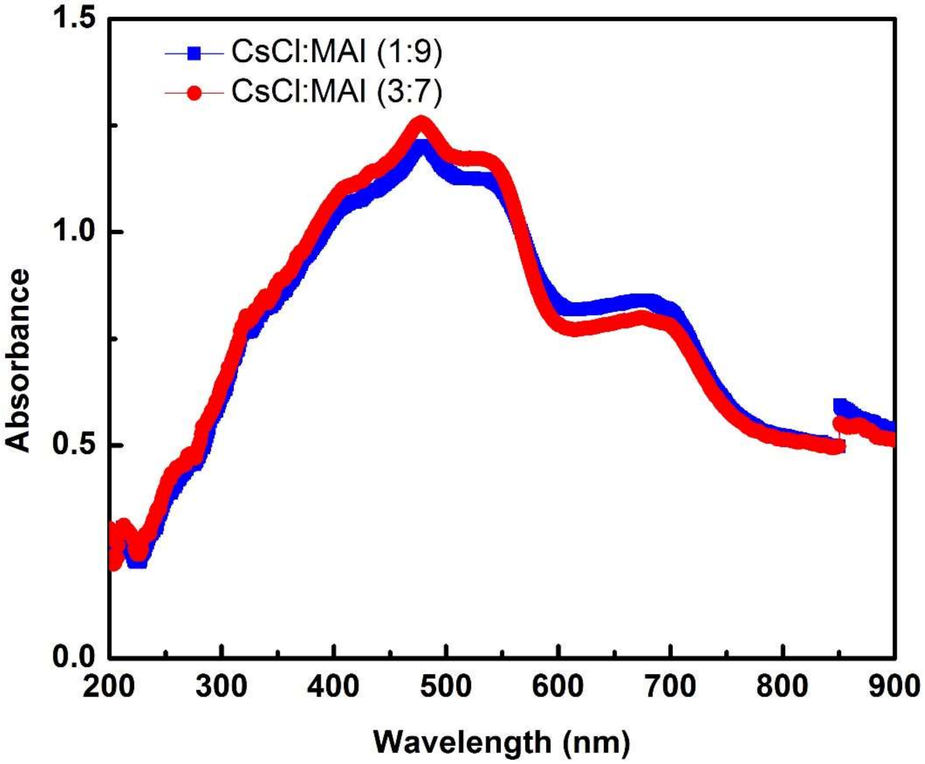

Figure 4.56: Absorbance spectra of the CsCl:MAI lead-free Bismuth perovskite

The samples showed visibly semitransparency, hence the transmittance of the samples were measured. The two samples have their transmittance spectra overlapping across the visible light region as shown in Figure 4.57.

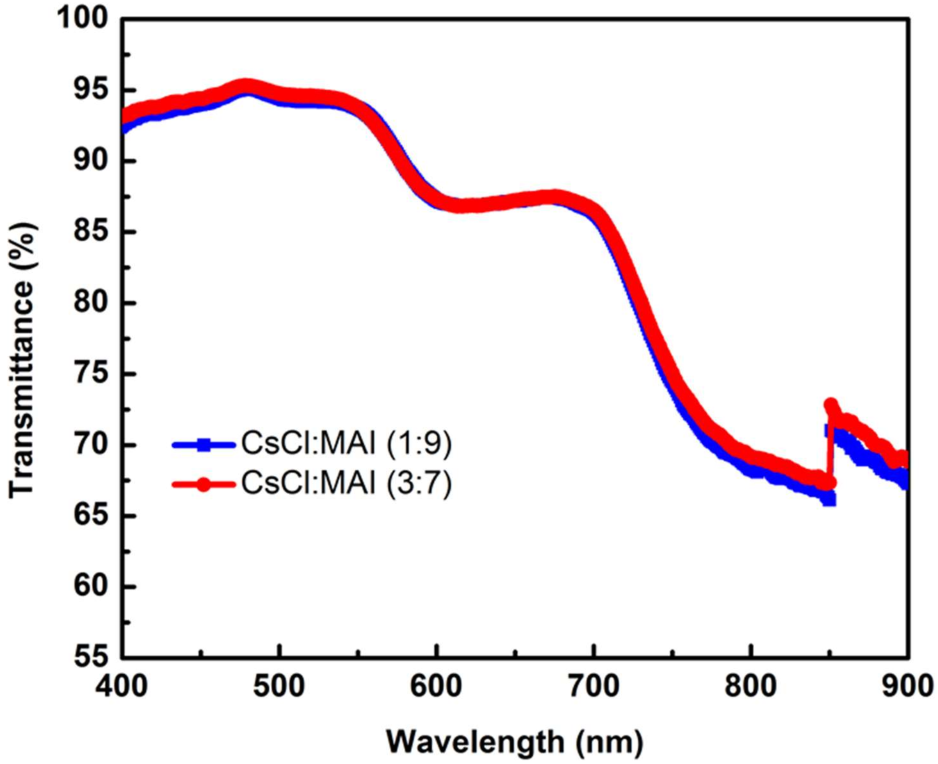

Figure 4.57: Transmittance spectra of the CsCl:MAI lead-free Bismuth perovskite

I V characteristics

The I-V characteristics of the photovoltaic performance of the mixed cation and mixed halides lead-free bismuth perovskite were measured using Autolab potentiostat PG302N equipped with NOVA 1.11 software. Oriel lamp solar simulator calibrated to 100 mW cm^{-2} was as light illumination source for the IV characteristic measurement. An area of 0.25 cm^{-2} was exposed for the measurement. Figure 4.58 shows the I-V curve of the perovskite samples and the photovoltaic parameters are listed in Table 4.4.

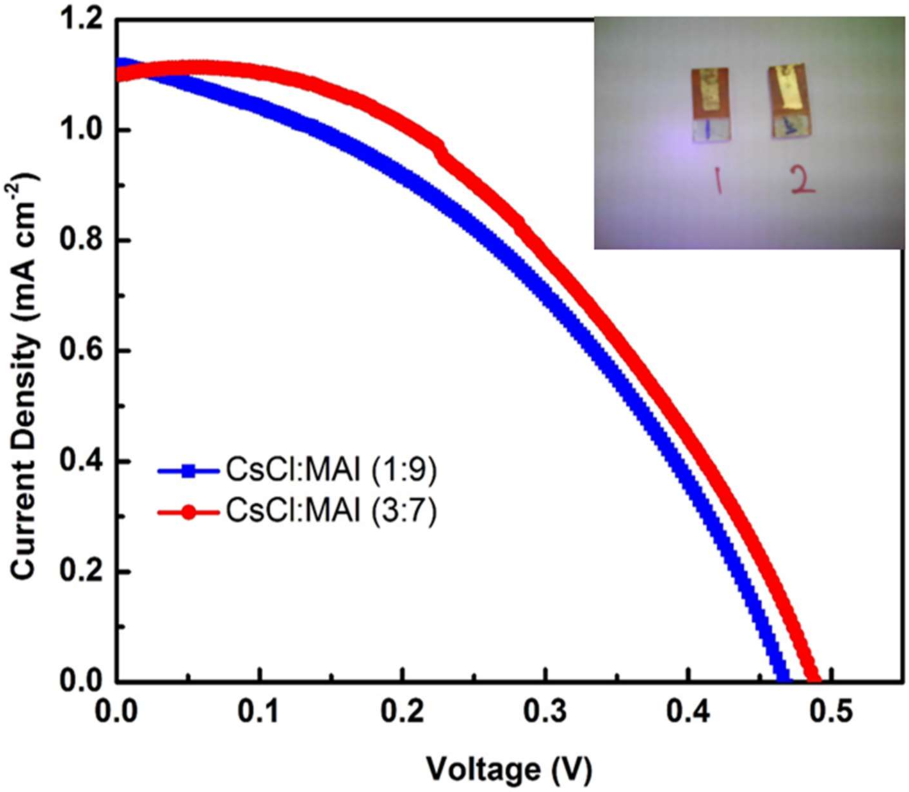

Figure 4.58: IV characteristic curve of the CsCl:MAI lead-free Bismuth perovskite solar cells. Inset is photographic image of the fabricated PSCs.

Electrochemical Impedance Spectroscopy

Electrochemical impedance spectroscopy Nyquist plots of the perovskite samples are as shown in Figure 4.59, inset is the equivalent circuit utilized for the fitting of the Nyquist plots for obtaining the respective Nyquist parameters. The Nyquist plots parameters are given in Table 4.4. The lifetime (τ) of the photogenerated electron can be estimated from the Bode plot in Figure 4.60 as the inverse of the frequency at the maximum peak.

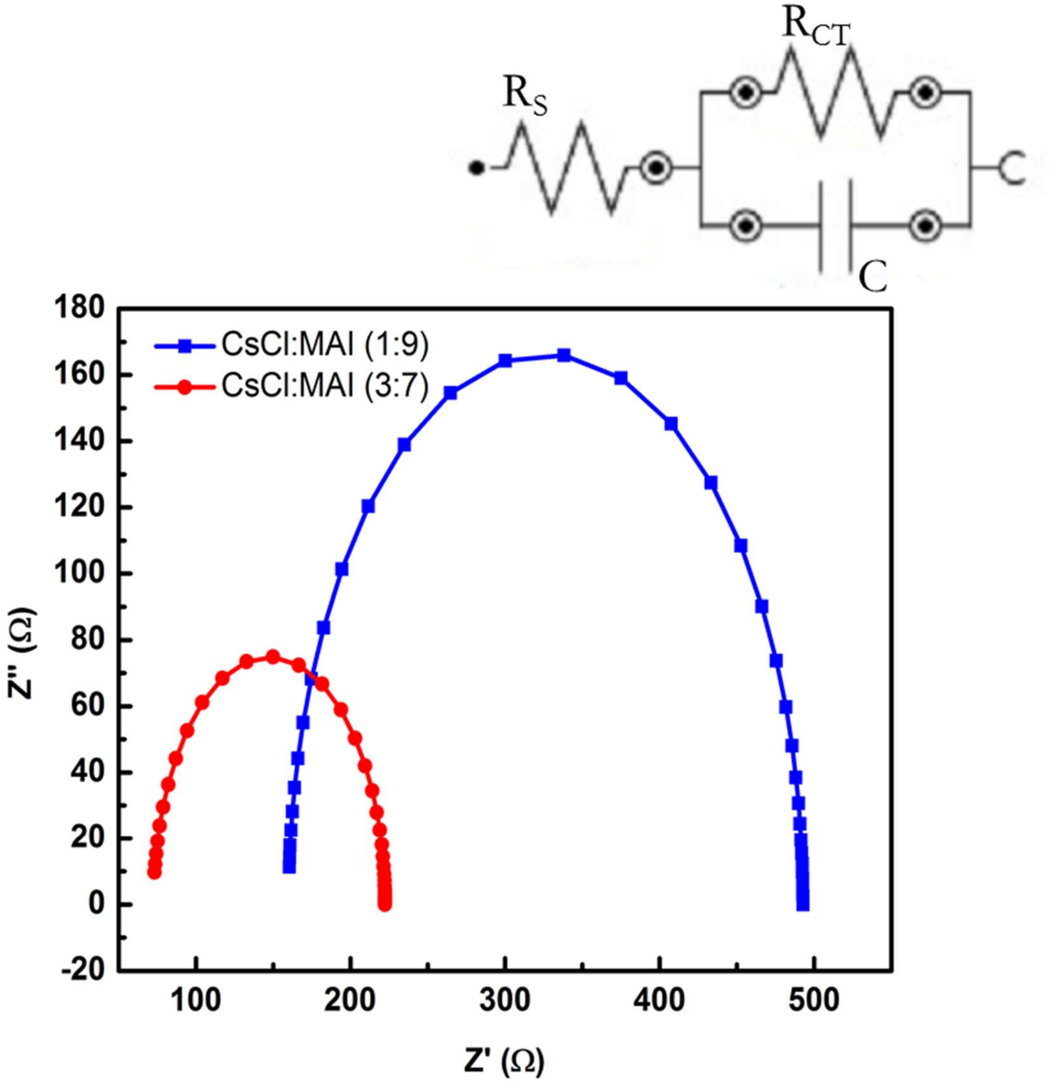

Figure 4.59: Nyquist plots of the CsCl:MAI lead-free Bismuth perovskite solar cells with equivalent circuit used for fitting (inset)

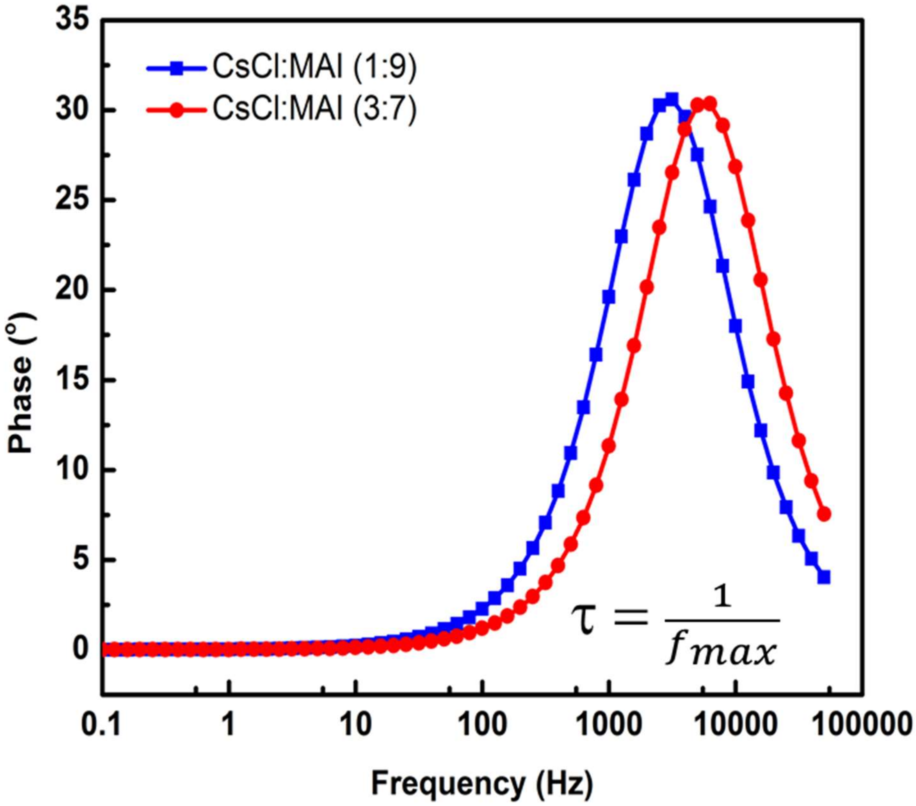

Figure 4.60: Bode Plots of CsCl:MAI lead-free Bismuth perovskite solar cells

Table 4.4: IV characteristics of mixed cation and mixed halides bismuth perovskite solar cells

Sample	**J_{SC} (mA cm^{-2})**	**V_{OC} (V)**	**FF (%)**	**η (%)**	**R_S (Ω)**	**R_{CT} (kΩ)**	**CPE (nF)**	**τ (s)**
CsCl:MAI (1:9)	1.119	0.466	40.32	0.21	160	333	282	0.317
CsCl:MAI (3:7)	1.101	0.488	43.15	0.23	72.7	150	327	0.2

Stability

The $CsMABiI_{9-x}Cl_x$ at (1:9 and 3:7) show no noticeable change in colour after two months and the photovoltaic performance recorded no significant losses.

CHAPTER 5

CONCLUSION

Renewable energy sources are the most viable and sustainable sources that can best meet the demand of the globe and the need for the sustainability of the environment. Development of renewable energy sources with facile fabrication technique and low cost production are both essential for their use. Solar photovoltaics are currently being used to harvest the enormous energy potential of the sun using silicon-based photovoltaic. Recently, third generation solution-processable solar cells have shown great potentials due to their unique properties like ease of fabrication, low cost, availability of materials and other remarkable features. Platinum counter electrodes were fabricated by a novel UV photoreduction fabrication process. Irradiation time, spin cpating cycles and solvent effects were investigated for the photofabricated platinum counter electrodes. X-ray photon spectroscopy (XPS), was used to characterized the photofabricated sample. scanning electron microscope (SEM) was used to study the morphology of the photofabricated Pt CEs. The catalytic performance of the electrodes was examined by cyclic voltammetry and electrochemical impedance spectroscopy techniques. And the electrodes were used in the fabrication of TiO2 dye sensitized solar cells (DSSCs) achieving a maximum efficiency of 8.12%. P-type DSSC based on CuO synthesized by pulsed laser ablation in liquid (PLAL) was fabricated and solvents effect on N719 was investigated. EIS of the fabricated samples were measured in other to understand charge transfer mechanism in the p-type CuO DSSCs. Mixed cation and mixed halides lead-free bismuth perovskite solar cells were fabricated and characterized. Morphology of the samples obtained from SEM revealed large hexagonal and bar like materials in 5 um range. This is particular good for perovskite solar cells material and challenges of charges recombination can the mitigated by the large crystals as the provide long diffusion length for photogenerated charges. The CsCl:MAI bismuth perovskite showed high broad absorbance peak within the visible light region amking a light harvester for photovoltaic device. Considerable high open circuit voltage VOC of 0.4907 V was achieved.

References

[1] O. Nematollahi, H. Hoghooghi, M. Rasti, and A. Sedaghat, “Energy demands and renewable energy resources in the Middle East,” *Renew. Sustain. Energy Rev.*, vol. 54, pp. 1172–1181, 2016.

[2] J. H. Heo, S. H. Im, J. H. Noh, T. N. Mandal, C. Lim, J. A. Chang, Y. H. Lee, H. Kim, A. Sarkar, K. Nazeeruddin, and M. Gra, “solar cells containing perovskite compound and,” vol. 7, no. June, 2013.

[3] M. A. Green, A. Ho-baillie, and H. J. Snaith, “The emergence of perovskite solar cells,” vol. 8, no. July, 2014.

[4] J. M. Ball, M. M. Lee, A. Hey, and H. J. Snaith, “Environmental Science,” pp. 1739–1743, 2013.

[5] M. Grätzel, “The light and shade of perovskite solar cells,” *Nat. Publ. Gr.*, vol. 13, no. 9, pp. 838–842, 2014.

[6] D. Liu and T. L. Kelly, “solution processing techniques,” *Nat. Photonics*, vol. 8, no. 2, pp. 133–138, 2013.

[7] N. Park, “Organometal Perovskite Light Absorbers Toward a 20 % E ffi ciency Low-Cost Solid-State Mesoscopic Solar Cell,” vol. 2, 2013.

[8] J. Im, C. Lee, J. Lee, S. Park, and N. Park, “Nanoscale,” vol. 2, pp. 4088–

4093, 2011.

[9] H. Zhou, “No Title,” vol. 542, 2014.

[10] S. Albrecht, M. Saliba, P. Correa, F. Lang, L. Korte, R. Schlatmann, M. K. Nazeeruddin, A. Hagfeldt, and M. Gra, “Monilithic perovskite/silicon-heterojunction tandem solar cells processed at low temperature,” *Energy Environ. Sci.*, vol. 9, pp. 81–88, 2015.

[11] J. Werner, C. H. Weng, A. Walter, L. Fesquet, J. P. Seif, S. De Wolf, B. Niesen, and C. Ballif, “Efficient Monolithic Perovskite/Silicon Tandem Solar Cell with Cell Area >1 cm2,” *J. Phys. Chem. Lett.*, vol. 7, no. 1, pp. 161–166, 2016.

[12] J. Sobuś and M. Ziółek, “Optimization of absorption bands of dye-sensitized and perovskite tandem solar cells based on loss-in-potential values.,” *Phys. Chem. Chem. Phys.*, vol. 16, pp. 14116–26, 2014.

[13] Y. M. Yang, Q. Chen, Y.-T. Hsieh, T.-B. Song, N. De Marco, H. Zhou, and Y. Yang, “Multilayer Transparent Top Electrode for Solution Processed Perovskite/Cu(In,Ga)(Se,S)2 Four Terminal Tandem Solar Cells.,” *ACS Nano*, vol. 9, no. 7, pp. 7714–21, 2015.

[14] W. Zi, X. Ren, X. Ren, Q. Wei, F. Gao, and S. F. Liu, “Perovskite/germanium tandem: A potential high efficiency thin film solar cell design,” *Opt. Commun.*, vol. 380, pp. 1–5, 2016.

[15] M. Anaya, J. P. Correa-Baena, G. Lozano, M. Saliba, P. Anguita, B. Roose, A. Abate, U. Steiner, M. Grätzel, M. E. Calvo, A. Hagfeldt, and H. Míguez, “Optical analysis of $CH_3NH_3Sn_xPb_{1-x}I_3$ absorbers: a roadmap for perovskite-on-perovskite tandem solar cells,” *J. Mater. Chem. A*, 2016.

[16] J. H. Heo and S. H. Im, “CH3NH3PbBr3-CH3NH3PbI3 Perovskite-Perovskite Tandem Solar Cells with Exceeding 2.2 V Open Circuit Voltage,” *Adv. Mater.*, pp. 5121–5125, 2015.

[17] M. Ledinsky, S. Nicolay, J. Bailat, J. Yum, and S. De Wolf, “Silicon Four-Terminal Tandem Solar Cells †,” pp. 1619–1629, 2015.

[18] Y. Jiang, I. Almansouri, S. Huang, T. Young, Y. Li, Y. Peng, Q. Hou, L. Spiccia, U. Bach, Y.-B. Cheng, M. Green, and A. Ho-Baillie, “Optical Analysis of Perovskite/Silicon Tandem Solar Cells,” *J. Mater. Chem. C*, vol. 4, pp. 5679–5689, 2016.

[19] P. Loper, B. Niesen, S.-J. Moon, S. Martin de Nicolas, J. Holovsky, Z. Remes, M. Ledinsky, F.-J. Haug, J.-H. Yum, S. De Wolf, C. Ballif, P. Loeper, B. Niesen, S.-J. Moon, S. M. de Nicolas, J. Holovsky, Z. Remes, M. Ledinsky, F.-J. Haug, J.-H. Yum, S. De Wolf, and C. Ballif, “Organic{â}{\texteuro}{\textquotedblleft}Inorganic Halide Perovskites: Perspectives for Silicon-Based Tandem Solar Cells,” *Ieee J. Photovoltaics*, vol. 4, no. 6, pp. 1545–1551, 2014.

[20] L. Chan, "INTERFACE STUDY OF SPIRO-OMETAD ON PASSIVATED P- , N- , AND N -Si (111) FOR USE IN TANDEM PEROVSKITE / SILICON SOLAR CELL DEVICES," no. 111, 2015.

[21] S. News, "Perovskite-silicon tandem solar cells with the highest power conversion efficiency," *ScienceDaily*, pp. 1–7, 2016.

[22] J. Liu, S. Lu, L. Zhu, X. Li, and W. C. H. Choy, "Perovskite-organic hybrid tandem solar cells using nanostructured perovskite layer as light window and PFN/doped-MoO3/MoO3 multi-layer interconnection layer," *Nanoscale*, pp. 3638–3646, 2016.

[23] D. P. McMeekin, G. Sadoughi, W. Rehman, G. E. Eperon, M. Saliba, M. T. Horantner, A. Haghighirad, N. Sakai, L. Korte, B. Rech, M. B. Johnston, L. M. Herz, and H. J. Snaith, "A mixed-cation lead mixed-halide perovskite absorber for tandem solar cells," *Science (80-.).*, vol. 351, no. 6269, pp. 151–155, 2016.

[24] F. Jiang, T. Liu, B. Luo, J. Tong, F. Qin, S. Xiong, Z. Li, and Y. Zhou, "Two-terminal perovskite/perovskite tandem solar cell," *J. Mater. Chem. A*, vol. 0, pp. 1–6, 2015.

[25] X. Jiang, K. M. Karlsson, E. Gabrielsson, M. J. Erik, M. Quintana, M. Karlsson, L. Sun, and A. Hagfeldt, "Supporting Information," pp. 1–4, 2011.

[26] A. Mei, "No Title," vol. 295, 2014.

[27] H. J. Snaith, A. Abate, J. M. Ball, G. E. Eperon, T. Leijtens, N. K. Noel, S. D. Stranks, J. T. Wang, K. Wojciechowski, and W. Zhang, “Anomalous Hysteresis in Perovskite Solar Cells,” no. iii, 2014.

[28] E. Environ, M. Guillermo, A. Garcia, P. Reinecke, T. Kroyer, M. I. Dar, K. Nazeeruddin, and H. J. Bolink, “Environmental Science,” pp. 994–997, 2014.

[29] J. You, Z. Hong, Y. M. Yang, Q. Chen, M. Cai, T. Song, and C. Chen, “Perovskite Solar Cells with High E ffi ciency and Flexibility,” no. Xx, 2014.

[30] S. S. Shin, W. S. Yang, J. H. Noh, J. H. Suk, N. J. Jeon, J. H. Park, J. S. Kim, W. M. Seong, and S. Il Seok, “High-performance flexible perovskite solar cells exploiting Zn2SnO4 prepared in solution below 100 °C,” *Nat. Commun.*, vol. 6, no. May, pp. 1–8, 2015.

[31] M. Ye, X. Hong, and X.-Y. Liu, “Recent Advancements in Perovskite Solar Cells: Flexibility, Stability and Large Scale,” *J. Mater. Chem. A*, vol. 4, pp. 6755–6771, 2016.

[32] S. Yun, A. Hagfeldt, and T. Ma, “Pt-free counter electrode for dye-sensitized solar cells with high efficiency,” *Adv. Mater.*, vol. 26, no. 36, pp. 6210–6237, 2014.

[33] J. H. Noh, J. H. Suk, N. J. Jeon, J. H. Park, J. S. Kim, W. M. Seong, and S.

Il Seok QDSSCs Review Elsevier pp. 994–997, 2014.

[34] J. Duan, H. Zhang, Q. Tang, B. He, and L. Yu, “Recent advances in critical materials for quantum dot-sensitized solar cells: a review,” *J. Mater. Chem. A*, vol. 3, no. 34, pp. 17497–17510, 2015.

[35] P. Docampo, J. M. Ball, M. Darwich, G. E. Eperon, and H. J. Snaith, “polymer substrates,” *Nat. Commun.*, vol. 4, pp. 1–6, 2013.

[36] F. Di Giacomo, V. Zardetto, A. D. Epifanio, S. Pescetelli, F. Matteocci, S. Razza, A. Di Carlo, S. Licoccia, W. M. M. Kessels, M. Creatore, and T. M. Brown, “Flexible Perovskite Photovoltaic Modules and Solar Cells Based on Atomic Layer Deposited Compact Layers and UV-Irradiated TiO 2 Scaffolds on Plastic Substrates,” pp. 1–9, 2015.

[37] B. Oregan and M. Gratzel, “a Low-Cost, High-Efficiency Solar-Cell Based on Dye-Sensitized Colloidal Tio2 Films,” *Nature*, vol. 353, no. 6346, pp. 737–740, 1991.

[38] S. Mathew, A. Yella, P. Gao, R. Humphry-Baker, B. F. E. Curchod, N. Ashari-Astani, I. Tavernelli, U. Rothlisberger, M. K. Nazeeruddin, and M. Grätzel, “Dye-sensitized solar cells with 13% efficiency achieved through the molecular engineering of porphyrin sensitizers,” *Nat. Chem.*, vol. 6, no. 3, pp. 242–247, 2014.

[39] K. M. Lee, C. Y. Hsu, W. H. Chiu, M. C. Tsui, Y. L. Tung, S. Y. Tsai, and

K. C. Ho, “Dye-sensitized solar cells with a micro-porous TiO2 electrode and gel polymer electrolytes prepared by in situ cross-link reaction,” *Sol. Energy Mater. Sol. Cells*, vol. 93, no. 11, pp. 2003–2007, 2009.

[40] U. Opara Krašovec, M. Berginc, M. Hočevar, and M. Topič, “Unique TiO2 paste for high efficiency dye-sensitized solar cells,” *Sol. Energy Mater. Sol. Cells*, vol. 93, no. 3, pp. 379–381, 2009.

[41] S. So, I. Hwang, and P. Schmuki, “Hierarchical DSSC structures based on ‘single walled’ TiO 2 nanotube arrays reach a back-side illumination solar light conversion efficiency of 8%,” *Energy Environ. Sci.*, vol. 8, no. 3, pp. 849–854, 2015.

[42] “Performance enhancement of dye sensitized solar cells based TiO 2 thick mesoporous photoanodes by morphological manipulation,” 2015.

[43] “TiO2 low index.” .

[44] M. a Alpuche-Aviles and Y. Wu, “Photoelectrochemical Study of the Band Structure of Zn2SnO4 Prepared by the Hydrothermal Method,” *J. Am. Chem. Soc.*, vol. 131, no. 9, pp. 3216–3224, 2009.

[45] B. S. Han, S. Caliskan, W. Sohn, M. Kim, J.-K. Lee, and H. W. Jang, “Room Temperature Deposition of Crystalline Nanoporous ZnO Nanostructures for Direct Use as Flexible DSSC Photoanode,” *Nanoscale Res. Lett.*, vol. 11, no. 1, p. 221, 2016.

[46] A. Thapa, J. Zai, H. Elbohy, P. Poudel, N. Adhikari, X. Qian, and Q. Qiao, "TiO2 coated urchin-like SnO2 microspheres for efficient dye-sensitized solar cells," *Nano Res.*, vol. 7, no. 8, pp. 1154–1163, 2014.

[47] C. Cavallo, F. Di Pascasio, A. Latini, M. Bonomo, and D. Dini, "Nanostructured Semiconductor Materials for Dye-Sensitized Solar Cells," vol. 2017, 2017.

[48] Y. Jo, C. L. Jung, J. Lim, B. H. Kim, C. H. Han, J. Kim, S. Kim, D. Kim, and Y. Jun, "A novel dye coating method for N719 dye-sensitized solar cells," *Electrochim. Acta*, vol. 66, no. April 2012, pp. 121–125, 2012.

[49] F. Bella, S. Galliano, C. Gerbaldi, and G. Viscardi, "Cobalt-based electrolytes for dye-sensitized solar cells: Recent advances towards stable devices," *Energies*, vol. 9, no. 5, pp. 1–22, 2016.

[50] J. Wu, Z. Lan, J. Lin, M. Huang, Y. Huang, L. Fan, and G. Luo, "Electrolytes in dye-sensitized solar cells," *Chem. Rev.*, vol. 115, no. 5, pp. 2136–2173, 2015.

[51] L.-L. Li, H.-H. Wu, C.-H. Tsai, and E. Wei-Guang Diau, "Nanofabrication of uniform and stabilizer-free self-assembled platinum monolayers as counter electrodes for dye-sensitized solar cells," *NPG Asia Mater.*, vol. 6, no. 8, p. e118, 2014.

[52] T. Y. Hsieh, T. C. Wei, P. Zhai, S. P. Feng, M. Ikegami, and T. Miyasaka,

"A room-temperature process for fabricating a nano-Pt counter electrode on a plastic substrate for efficient dye-sensitized cells," *J. Power Sources*, vol. 283, pp. 351–357, 2015.

[53] B. Anothumakkool, I. Agrawal, S. N. Bhange, R. Soni, O. Game, S. B. Ogale, and S. Kurungot, "Pt- and TCO-Free Flexible Cathode for DSSC from Highly Conducting and Flexible PEDOT Paper Prepared via in Situ Interfacial Polymerization," *ACS Appl. Mater. Interfaces*, vol. 8, no. 1, pp. 553–562, 2016.

[54] X. Zhao, M. Li, D. Song, P. Cui, Z. Zhang, Y. Zhao, C. Shen, and Z. Zhang, "A novel hierarchical Pt- and FTO-free counter electrode for dye-sensitized solar cell.," *Nanoscale Res. Lett.*, vol. 9, no. 1, p. 202, 2014.

[55] G. Yue, J. Wu, Y. Xiao, J. Lin, M. Huang, L. Fan, and Y. Yao, "A dye-sensitized solar cell based on PEDOT:PSS counter electrode," *Chinese Sci. Bull.*, vol. 58, no. 4, pp. 559–566, 2013.

[56] W. Wei, H. Wang, and Y. H. Hu, "A review on PEDOT-based counter electrodes for dye-sensitized solar cells," *Int. J. Energy Res.*, vol. 38, no. 9, pp. 1099–1111, 2014.

[57] A. Ali, K. Shehzad, F. Ur-Rahman, S. M. Shah, M. Khurram, M. Mumtaz, and R. U. R. Sagar, "Flexible, Low Cost, and Platinum-Free Counter Electrode for Efficient Dye-Sensitized Solar Cells," *ACS Appl. Mater.*

Interfaces, vol. 8, no. 38, pp. 25353–25360, 2016.

[58] I. Ali, K. Chul, A. Ayoub, M. Bilal, and S. Hoon, “Electrochimica Acta Graphene coated cotton fabric as textile structured counter electrode for DSSC,” *Electrochim. Acta*, vol. 173, pp. 164–171, 2015.

[59] H. Choi, H. Kim, S. Hwang, Y. Han, and M. Jeon, “Graphene counter electrodes for dye-sensitized solar cells prepared by electrophoretic deposition,” *J. Mater. Chem.*, vol. 21, pp. 7548–7551, 2011.

[60] L. Fu and a M. Yu, “Carbon Nanotubes Based Thin Films: Fabrication, Characterization and Applications,” *Rev. Adv. Mater. Sci*, vol. 36, pp. 40–61, 2014.

[61] S.-H. Hsu, C.-T. Li, H.-T. Chien, R. R. Salunkhe, N. Suzuki, Y. Yamauchi, K.-C. Ho, and K. C.-W. Wu, “Platinum-Free Counter Electrode Comprised of Metal-Organic-Framework (MOF)-Derived Cobalt Sulfide Nanoparticles for Efficient Dye-Sensitized Solar Cells (DSSCs),” *Sci. Rep.*, vol. 4, p. 6983, 2014.

[62] H. Y. Chen, J. Y. Liao, B. X. Lei, D. Bin Kuang, Y. Fang, and C. Y. Su, “Highly catalytic carbon nanotube/Pt nanohybrid-based transparent counter electrode for efficient dye-sensitized solar cells,” *Chem. - An Asian J.*, vol. 7, no. 8, pp. 1795–1802, 2012.

[63] G. Yue, X. Ma, W. Zhang, F. Li, J. Wu, and G. Li, “A highly efficient

flexible dye-sensitized solar cell based on nickel sulfide/platinum/titanium counter electrode.," *Nanoscale Res. Lett.*, vol. 10, p. 1, 2015.

[64] C. P. Lee, C. A. Lin, T. C. Wei, M. L. Tsai, Y. Meng, C. T. Li, K. C. Ho, C. I. Wu, S. P. Lau, and J. H. He, "Economical low-light photovoltaics by using the Pt-free dye-sensitized solar cell with graphene dot/PEDOT: PSS counter electrodes," *Nano Energy*, vol. 18, pp. 109–117, 2015.

[65] C. T. Li, C. P. Lee, Y. Y. Li, M. H. Yeh, and K. C. Ho, "A composite film of TiS2/PEDOT:PSS as the electrocatalyst for the counter electrode in dye-sensitized solar cells," *J. Mater. Chem. A*, vol. 1, no. 47, pp. 14888–14896, 2013.

[66] Z. Lan, J. Wu, J. Lin, and M. Huang, "Morphology controllable fabrication of Pt counter electrodes for highly efficient dye-sensitized solar cells," *J. Mater. Chem.*, vol. 22, no. 9, p. 3948, 2012.

[67] R. S. Moraes, E. Saito, D. M. G. Leite, M. Massi, and A. S. da Silva Sobrinho, "Optical, electrical and electrochemical evaluation of sputtered platinum counter electrodes for dye sensitized solar cells," *Appl. Surf. Sci.*, vol. 364, pp. 229–234, 2016.

[68] A. Iefanova, U. Gautam, P. Poudel, D. Davoux, V. Mallam, Q. Qiao, B. Logue, M. F. Baroughi, and S. Dakota, "Low Cost Platinum Counter Electrode for Dye-Sensitized Solar Cells," pp. 2716–2719, 2013.

[69] Y. Gong, C. H. Li, X. M. Huang, Y. H. Luo, D. M. Li, Q. B. Meng, and B. B. Iversen, “Simple Method for Manufacturing Pt Counter Electrodes on Conductive Plastic Substrates for Dye-Sensitized Solar Cells,” *ACS Appl. Mater. Interfaces*, vol. 5, pp. 795–800, 2013.

[70] D. Zhang, W. C. Chang, T. Okajima, and T. Ohsaka, “Electrodeposition of platinum nanoparticles in a room-temperature ionic liquid.,” *Langmuir*, vol. 27, no. 23, pp. 14662–8, 2011.

[71] L. Zhang, Z. Fang, G. C. Zhao, and X. W. Wei, “Electrodeposited platinum nanoparticles on the multi-walled carbon nanotubes and its electrocatalytic for nitric oxide,” *Int. J. Electrochem. Sci.*, vol. 3, no. 6, pp. 746–754, 2008.

[72] S. Domínguez-Domínguez, J. Arias-Pardilla, Á. Berenguer-Murcia, E. Morallón, and D. Cazorla-Amorós, “Electrochemical deposition of platinum nanoparticles on different carbon supports and conducting polymers,” *J. Appl. Electrochem.*, vol. 38, no. 2, pp. 259–268, 2008.

[73] X. Yin, Z. Xue, and B. Liu, “Electrophoretic deposition of Pt nanoparticles on plastic substrates as counter electrode for flexible dye-sensitized solar cells,” *J. Power Sources*, vol. 196, no. 4, pp. 2422–2426, 2011.

[74] L. Matoh, I. Kozjek Škofic, M. Čeh, and N. Bukovec, “A novel method for preparation of a platinum catalyst at low temperatures,” *J. Mater. Chem. A*, vol. 1, no. 4, p. 1065, 2013.

[75] X.-G. Mei, B.-H. Fan, K. Sun, and J.-Y. Ouyang, “High-performance dye-sensitized solar cells with nanomaterials as counter electrode,” *Proc. SPIE*, vol. 7411, no. Copyright (C) 2010 American Chemical Society (ACS). All Rights Reserved., p. 74110A/1-74110A/9, 2009.

[76] M. Saliba, “Environmental,” *Energy Environ. Sci.*, vol. 9, no. 6, pp. 1989–1997, 2016.

[77] S. Luo and W. A. Daoud, “Recent progress in organic – inorganic halide perovskite solar cells : mechanisms and material,” *J. Mater. Chem. A Mater. energy Sustain.*, vol. 3, pp. 8992–9010, 2015.

[78] T. Singh, A. Kulkarni, M. Ikegami, and T. Miyasaka, “Trilok Singh, * Ashish Kulkarni, Masashi Ikegami, and Tsutomu Miyasaka *,” pp. 6–11, 2016.

[79] W. Yin, T. Shi, Y. Yan, W. Yin, T. Shi, and Y. Yan, “Unusual defect physics in CH3NH3PbI3 perovskite solar cell absorber Unusual defect physics in CH 3 NH 3 PbI 3 perovskite solar cell absorber,” vol. 63903, no. 2014, pp. 2–6, 2015.

[80] J. Seo and S. Il Seok, “Fabrication of E ffi cient Formamidinium Tin Iodide Perovskite Solar Cells through SnF 2 − Pyrazine Complex,” pp. 2–5, 2016.

[81] Y. Hsiao, T. Wu, M. Li, Q. Liu, W. Qin, and B. Hu, “organo-metal halide perovskite solar cells,” *J. Mater. Chem. A Mater. energy Sustain.*, vol. 3, pp.

15372–15385, 2015.

[82] G. Niu, X. Guo, and L. Wang, “Review of recent progress in chemical stability of perovskite solar cells,” *J. Mater. Chem. A Mater. energy Sustain.*, vol. 3, pp. 8970–8980, 2015.

[83] Z. Xiao, Y. Yuan, Q. Wang, Y. Shao, Y. Bai, Y. Deng, Q. Dong, M. Hu, C. Bi, and J. Huang, “Thin-film semiconductor perspective of organometal trihalide perovskite materials for high-efficiency solar cells,” *Mater. Sci. Eng. R*, vol. 101, pp. 1–38, 2016.

[84] K. Wang, Z. Liang, X. Wang, and X. Cui, “Lead Replacement in CH 3 NH 3 PbI 3 Perovskites,” pp. 1–8, 2015.

[85] G. Giorgi and K. Yamashita, “ambipolar class of materials with enhanced photovoltaic performances,” *J. Mater. Chem. A Mater. energy Sustain.*, vol. 3, pp. 8981–8991, 2015.

[86] V. A. Online, T. Baikie, Y. Fang, J. M. Kadro, M. Schreyer, F. Wei, S. G. Mhaisalkar, M. Graetzel, and T. J. White, “Journal of Materials Chemistry A,” pp. 5628–5641, 2013.

[87] F. Hao, C. C. Stoumpos, D. H. Cao, R. P. H. Chang, and M. G. Kanatzidis, “Lead-free solid-state organic-inorganic halide perovskite solar cells,” *Nat. Photonics*, vol. 8, no. 6, pp. 489–494, 2014.

[88] V. A. Online, “RSC Advances,” pp. 18762–18766, 2013.

[89] M. Graetzel, O. Malinkiewicz, A. Yella, Y. H. Lee, G. Mı, M. K. Nazeeruddin, and H. J. Bolink, “Perovskite solar cells employing organic charge-transport layers,” vol. 8, no. February, 2014.

[90] H. Kim, C. Lee, J. Im, K. Lee, T. Moehl, A. Marchioro, S. Moon, R. Humphry-baker, J. Yum, J. E. Moser, and M. Gra, “All-Solid-State Submicron Thin Film,” pp. 1–7, 2012.

[91] D. Bi, W. Tress, M. I. Dar, P. Gao, J. Luo, C. Renevier, S. M. Zakeeruddin, M. K. Nazeeruddin, and M. Grätzel, “Efficient luminescent solar cells based on tailored mixed-cation perovskites,” vol. 2, pp. 1–23, 2016.

[92] Q. Chen, H. Zhou, Z. Hong, S. Luo, H. Duan, H. Wang, Y. Liu, G. Li, and Y. Yang, “Planar Heterojunction Perovskite Solar Cells via Vapor-Assisted Solution Process,” no. Scheme 1, pp. 3–6, 2013.

[93] Y. Luo, F. Meng, E. Zhao, Y. Zheng, Y. Zhou, and X. Tao, “Fine control of perovskite-layered morphology and composition via sequential deposition crystallization process towards improved perovskite solar cells,” *J. Power Sources*, vol. 311, pp. 130–136, 2016.

[94] T. Salim, S. Sun, Y. Abe, A. Krishna, A. C. Grimsdale, and Y. M. Lam, “and device architecture on device performance,” *J. Mater. Chem. A Mater. energy Sustain.*, vol. 3, pp. 8943–8969, 2015.

[95] J. M. Chem, T. Song, Q. Chen, H. Zhou, C. Jiang, H. Wang, M. Yang, and Y. Liu, "Perovskite solar cells: film formation and properties," *J. Mater. Chem. A Mater. energy Sustain.*, vol. 3, pp. 9032–9050, 2015.

[96] M. Habibi, F. Zabihi, M. R. Ahmadian-yazdi, and M. Eslamian, "Progress in emerging solution-processed thin film solar cells – Part II : Perovskite solar cells," *Renew. Sustain. Energy Rev.*, vol. 62, pp. 1012–1031, 2016.

[97] N. J. Jeon, J. H. Noh, Y. C. Kim, W. S. Yang, S. Ryu, and S. Il Seok, "inorganic – organic hybrid perovskite solar cells," vol. 13, no. September, pp. 897–903, 2014.

[98] X. Wang, Z. Li, W. Xu, S. A. Kulkarni, S. K. Batabyal, S. Zhang, A. Cao, and L. Helena, "TiO 2 nanotube arrays based flexible perovskite solar cells with transparent carbon nanotube electrode," *Nano Energy*, vol. 11, pp. 728–735, 2015.

[99] G. E. Eperon, V. M. Burlakov, P. Docampo, A. Goriely, and H. J. Snaith, "Morphological control for high performance, solution-processed planar heterojunction perovskite solar cells," *Adv. Funct. Mater.*, vol. 24, no. 1, pp. 151–157, 2014.

[100] J. Burschka, N. Pellet, S.-J. Moon, R. Humphry-Baker, P. Gao, M. K. Nazeeruddin, and M. Grätzel, "Sequential deposition as a route to high-performance perovskite-sensitized solar cells.," *Nature*, vol. 499, no. 7458,

pp. 316–320, 2013.

[101] M. Dianetti, F. Di Giacomo, G. Polino, C. Ciceroni, A. Liscio, A. D. Epifanio, S. Licoccia, T. M. Brown, A. Di Carlo, and F. Brunetti, “Solar Energy Materials & Solar Cells TCO-free flexible organo metal trihalide perovskite planar-heterojunction solar cells,” *Sol. Energy Mater. Sol. Cells*, vol. 140, pp. 150–157, 2015.

[102] H. C. Weerasinghe, Y. Dkhissi, A. D. Scully, R. A. Caruso, and Y. Cheng, “Encapsulation for improving the lifetime of flexible perovskite solar cells,” *Nano Energy*, vol. 18, pp. 118–125, 2015.

[103] X. Yin, P. Chen, M. Que, Y. Xing, W. Que, C. Niu, and J. Shao, “Highly Efficient Flexible Perovskite Solar Cells Using Solution-Derived NiO,” 2016.

[104] M. Xiao, F. Huang, W. Huang, Y. Dkhissi, Y. Zhu, J. Etheridge, A. Gray-weale, U. Bach, Y. Cheng, and L. Spiccia, “Angewandte A Fast Deposition-Crystallization Procedure for Highly Efficient Lead Iodide Perovskite Thin-Film Solar Cells **,” vol. 3168, pp. 10056–10061, 2014.

[105] Y. Zhang, X. Hu, L. Chen, Z. Huang, Q. Fu, Y. Liu, L. Zhang, and Y. Chen, “Flexible , hole transporting layer-free and stable CH 3 NH 3 PbI 3 / PC 61 BM planar heterojunction perovskite solar cells,” *Org. Electron.*, vol. 30, pp. 281–288, 2016.

[106] X. Xu, Q. Chen, Z. Hong, H. Zhou, Z. Liu, W. Chang, P. Sun, H. Chen, N. De Marco, M. Wang, and Y. Yang, “Working Mechanism for Flexible Perovskite Solar Cells with Simplified Architecture,” 2015.

[107] J. Xi, Z. Wu, K. Xi, H. Dong, B. Xia, T. Lei, F. Yuan, W. Wu, B. Jiao, and X. Hou, “Initiating crystal growth kinetics of α-HC(NH2)2PbI3 for flexible solar cells with long-term stability,” *Nano Energy*, vol. 26, pp. 438–445, 2016.

[108] S. Nanostructures, “Highly Efficient Flexible Perovskite Solar Cells with Antireflection and,” no. 10, pp. 10287–10295, 2015.

[109] F. Huang, Y. Dkhissi, W. Huang, M. Xiao, I. Benesperi, S. Rubanov, Y. Zhu, X. Lin, L. Jiang, Y. Zhou, A. Gray-weale, J. Etheridge, C. R. Mcneill, R. A. Caruso, U. Bach, L. Spiccia, and Y. Cheng, “Gas-assisted preparation of lead iodide perovskite films consisting of a monolayer of single crystalline grains for high efficiency planar solar cells,” *Nano Energy*, vol. 10, pp. 10–18, 2014.

[110] Y. Dkhissi, F. Huang, S. Rubanov, M. Xiao, and U. Bach, “Low temperature processing of flexible planar perovskite solar cells with efficiency over 10 %,” *J. Power Sources*, vol. 278, pp. 325–331, 2015.

[111] F. C. Krebs, J. Fyenbo, and M. Jørgensen, “Product integration of compact roll-to-roll processed polymer solar cell modules: methods and manufacture

using flexographic printing, slot-die coating and rotary screen printing," *J. Mater. Chem.*, vol. 20, no. 41, p. 8994, 2010.

[112] F. C. Krebs, "Polymer solar cell modules prepared using roll-to-roll methods: Knife-over-edge coating, slot-die coating and screen printing," *Sol. Energy Mater. Sol. Cells*, vol. 93, no. 4, pp. 465–475, 2009.

[113] T. M. Schmidt, T. T. Larsen-Olsen, J. E. Carlé, D. Angmo, and F. C. Krebs, "Upscaling of Perovskite Solar Cells: Fully Ambient Roll Processing of Flexible Perovskite Solar Cells with Printed Back Electrodes," *Adv. Energy Mater.*, vol. 5, no. 15, pp. 1–9, 2015.

[114] C. S. Ponseca, T. J. Savenije, M. Abdellah, K. Zheng, A. Yartsev, T. Pascher, T. Harlang, P. Chabera, T. Pullerits, A. Stepanov, J. Wolf, and V. Sundstro, "Organometal Halide Perovskite Solar Cell Materials Rationalized: Ultrafast Charge Generation, High and Microsecond-Long Balanced Mobilities, and Slow Recombination," 2014.

[115] Z. Lin, C. Jiang, C. Zhu, and J. Zhang, "Development of inverted organic solar cells with TiO_2 interface layer by using low-temperature atomic layer deposition.," *ACS Appl Mater Inter*, vol. 5, no. 3, pp. 713–8, 2013.

[116] M. Stefik, F. J. Heiligtag, M. Niederberger, and M. Grätzel, "Improved nonaqueous synthesis of TiO2 for dye-sensitized solar cells," *ACS Nano*, vol. 7, no. 10, pp. 8981–8989, 2013.

[117] J. Fan, Z. Li, W. Zhou, Y. Miao, Y. Zhang, and J. Hu, “Applied Surface Science Dye-sensitized solar cells based on TiO 2 nanoparticles / nanobelts double-layered film with improved photovoltaic performance,” vol. 319, pp. 75–82, 2014.

[118] A. Tricoli, A. S. Wallerand, and M. Righettoni, “Highly porous TiO2 films for dye sensitized solar cells,” *J. Mater. Chem.*, vol. 22, no. 28, p. 14254, 2012.

[119] A. Ranjitha, N. Muthukumarasamy, M. Thambidurai, D. Velauthapillai, A. M. Kumar, and Z. M. Gasem, “Superlattices and Microstructures Inverted organic solar cells based on Cd-doped TiO 2 as an electron extraction layer,” *Superlattices Microstruct.*, vol. 74, pp. 114–122, 2014.

[120] J. Troughton, D. Bryant, K. Wojciechowski, M. J. Carnie, H. Snaith, A. Worsley, and T. M. Watson, “solar cells employing metallic substrates †,” *J. Mater. Chem. A Mater. energy Sustain.*, vol. 3, pp. 9141–9145, 2015.

[121] L. Qiu, J. Deng, X. Lu, Z. Yang, and H. Peng, “Integrating Perovskite Solar Cells into a Flexible Fiber **,” pp. 10425–10428, 2014.

[122] D. Yang, R. Yang, J. Zhang, Z. Yang, S. F. Liu, and C. Li, “Environmental Science,” *Energy Environ. Sci.*, vol. 8, no. ii, pp. 3208–3214, 2015.

[123] J. Wang and Z. Lin, “Freestanding TiO\n 2 nanotube arrays with ultrahigh aspect ratio via electrochemical anodization,” *Chem. Mater.*, no.

20, pp. 1257–1261, 2008.

[124] J. M. Mac??k, H. Tsuchiya, and P. Schmuki, “High-aspect-ratio TiO2 nanotubes by anodization of titanium,” *Angew. Chemie - Int. Ed.*, vol. 44, no. 14, pp. 2100–2102, 2005.

[125] L. Qiu, S. He, J. Yang, J. Deng, and H. Peng, “Fiber-Shaped Perovskite Solar Cells with High Power Conversion Efficiency,” *Small*, pp. 2419–2424, 2016.

[126] S. Lee and H. Suk, “Environmental,” *Energy Environ. Sci.*, vol. 8, no. 3, pp. 916–921, 2015.

[127] H.-Y. Park, D. Lim, K.-D. Kim, and S.-Y. Jang, “Performance optimization of low-temperature-annealed solution-processable ZnO buffer layers for inverted polymer solar cells,” *J. Mater. Chem. A*, vol. 1, no. 21, p. 6327, 2013.

[128] H. H. Kim, C. Park, W. Choi, S. Cho, B. Moon, and D. I. Son, “Low-temperature-fabricated ZnO, AZO, and SnO2 nanoparticle-based dye-sensitized solar cells,” *J. Korean Phys. Soc.*, vol. 65, no. 9, pp. 1315–1319, 2014.

[129] M. H. Kumar, N. Yantara, S. Dharani, M. Graetzel, S. Mhaisalkar, P. Boix, and N. Mathews, “ChemComm ZnO-based perovskite solid state solar cells †,” pp. 2–4, 2013.

[130] K. Jung, J. Lee, J. Kim, W. Chae, and M. Lee, "Solution-processed flexible planar perovskite solar cells : A strategy to enhance efficiency by controlling the ZnO electron transfer layer , PbI 2 phase , and CH 3 NH 3 PbI 3 morphologies," vol. 324, pp. 142–149, 2016.

[131] M. A. Alpuche-aviles and Y. Wu, "Photoelectrochemical Study of the Band Structure of Zn 2 SnO 4 Prepared by the Hydrothermal Method," pp. 3216–3224, 2009.

[132] C. Nanoscale, "Nanoscale," pp. 557–562, 2012.

[133] Y. Zhao, L. Hu, H. Liu, M. Liao, X. Fang, and L. Wu, "Band Gap Tunable Zn 2 SnO 4 Nanocubes," pp. 1–7, 2014.

[134] L. S. Oh, D. H. Kim, J. A. Lee, S. S. Shin, J. Lee, I. J. Park, M. J. Ko, N. Park, S. G. Pyo, K. S. Hong, and J. Y. Kim, "Zn 2 SnO 4 - Based Photoelectrodes for Organolead Halide Perovskite Solar Cells," pp. 8–11, 2014.

[135] S. S. Shin, W. S. Yang, E. J. Yeom, S. J. Lee, and N. J. Jeon, "Tailoring of Electron-Collecting Oxide Nanoparticulate Layer for Flexible Perovskite Solar Cells," 2016.

[136] H. Yoon, S. M. Kang, J.-K. Lee, and M. Choi, "Hysteresis-free low-temperature-processed planar perovskite solar cells with 19.1% efficiency," *Energy Environ. Sci.*, 2016.

[137] S. Prakash, “Recent advances in flexible perovskite solar cells,” *Chem. Commun.*, vol. 51, no. 79, pp. 14696–14707, 2015.

[138] J. Wei, H. Li, Y. Zhao, W. Zhou, R. Fu, Y. Leprince-Wang, D. Yu, and Q. Zhao, “Suppressed hysteresis and improved stability in perovskite solar cells with conductive organic network,” *Nano Energy*, vol. 26, pp. 139–147, 2016.

[139] G. Iannaccone, M. V??lim??ki, E. Jansson, A. Sunnari, G. Corso, A. Bernardi, M. Levi, S. Turri, J. Hast, and G. Griffini, “Roll-to-roll compatible flexible polymer solar cells incorporating a water-based solution-processable silver back electrode with low annealing temperature,” *Sol. Energy Mater. Sol. Cells*, vol. 143, pp. 227–235, 2015.

[140] W. Qiu, M. Buffière, G. Brammertz, U. W. Paetzold, L. Froyen, P. Heremans, and D. Cheyns, “High efficiency perovskite solar cells using a PCBM / ZnO double electron transport layer and a short air-aging step,” vol. 26, pp. 30–35, 2015.

[141] T. Kim, J.-H. Kim, T. E. Kang, C. Lee, H. Kang, M. Shin, C. Wang, B. Ma, U. Jeong, T.-S. Kim, and B. J. Kim, “Flexible, highly efficient all-polymer solar cells,” *Nat. Commun.*, vol. 6, no. May, p. 8547, 2015.

[142] L. Sowjanya Pali, P. Ganesan, and A. Garg, “Inverted P3HT:PCBM organic solar cells on low carbon steel substrates,” *Sol. Energy*, vol. 133, pp. 339–

348, 2016.

[143] K. Liu, T. T. Larsen-Olsen, Y. Lin, M. Beliatis, E. Bundgaard, M. Jørgensen, F. C. Krebs, and X. Zhan, “Roll-coating fabrication of flexible organic solar cells: comparison of fullerene and fullerene-free systems,” *J. Mater. Chem. A*, vol. 4, no. 3, pp. 1044–1051, 2016.

[144] J. A. Hauch, P. Schilinsky, S. A. Choulis, R. Childers, M. Biele, and C. J. Brabec, “Flexible organic P3HT:PCBM bulk-heterojunction modules with more than 1 year outdoor lifetime,” *Sol. Energy Mater. Sol. Cells*, vol. 92, no. 7, pp. 727–731, 2008.

[145] C. Lungenschmied, G. Dennler, H. Neugebauer, S. N. Sariciftci, M. Glatthaar, T. Meyer, and A. Meyer, “Flexible, long-lived, large-area, organic solar cells,” *Sol. Energy Mater. Sol. Cells*, vol. 91, no. 5, pp. 379–384, 2007.

[146] M. Al-Ibrahim, H. K. Roth, U. Zhokhavets, G. Gobsch, and S. Sensfuss, “Flexible large area polymer solar cells based on poly(3-hexylthiophene)/ fullerene,” *Sol. Energy Mater. Sol. Cells*, vol. 85, no. 1, pp. 13–20, 2005.

[147] M. Kaltenbrunner, G. Adam, E. D. Głowacki, M. Drack, R. Schwödiauer, L. Leonat, D. H. Apaydin, H. Groiss, M. C. Scharber, M. S. White, N. S. Sariciftci, and S. Bauer, “improved stability in air,” vol. 14, no. August, 2015.

[148] L. Dqj, K. D. Xdq, D. X. D. Q. Hh, and K. H. Q. D. E. F. Xqj, “+ LJK YROWDJH DQG HIILFLHQW ELOD \ HU KHWHURMXQFWLRQ VRODU FHOOV EDVHG RQ DQ RUJDQLF ± LQRUJDQLF K \ EULG SHURYVNLWH DEVRUEHU ZLWK D ORZ FRVW IOH [LEOH VXEVWUDWH ,.”

[149] S. Ryu, J. Seo, S. S. Shin, Y. C. Kim, N. J. Jeon, J. H. Noh, and S. Il Seok, “Fabrication of metal-oxide-free CH3NH3PbI3 perovskite solar cells processed at low temperature,” *J. Mater. Chem. A Mater. energy Sustain.*, vol. 3, pp. 3271–3275, 2015.

[150] L. Yang, U. B. Cappel, E. L. Unger, M. Karlsson, K. M. Karlsson, E. Gabrielsson, L. Sun, G. Boschloo, A. Hagfeldt, and E. M. J. Johansson, “Comparing spiro-OMeTAD and P3HT hole conductors in efficient solid state dye-sensitized solar cells,” *Phys. Chem. Chem. Phys.*, vol. 14, no. 2, p. 779, 2012.

[151] W. H. Nguyen, C. D. Bailie, E. L. Unger, and M. D. Mcgehee, “Enhancing the Hole-Conductivity of Spiro-OMeTAD without Oxygen or Lithium Salts by Using Spiro(TFSI) 2 in Perovskite and Dye- Sensitized Solar Cells,” 2014.

[152] S. Wang, W. Yuan, and Y. S. Meng, “Spectrum-Dependent Spiro-OMeTAD Oxidization Mechanism in Perovskite Solar Cells,” *ACS Appl. Mater.*

Interfaces, vol. 7, no. 44, pp. 24791–24798, 2015.

[153] D. Shi, X. Qin, Y. Li, Y. He, C. Zhong, J. Pan, H. Dong, W. Xu, T. Li, W. Hu, J.-L. Bredas, and O. M. Bakr, "Spiro-OMeTAD single crystals: Remarkably enhanced charge-carrier transport via mesoscale ordering," *Sci. Adv.*, vol. 2, no. 4, pp. e1501491–e1501491, 2016.

[154] S. Ma, H. Zhang, N. Zhao, Y. Cheng, and M. Wang, "Spiro-thiophene derivatives as hole-transport materials for perovskite solar cells," *J. Mater. Chem. A Mater. energy Sustain.*, vol. 3, pp. 12139–12144, 2015.

[155] G. Hu, W. Guo, R. Yu, X. Yang, R. Zhou, C. Pan, and Z. Lin, "Nano Energy Enhanced performances of fl exible ZnO / perovskite solar cells by piezo-phototronic effect," vol. 23, pp. 27–33, 2016.

[156] J. Zhou, D. H. Anjum, L. Chen, X. Xu, I. A. Ventura, L. Jiang, and G. Lubineau, "The temperature-dependent microstructure of PEDOT/PSS films: insights from morphological, mechanical and electrical analyses," *J. Mater. Chem. C*, vol. 2, no. 46, pp. 9903–9910, 2014.

[157] U. Lang, N. Naujoks, and J. Dual, "Mechanical characterization of PEDOT:PSS thin films," *Synth. Met.*, vol. 159, no. 5–6, pp. 473–479, 2009.

[158] T. St??cker, A. K??hler, and R. Moos, "Why does the electrical conductivity in PEDOT:PSS decrease with PSS content? A study combining thermoelectric measurements with impedance spectroscopy," *J. Polym. Sci.*

Part B Polym. Phys., vol. 50, no. 14, pp. 976–983, 2012.

[159] S. Hsiung, K. Lin, K. Yuan, C. Tsai, S. Chen, and C. Wu, "ScienceDirect Improving the efficiency of CH 3 NH 3 PbI 3 based photovoltaics by tuning the work function of the PEDOT : PSS hole transport layer," vol. 122, pp. 892–899, 2015.

[160] Y. Li, L. Meng, Y. M. Yang, G. Xu, Z. Hong, Q. Chen, J. You, G. Li, Y. Yang, and Y. Li, "ultrathin flexible substrates," *Nat. Commun.*, pp. 1–10, 2016.

[161] S. H. Chang, K. F. Lin, K. Y. Chiu, C. L. Tsai, H. M. Cheng, S. C. Yeh, W. T. Wu, W. N. Chen, C. T. Chen, S. H. Chen, and C. G. Wu, "Improving the efficiency of CH3NH3PbI3 based photovoltaics by tuning the work function of the PEDOT: PSS hole transport layer," *Sol. Energy*, vol. 122, pp. 892–899, 2015.

[162] J. W. Jo, M. Seo, M. Park, J. Kim, J. S. Park, I. K. Han, H. Ahn, J. W. Jung, B. Sohn, M. J. Ko, and H. J. Son, "Improving Performance and Stability of Flexible Planar- Heterojunction Perovskite Solar Cells Using Polymeric Hole-Transport Material," pp. 1–8, 2016.

[163] M. Li, P. Shen, K. Wang, T. Guo, and P. Chen, "based solar cells," *J. Mater. Chem. A Mater. energy Sustain.*, vol. 3, pp. 9011–9019, 2015.

[164] S. Nanhai and et al., "Efficient flexible organic solar cells with room

temperature sputtered and highly conductive NiO as hole-transporting layer," *J. Phys. D. Appl. Phys.*, vol. 43, no. 44, p. 445101, 2010.

[165] H. Zhang, J. Cheng, F. Lin, H. He, J. Mao, K. S. Wong, A. K.-Y. Jen, and W. C. H. Choy, "Pinhole-Free and Surface-Nanostructured NiOx Film by Room-Temperature Solution Process for High-Performance Flexible Perovskite Solar Cells with Good Stability and Reproducibility," *ACS Nano*, p. acsnano.5b07043, 2015.

[166] C. Chappaz-Gillot, S. Berson, R. Salazar, B. Lechêne, D. Aldakov, V. Delaye, S. Guillerez, and V. Ivanova, "Polymer solar cells with electrodeposited CuSCN nanowires as new efficient hole transporting layer," *Sol. Energy Mater. Sol. Cells*, vol. 120, no. PART A, pp. 163–167, 2014.

[167] P. Qin, S. Tanaka, S. Ito, N. Tetreault, K. Manabe, H. Nishino, M. K. Nazeeruddin, M. G. A. Tzel, and M. Grätzel, "Inorganic hole conductor-based lead halide perovskite solar cells with 12.4% conversion efficiency," *Nat Commun*, vol. 5, no. May, pp. 1–6, 2014.

[168] S. Ye, W. Sun, Y. Li, W. Yan, H. Peng, Z. Bian, Z. Liu, and C. Huang, "CuSCN-based inverted planar perovskite solar cell with an average PCE of 15.6%," *Nano Lett.*, p. 150504172654007, 2015.

[169] K. Zhao, R. Munir, B. Yan, Y. Yang, T.-S. Kim, and A. Amassian,

“Solution-processed inorganic copper(I) thiocyanate (CuSCN) hole transporting layers for efficient p–i–n perovskite solar cells,” *J. Mater. Chem. A*, vol. 3, pp. 20554–20559, 2015.

[170] J. A. Christians, R. C. M. Fung, P. V Kamat, N. Dame, and C. Student, “Supporting Information An Inorganic Hole Conductor for Organo-Lead Halide Perovskite Solar Cells . Improved Hole Conductivity with Copper Iodide .,” pp. 3–6, 2013.

[171] G. A. Sepalage, S. Meyer, A. Pascoe, A. D. Scully, F. Huang, U. Bach, Y.-B. Cheng, and L. Spiccia, “Copper(I) Iodide as Hole-Conductor in Planar Perovskite Solar Cells: Probing the Origin of J-V Hysteresis,” *Adv. Funct. Mater.*, no. I, p. n/a-n/a, 2015.

[172] W.-Y. Chen, L.-L. Deng, S.-M. Dai, X. Wang, C.-B. Tian, X.-X. Zhan, S.-Y. Xie, R.-B. Huang, and L. Zheng, “Low-cost solution-processed copper iodide as an alternative to PEDOT: PSS hole transport layer for efficient and stable inverted planar heterojunction perovskite solar cells,” *J. Mater. Chem. A*, vol. 3, no. 38, pp. 19353–19359, 2015.

[173] H. Rao, S. Ye, W. Sun, W. Yan, Y. Li, H. Peng, Z. Liu, Z. Bian, Y. Li, and C. Huang, “A 19.0% efficiency achieved in CuOx-based inverted CH3NH3PbI3-xClx solar cells by an effective Cl doping method,” *Nano Energy*, pp. 0–23, 2016.

[174] J. Bouclé and N. Herlin-boime, "The bene fi ts of graphene for hybrid perovskite solar cells," *Synth. Met.*, no. 2015, 2016.

[175] J. M. Chem, M. Batmunkh, C. J. Shearer, J. Biggs, and J. G. Shapter, "Nanocarbons for mesoscopic perovskite solar cells," *J. Mater. Chem. A Mater. energy Sustain.*, vol. 3, pp. 9020–9031, 2015.

[176] T. Liu, D. Kim, H. Han, A. R. Bin Mohd Yusoff, and J. Jang, "Fine-tuning Optical and Electronic Properties of Graphene Oxide for Highly Efficient Perovskite Solar Cells," *Nanoscale*, vol. 7, pp. 10708–10718, 2015.

[177] K.-T. Lee, L. Guo, and H. Park, "Neutral- and Multi-Colored Semitransparent Perovskite Solar Cells," *Molecules*, vol. 21, no. 4, p. 475, 2016.

[178] Y. Luo, X. Chen, C. Zhang, J. Li, J. Shi, Z. Sun, Z. Wang, and S. Huang, "AgAl alloy electrode for efficient perovskite solar cells," *RSC Adv.*, vol. 5, no. 69, pp. 56037–56044, 2015.

[179] Y. Wang, S. Bai, L. Cheng, N. Wang, J. Wang, F. Gao, and W. Huang, "High-Efficiency Flexible Solar Cells Based on Organometal Halide Perovskites," *Adv. Mater.*, pp. 4532–4540, 2015.

[180] M. Makha, S. L. Fernandes, S. Jenatsch, T. Offermans, J. Schleuniger, J.-N. Tisserant, A. C. Véron, and R. Hany, "A transparent, solvent-free laminated top electrode for perovskite solar cells," *Sci. Technol. Adv. Mater.*, vol. 0,

no. ja, pp. 1–19, 2016.

[181] P. Solar, Z. Li, S. A. Kulkarni, P. P. Boix, E. Shi, A. Cao, K. Fu, and S. K. Batabyal, “Laminated Carbon Nanotube Networks for Metal Electrode-Free,” no. 7, pp. 6797–6804, 2014.

[182] H. Wei, J. Xiao, Y. Yang, S. Lv, J. Shi, X. Xu, J. Dong, Y. Luo, D. Li, and Q. Meng, “Free-standing flexible carbon electrode for highly efficient hole-conductor-free perovskite solar cells,” *Carbon N. Y.*, vol. 93, pp. 861–868, 2015.

[183] K. Yan, Z. Wei, J. Li, H. Chen, Y. Yi, X. Zheng, X. Long, Z. Wang, J. Wang, J. Xu, and S. Yang, “High-performance graphene-based hole conductor-free perovskite solar cells: Schottky junction enhanced hole extraction and electron blocking,” *Small*, vol. 11, no. 19, pp. 2269–2274, 2015.

Vitae

Idris Kayode Popoola

Personal Details

Place of Birth: Nigeria

Nationality: Nigerian

Marital Status: Married

Address: 12 Kolapo Raheem Crescent, Agbede Transformer, Ikorodu, Lagos State, Nigeria

Email: pen4group@gmail.com

Objective

To strive for excellence and precision at all time, in all positions and circumstances, attaining professional distinction and proficiency.

Education

- 2015 – 2017
  Masters of Science (MS)
  Physics
  King Fahd University of Petroleum and Minerals (KFUPM), Dhahran, Saudi Arabia.

- 2006 – 2011
  B.Tech. (***First class***)
  Physics Electronics
  Federal University of Technology, PMB 65, Minna, Nigeria.

Research Interest

- Synthesis and characterization of nanomaterials.
- Fabrication and characterization of solar cells [Dye Sensitized Solar cells (DSSCs, Quantum-dot Sensitized Solar Cells (QDSSCs) and Perovskite Solar Cells (PSCs)]
- Thin film technology.

Research Experience

- January 2015 till date
  Graduate Student,
  Physics department
  King Fahd University of Petroleum and Minerals, Dhahran, Saudi Arabia.
  Fabrication of solar cell devices (DSSCs, QDSSCs and PSCs).

- January 2015 till date
  Graduate Student,
  Center for Excellence in Nanotechnology (CENT) Research Institute
  King Fahd University of Petroleum and Minerals, Dhahran, Saudi Arabia.
  Nanocomposite materials [Synthesis using pulsed laser ablation in liquid (PLAL) and characterization]).

Fabrication, Synthesis, and Characterization Techniques Expertise

- Spin-coating
- Drop casting
- Blade coating
- Pulsed laser ablation in liquid (PLAL)
- Sol-gel synthesis
- Hydrothermal synthesis
- Working in glovebox
- UV-Vis spectrophotometry [measurement and analysis]
- I-V characterization [Measurement and analysis on Autolab potentiostat and NOVA software]
- FTIR/ATR Characterization [Measurement and analysis].
- X-ray Diffraction (XRD) [Measurement and Analysis]
- X-ray Photoelectron Spectroscopy (XPS) [Analysis]
- Electrochemical Impedance Spectroscopy (EIS) [Measurement and analysis of Nyquist plot, Bode plot and Tafel Polarization on Autolab potentiostat equipped with NOVA software]
- Cyclic voltammogram (CV) [Measurement and analysis on Autolab potentiostat and NOVA software]

Skills

- Proficiency in computer usage
- Good and efficient research abilities
- Effective Leadership and Administrative skills
- Excellent oral and written communication skills

Work Experience

- September 2013 till date
  Department of Physics/Geology/Geophysics,
  Federal University, Ndufu-Alike, Ikwo , Nigeria.
  Graduate Assistant

- July 2012 – May 2013
  University of Ilorin, P.M.B. 1515 Ilorin, Nigeria.
  Teaching and Research Assistant (National service)

- June 2010 – December 2010
  OCI Automations (Nigeria Representative of National Instrument) 58, Kudirat Abiola way Oregun-Ikeja, Lagos
  Intern

Scientific Publications

i. Idris K. Popoola, Mohammad A. Gondal[*], Jwaher Al-Ghamdi, and Talal F. Qahtan, ***Mixed Cations and Mixed Halides Lead-free Bismuth based Perovskite Solar Cells,*** **2017 (Ready for Submission).**

ii. Idris K. Popoola, Mohammad. A. Gondal[*], Jwaher. Al-Ghamdi, and Talal F. Qahtan, ***Photofabrication of Highly Transparent Platinum Counter Electrodes at Ambient Temperature for Bifacial Dye Sensitized Solar Cells,*** NanoEnergy, Elsevier Ltd, **2017 (Submitted).**

iii. Idris K. Popoola, Mohammad A. Gondal[*], Jwaher Al-Ghamdi, and Talal F. Qahtan, ***Photovoltaic Performance of P-type Dye Sensitized Solar Cells utilizing Facile Pulsed Laser Ablation Synthesized CuO Nanospheres*****, 2017 (Ready for submission).**

iv. Idris K. Popoola, Mohammad A. Gondal[*], Jwaher Al-Ghamdi and Talal F. Qahtan, ***Facile In situ Photofabrication of Platinum/reduced Graphene oxide composites Counter Electrodes at ambient temperature for Bifacial Dye Sensitized Solar Cells*****, 2017 (Ready for Submission)**

v. Idris K. Popoola, Mohammed A. Gondal and Talal F. Qahtan,
Recent progress in flexible perovskite solar cells: materials, mechanical tolerance and stability**,** Renewable and Sustainable Energy Reviews, Elsevier Ltd, ***2017 (Resubmitted with minor revision).***

vi. Ibrahim O. Alade, Tajudeen A. Oyehan, **Idris K. Popoola**, Sunday O. Olatunji, Bagudu Aliyu, ***Modeling thermal conductivity enhancement of metal and metallic***

oxide nanofluids using support vector regression**.** Applied Powder Technology (APT), Elsevier Ltd. – ***2016 (Resubmitted with minor revision).***

vii. Taoreed.O. Owolabi, Mohamed Faiz, Sunday O. Olatunji, **Idris.K.Popoola**, ***Computational intelligence method of determining the energy band gap of doped ZnO semiconductor***, **(Published)** http://dx.doi.org/10.1016/j.matdes.2016.03.116 0264-1275/© 2016 Elsevier Ltd.

Seminar and Poster presentation

I. K. Popoola, M. A. Gondal, ***Novel Fabrication Techniques of Third Generation Solar Cells,*** Physics Day, KFUPM, **2017 (Poster presentation)**

Idris K. Popoola, ***Nanomaterials Applications in Energy Harvesting***, Physics Department KFUPM **2016** (**Seminar**)

Idris K. Popoola, ***Nanomaterials Applications in Solar Cells***, Center for Excellence in Nanotechnology (CENT) KFUPM **2016 (Seminar)**

Membership of Professional Bodies and Associations

Member, *Nigerian Institute of Physics (NIP)*

Student Member (90837538), *Institute of Electrical and Electronics Engineering (IEEE)*

Conference, Seminar and Workshop Attended

25th – 27th October, 2016 – The 4th Saudi International Nanotechnology Conference (SINC 2016)

21st April 2015- 4th KFUPM-KAUST Workshop on Solid-State Lighting

26th – 30th May, 2014 - "The Role of Physics in the Nano World" Nigeria Institute of Physics (NIP) 36th Annual Conference, Uyo.

2013, Examination Ethics Workshop, Federal University, Ndufu-Alike, Ikwo

2011, Entrepreneurship Training Workshop, Physics Department, Federal University of Technology, Minna

2010, Nigercon – Abuja, Nigeria Institute of Electrical and Electronics Engineers (NIEEE)

2010, Institutional Productivity and Quality Assurance Workshop, Federal University of Technology, Minna

2007, “Energy in National Development” Nigeria Institute of Physics (NIP) Conference, Lagos

Social Works.

2016 Voluntary work, King Fahd University of Petroleum and Minerals, Dhahran, Saudi Arabia

July 2012 – June 2013, MDGs Family and Community Life Reorientation (FACOR) – National Youth Service Corps (NYSC).

2007 – 2012, Undergraduates, Volunteer Tutor of various undergraduates’ courses, FUT, Minna